Research of Processing Methods for Overlapped Neural Spikes using Bayesian Statistics
(ベイズ推論を用いたオーバーラップを含む神経信号の処理手法に関する研究)

Tatsuya Haga

芳賀　達也

Abstract

Overlapping of spike waveforms is a major problem in the detection and sorting of extracellularly recorded neural spikes because the original spike waveforms can become hidden and merged due to overlapping. Previous methods proposed for solving this problem include using a multitrode or placing a restriction on spike patterns. In the thesis, we proposed two methods to detect and sort arbitrarily overlapped spikes in order to help to obtain more accurate analyses of highly synchronized neural activity.

First, we propose a fast sequential method that can robustly detect and sort arbitrarily overlapped spikes recorded with arbitrary types of electrodes. In our method, the probabilities of possible spike trains including ones with overlapping are evaluated by a sequential Bayesian inference based on probabilistic models of spike-train generation and extracellular voltage recording. We derived a computationally efficient sequential Bayesian inference algorithm based on these models that is used to calculate the probability of spike existence at each sampling time in real-time. In addition, the “look-ahead probability", the probability calculated with the data for a few sampling times ahead, results in more efficient calculation. We assessed the performance of our method with simulated neural signals and a real neural signal recorded from primary cortical neurons cultured on a multi-electrode array. Our results showed that our method could be applied in real-time and the delay was less than 10ms. Furthermore, the estimation accuracy was higher than that of a conventional spike sorting method, especially for signals with many overlapped spikes.

Second, a method for simultaneous estimation of spike templates and timings of highly-overlapped spikes was proposed and the performance was assessed using simulated and real neural signals. In our method, the inference based on the hidden Markov model with the probabilistic penalty is efficiently calculated with the approximation. As the result, it was showed that our method could appropriately decompose the simulated and real signals containing complexly overlapped spikes.

Last, we applied two methods in combination to various data and compared the traditional approach and the application without the combination. The strong and weak points of these two methods are complementary and the procedure using two methods in combination performed better than other methods and applying without combination.

Contents

Chapter 1 Introduction

1.1 Neurons and action potentials

1.1.1 Morphology of neurons

1.1.2 Concentrations of ions and equilibrium potentials

1.1.3 Action potentials

1.1.4 Cable Theory

1.1.5 Variety of electrophysiological properties

1.2 Recording of action potentials

1.2.1 Intracellular voltage recording

1.2.2 Extracellular voltage recording

1.2.3 Optical recording

1.3 Mechanisms of extracellular voltage recording

1.3.1 Polarization of electric charges in the extracellular medium

1.3.2 The extracellular potential produced by a single current source

1.3.3 The relationship between the intracellular potential and the extracellular potential

1.3.4 The extracellular potential produced by distributed membrane currents

1.4 Signal processing for neural spikes

1.4.1 Extraction of neural activity from extracellular voltage signals

1.4.2 Spike detection and sorting

1.4.3 Issues in spike detection and sorting

1.4.4 Previous studies dealing with spike overlaps

1.5 Scope and contributions

1.6 Organization

Chapter 2 Real-time Detection and Sorting of Overlapped Neural Spikes

2.1 Overview

2.2 Methods

2.2.1 Models of spike-train generation and multi-unit recording

2.2.2 Sequential Bayesian inference

2.2.3 Algorithms

2.3 Experiments

2.3.1 Assessment of computational efficiency and error rates with simulated signals

2.3.2 Assessments with the real neural signal
2.4 Results
2.4.1 Computational efficiency and error rates for simulated signals
2.4.2 Assessments with the real neural signal
2.5 Discussion
2.6 Summary of the chapter

Chapter 3 Simultaneous Inference of Templates and Timings of Highly Overlapped Neural Spikes
3.1 Overview
3.2 Methods
3.2.1 The model of extracellular voltage recordings
3.2.2 The model of spike trains
3.2.3 Estimation of hidden variables and parameters
3.3 Experiments
3.3.1 Assessments with simulated signals
3.3.2 Assessments with the real neural signal
3.4 Results
3.4.1 Assessments with simulated signals
3.4.2 Assessments with the real neural signal
3.5 Discussion
3.6 Summary of the chapter

Chapter 4 Combination of two methods
4.1 Overview
4.2 Experiments
4.3 Results
4.4 Discussion
4.5 Summary of the chapter

Chapter 5 Conclusion
5.1 Summary of the thesis
5.2 Future research directions
5.2.1 Real-time creation of spike templates and acceleration of computation
5.2.2 Handling short-term changes of spike templates caused by bursting
5.2.3 Handling artifact noises

5.2.4 Application to connectivity analysis

Acknowledgements

References

Publications

Appendix A Cell culture and recording methods

Appendix B Derivation of equations to update parameters in M-step

Chapter 1
Introduction

1.1 Neurons and action potentials

1.1.1 Morphology of neurons

Neurons are electrically excitable cells that process and transmit information in the brain. The typical morphology of neurons is shown in Figure 1.1. A neuron has a soma and two types of protrusions, dendrites and axons, which have different shapes according to the types of neurons they belong to and their locations in the brain. An axon of a neuron is connected to the dendrites of other neurons through synapses, and neuronal excitation is transmitted through these synapses. Electrical excitation propagated through neuronal networks is the basis of information processing in the brain.

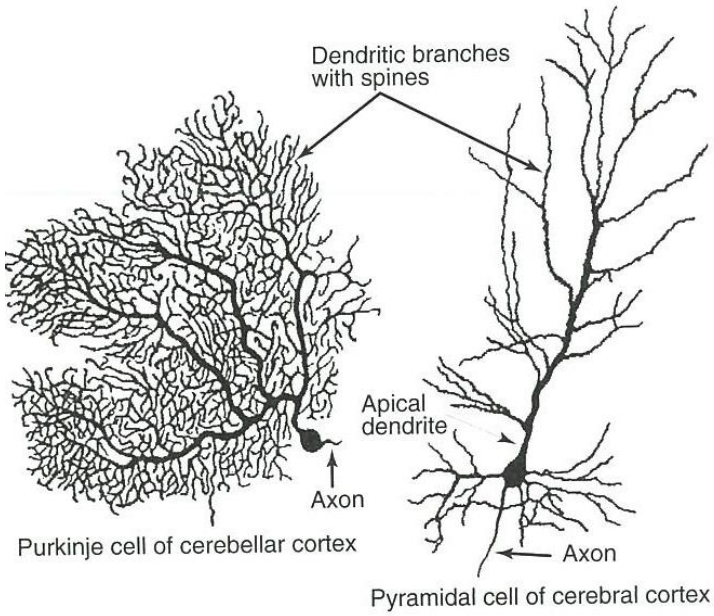

Figure 1.1. Typical morphology of neurons. (Left) A Purkinje cell of the cerebellar cortex and (right) a pyramidal neuron of the neocortex. Each has an extensively branched, spiny apical dendrite, shorter basal dendrites, and a single axon emerging from the basal pole of the cell. This figure was reprinted, with permission, from Fundamental Neuroscience, Third Edition, Squire LR, Bloom FE, Spitzer NC, Darwin B, Lac S, Ghosh A, ⓒAcademic Press (2008).

1.1.2 Concentrations of ions and equilibrium potentials

On the membranes of neurons, ion pumps that transport ions through the membranes in one direction produce differences between the intracellular and extracellular concentrations of potassium and sodium ions. The differences in the concentrations of ions result in differences in the potentials between the extracellular and intracellular space (the membrane potential). In this situation, ions move in the direction that cancels out the difference in the potential when ions can pass through the membranes. However, ions also move from a region with high concentration to a region with low concentration. Membrane potentials are strongly influenced by these movements of ions. In contrast, the ion concentrations are almost unchanged. Consequently, in some membrane potential, the two ion fluxes balance out, and there is no apparent current. This membrane potential is called the equilibrium potential. The equilibrium potential of each kind of ion is determined by the Nernst equation (Kandel et al., 2000):

$$E_{\mathrm{ion}} = \frac{RT}{zF} \log \frac{[\mathrm{ion}]_{\mathrm{o}}}{[\mathrm{ion}]_{\mathrm{i}}} \tag{1.1}$$

where E_{ion} is the membrane potential at which the ionic species is at equilibrium, R is the gas constant (8.315 $\mathrm{J\,K^{-1}\,mol^{-1}}$), T is the temperature in Kelvin, F is Faraday's constant (96485 $\mathrm{C\,mol^{-1}}$), z is the valence of the ion, and $[\mathrm{ion}]_{\mathrm{o}}$ and $[\mathrm{ion}]_{\mathrm{i}}$ are the concentrations of the ion outside and inside the cell, respectively. At room temperature (25°C), the equilibrium potential for $\mathrm{K^+}$ is

$$E_{\mathrm{K}} = 58\mathrm{mV} \log \frac{20}{400} = -75\mathrm{mV} \tag{1.2}$$

and the equilibrium potential for $\mathrm{Na^+}$ is

$$E_{\mathrm{Na}} = 58\mathrm{mV} \log \frac{440}{50} = +55\mathrm{mV}. \tag{1.3}$$

In the steady state, the multiple ion fluxes that pass through the membrane balance out, and the membrane potential is stabilized at the resting membrane potential determined by the Goldman equation (Kandel et al., 2000):

$$V_{\mathrm{ion}} = \frac{RT}{F} \log \frac{P_{\mathrm{K}}[\mathrm{K^+}]_{\mathrm{o}} + P_{\mathrm{Na}}[\mathrm{Na^+}]_{\mathrm{o}} + P_{\mathrm{Cl}}[\mathrm{Cl^-}]_{\mathrm{i}}}{P_{\mathrm{K}}[\mathrm{K^+}]_{\mathrm{i}} + P_{\mathrm{Na}}[\mathrm{Na^+}]_{\mathrm{i}} + P_{\mathrm{Cl}}[\mathrm{Cl^-}]_{\mathrm{o}}} \tag{1.4}$$

where P_{K}, P_{Na}, and P_{Cl} are the permeability of potassium ions, sodium ions, and chloride ions, respectively.

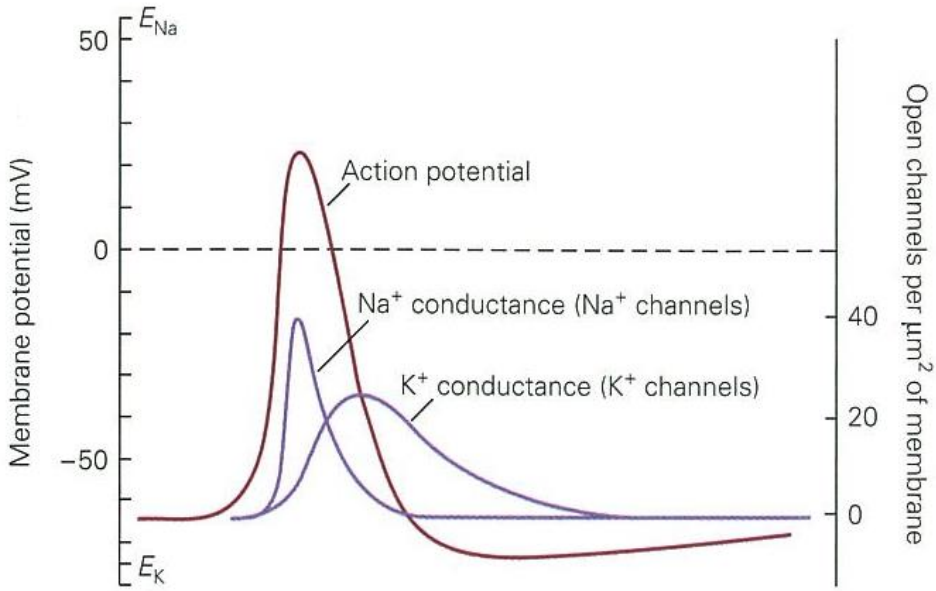

Figure 1.2. The sequential opening of voltage-gated Na^+ and K^+ channels generates the action potential. The shape of the action potential and the underlying conductance changes can be calculated from the properties of the voltage-gated Na^+ and K^+ channels. This figure was reprinted, with permission, from Principles of Neural Science, 4th edition, Kandel E, Schwartz J, Jessel T, ⓒ McGraw-Hill Medical (2000).

1.1.3 Action potentials

The electrical excitation of neurons result in a sharp change of the membrane potential, and this is called an action potential. The membrane potential is normally stabilized around -65mV (the resting membrane potential). When a neuron is excited, the membrane potential steeply rises to approximately 30 mV and then decreases to the resting membrane potential (Figure 1.2). After generation, action potentials travel through an axon and excite synapses to make other neurons generate neural spikes.

Action potentials are generated by the opening and closing of ion channels on the membrane. On a neuron's membrane, there are many ion channels through which only sodium ions or potassium ions can pass (Figure 1.3). These ion channels are normally closed, but they open when the membrane potential rises and the conductance of the membrane for the corresponding type of ion increases. After that, the ion channels are closed and inactivated for a short time (approximately 2 ms) after the opening of the ion channels, and this prevents the neuron from generating an action potential again (Figure 1.4). This is called the refractory period, and it is an important feature of a neuron that prevents the backward transmission of excitation.

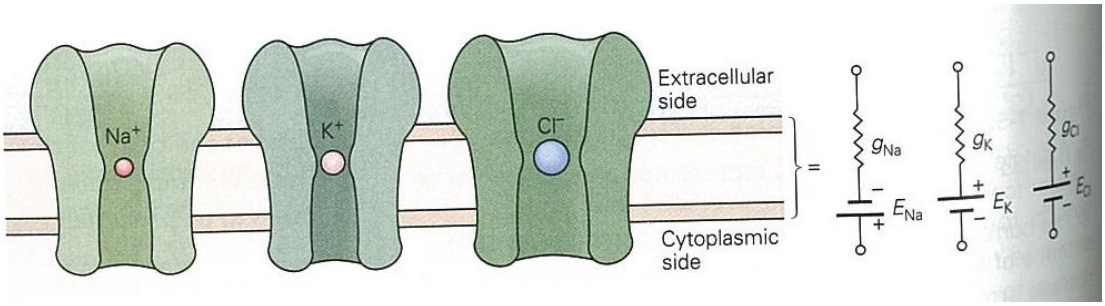

Figure 1.3. Each ion channel is selective for Na^+, K^+, or Cl^- and a population of ion channels can be represented by a battery in series with a conductor. Note the directions of poles of batteries, indicating a negative electromotive force for K^+ and Cl^- and a positive one for Na^+. This figure was reprinted, with permission, from Principles of Neural Science, 4th edition, Kandel E, Schwartz J, Jessel T, ⓒ McGraw-Hill Medical (2000).

These mechanisms of the changes in channel conductance and the membrane current are quantitatively described by the Hodgkin-Huxley equation (Dayan et al., 2005):

$$I_{\mathrm{m}} = \bar{g}_L(V - E_L) + \bar{g}_K n^4 (V - E_K) + \bar{g}_{Na} m^3 h (V - E_{Na}) \tag{1.5}$$

$$\frac{dn}{dt} = \alpha_{\mathrm{n}}(1 - n) - \beta_{\mathrm{n}} n \tag{1.6}$$

$$\frac{dm}{dt} = \alpha_{\mathrm{m}}(1 - m) - \beta_{\mathrm{m}} m \tag{1.7}$$

$$\frac{dh}{dt} = \alpha_{\mathrm{h}}(1 - h) - \beta_{\mathrm{h}} h \tag{1.8}$$

$$\alpha_{\mathrm{n}} = \frac{0.01(V + 55)}{1.0 - \exp\left(-0.1(V + 55)\right)} \tag{1.9}$$

$$\beta_{\mathrm{n}} = 0.125 \exp\left(-0.0125(V + 65)\right) \tag{1.10}$$

$$\alpha_{\mathrm{m}} = \frac{0.1(V + 40)}{1.0 - \exp\left(-0.1(V + 40)\right)} \tag{1.11}$$

$$\beta_{\mathrm{m}} = 4.0 \exp\left(-0.0556(V + 65)\right) \tag{1.12}$$

$$\alpha_{\mathrm{h}} = 0{,}07 \exp\left(\frac{V}{20}\right) \tag{1.13}$$

$$\beta_{\mathrm{h}} = \frac{1.0}{1.0 + \exp\left(-0.1(V + 35)\right)} \tag{1.14}$$

where V is the membrane potential, E_L is the equilibrium potential of leak channels, E_K is the equilibrium potential of potassium channels, E_{Na} is the equilibrium potential of sodium channels, $\bar{g}_L$ is the conductance of leak channels, $\bar{g}_K$ is the maximal conductance of potassium channels,

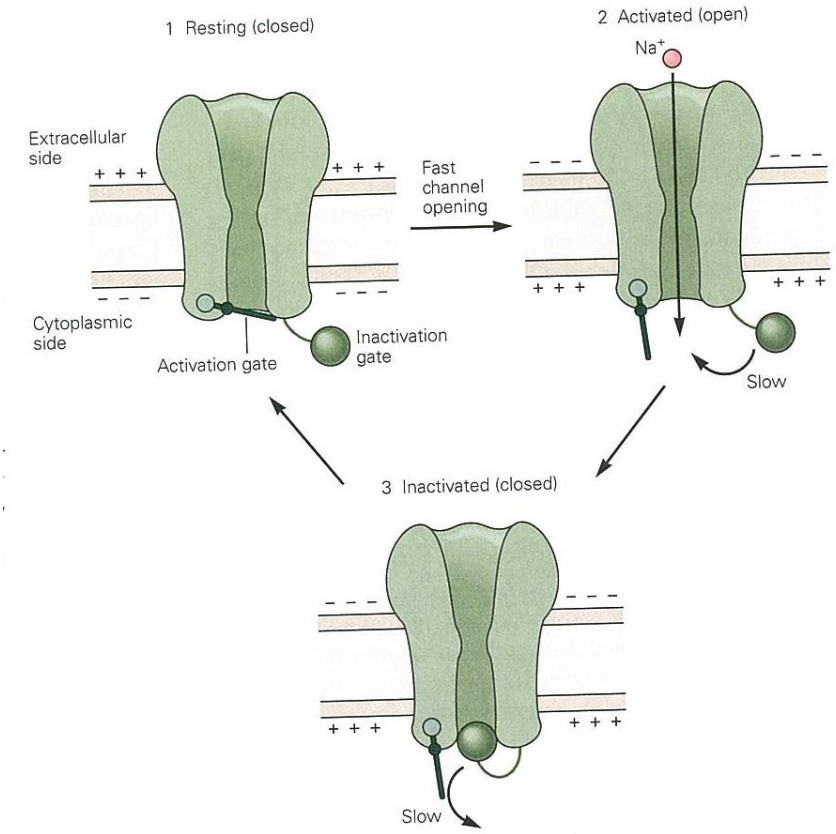

Figure 1.4. Illustration of the position of the activation and inactivation gates when the channel is at rest (1), when the sodium channels have been opened (2), and when the channels have been inactivated (3). It is the movement of the positive charge on the activation gate through the membrane electric field that generates the gating current. This figure was reprinted, with permission, from Principles of Neural Science, 4th edition, Kandel E, Schwartz J, Jessel T, ⓒ McGraw-Hill Medical (2000).

$\bar{g}_{Na}$ is the maximal conductance of potassium channels, and *n*, *m*, and *h* are the variables that represent the opening and closing of ion channels. The equivalent circuit is shown in Figure 1.5.

At the resting membrane potential, the ion channels are closed, and the channel conductance is low. When the membrane potential rises, the ion channels open, and the channel conductance increases, which causes the membrane current to move towards the equilibrium potential. At first, the membrane potential rises towards the equilibrium potential of sodium ions (+55 mV) and then falls towards that of potassium ions (-75 mV) because the sodium channels open at a lower membrane potential than the potassium channels do. After that, the membrane potential returns to the steady state during the refractory period (Figure 1.2).

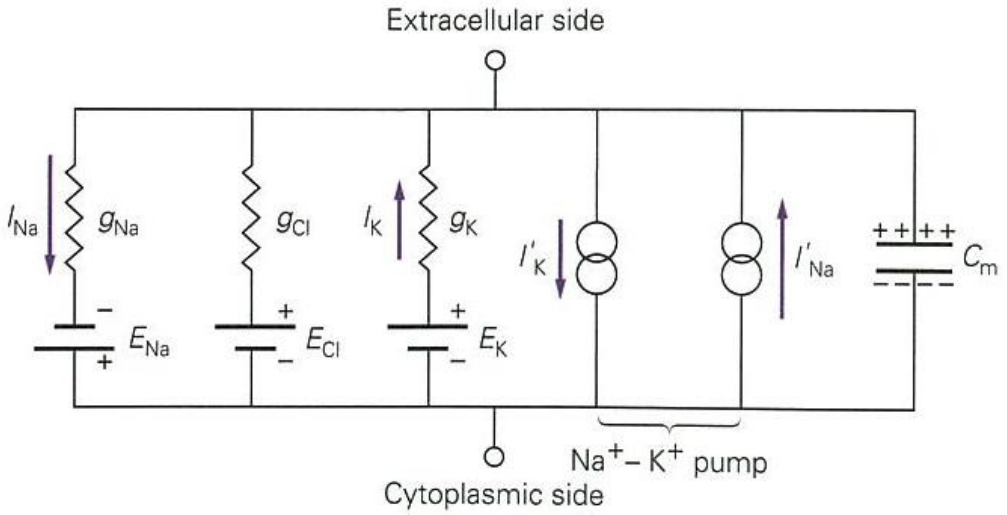

Figure 1.5. The equivalent circuit of Hodgkin-Huxley equation. Under steady state conditions the passive sodium and potassium currents are balanced by active sodium and potassium fluxes (I_{Na} and I_K) driven by the $Na^+ - K^+$ pump. The lipid bilayer endows the membrane with electrical capacitance (C_m). This figure was reprinted, with permission, from Principles of Neural Science, 4th edition, Kandel E, Schwartz J, Jessel T, ⓒ McGraw-Hill Medical (2000).

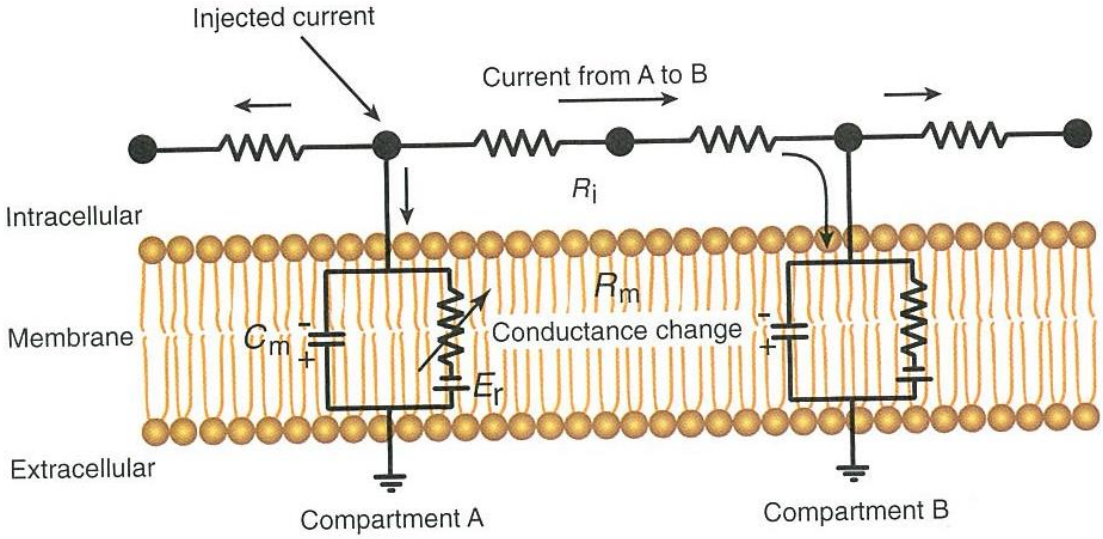

Figure 1.6. The equivalent circuit of two neighboring compartments or segments (A and B) of an axon or dendrite shows the pathways for current spread in response to an input (injected current or increase in membrane conductance) at segment A. This figure was reprinted, with permission, from Fundamental Neuroscience, Third Edition, Squire LR, Bloom FE, Spitzer NC, Darwin B, Lac S, Ghosh A, ⓒAcademic Press (2008).

1.1.4 Cable theory

The current generated at a point on the membrane affects other areas. The effects are described by cable theory, which is derived under the approximation of a neuron as a one-dimensional cable (Squire et al., 2008). Assuming a compartment model that discretizes the homogenous cable of d diameter into a compartment of Δx length, the equivalent circuit can be modeled as shown in Figure 1.6. From Kirchhoff's law, the following equation holds in this circuit:

$$c_{\mathrm{m}}\frac{dV_j}{dt} + I_j\Delta x = \frac{V_{j+1} - V_j}{r_i} + \frac{V_{j-1} - V_j}{r_i} \tag{1.15}$$

where V_j and I_j are the membrane potential and the membrane current density at compartment j, respectively. The conductance of the membrane (c_{m}) is proportional to the area of the membrane of the compartment ($\pi d\Delta x$) because the cable is homogenous. However, the resistance in the cell (r_i) is proportional to Δx and inversely proportional to the cross-sectional area $\pi\left(\frac{d}{2}\right)^2$. Consequently, we can define C_m and R_i as $c_{\mathrm{m}} = C_m\pi d\Delta x$ and $r_i = R_i\Delta x/\pi\left(\frac{d}{2}\right)^2$, and the following equation is derived:

$$C_{\mathrm{m}}\frac{dV_j}{dt} + I_j = \frac{d}{4R_i}\frac{V_{j+1} - 2V_j + V_{j-1}}{\Delta x^2} \tag{1.16}$$

.

Taking the limit of $\Delta x \to 0$, we can derive a continuous equation about the membrane potential V_m and the membrane current I_m on the cable, as shown below:

$$C_{\mathrm{m}}\frac{dV_m}{dt} + I_m = \frac{d}{4R_i}\frac{d^2V_m}{dx^2} \tag{1.17}$$

.

This equation is called the cable theory. Active currents described by the Hodgkin-Huxley equation and passive currents described by cable theory make a pair of a current sink and a current source on the membrane, as shown in Figure 1.7. A NEURON simulator (Hines, 1998) can simulate the dynamics of the membrane potential and the membrane current at each point in the structure of a neuron by using cable theory.

1.1.5 Variety of electrophysiological properties

It is known that there are several types of neurons that have different electrophysiological properties that generate action potentials (Squire et al., 2008). No uniform classification scheme has been formulated, but some characteristic patterns of activity can be found, as shown in Figure 1.8. The general classes of the characteristic patterns are elucidated below.

- Linear: Neurons that generate one spike at a time. The more prolonged and intense their depolarization, the more they generate action potentials. They are typical for brain stem and spinal cord motor neurons.
- Regular firing: Neurons that produce trains of action potentials that show a tendency to slow down in frequency with time (spike frequency adaptation). Examples of such neurons are cortical and hippocampal pyramidal cells.
- Bursting: Neurons that generate clusters of action potentials when the membrane is brought above the threshold. Examples of such neurons are thalamic relay neurons, inferior olivary neurons, and some types of cortical and hippocampal pyramidal cells.
- Fast spiking: Neurons that generate short duration (<1ms) action potentials and that can discharge at high frequencies (>300 Hz). Such electrophysiological properties are often found in inhibitory neurons, such as interneurons in the cerebral cortex, thalamus, and hippocampus.

Such variability is produced by multiple types of active conductance (Squire et al., 2008). For example, two distinct Na^+ currents and five distinct K^+ currents are shown in Table 1.1 and Table 1.2. Furthermore, four distinct Ca^{2+} currents and the current that conducts both Na^+ and K^+ are shown in Table 1.3 and Table 1.4. They are not modeled in the original Hodgkin-Huxley equation, but various distinctive activities of neurons are produced by them. Simulations of the Hodgkin-Huxley equation with different conductances can reproduce a variety of generated action potentials, as shown in Figure 1.9.

Although these currents can dramatically change how action potentials are generated, all neurons have a refractory period because all of the action potentials are started by I_{Nat} which is inactivated after the activation. However, it is known that the shapes of action potentials are not homogenous during bursting or tonic firing (Figure 1.8 and Figure 1.9).

Table 1.1. Types of Na^+ currents (Squire et al., 2008).

I_{Nat}	"transient", inactivated after activation, modeled in the classical Hodgkin-Huxley equation
I_{Nap}	"persistent", not inactivated after activation, changing responsiveness of neurons

Table 1.2. Types of K^+ currents (Squire et al., 2008).

I_K	not inactivated after activation, modeled in the classical Hodgkin-Huxley equation
I_C	voltage- and Ca^{2+}-dependent current
I_A	inactivated after activation, controlling the rate of generation of action potentials
I_M	modulated by the activation of neurotransmitter receptors (e.g. acetylcholine)
I_{AHP}	voltage- and Ca^{2+}-dependent current, producing after-hyper-polarization

Table 1.3. Types of Ca^{2+} currents (Squire et al., 2008).

I_L	"long-lasting", high-threshold, not inactivated after activation
I_T	"transient", low-threshold, inactivated after activation, producing bursting
I_N	"neither", high-threshold, inactivated after activation
I_P	"Purkinje", high-threshold, not inactivated after activation

Table 1.4. The current conducted by Na^+ and K^+ (Squire et al., 2008).

I_h	Activated by hyperpolarization, related to rhythmic oscillations

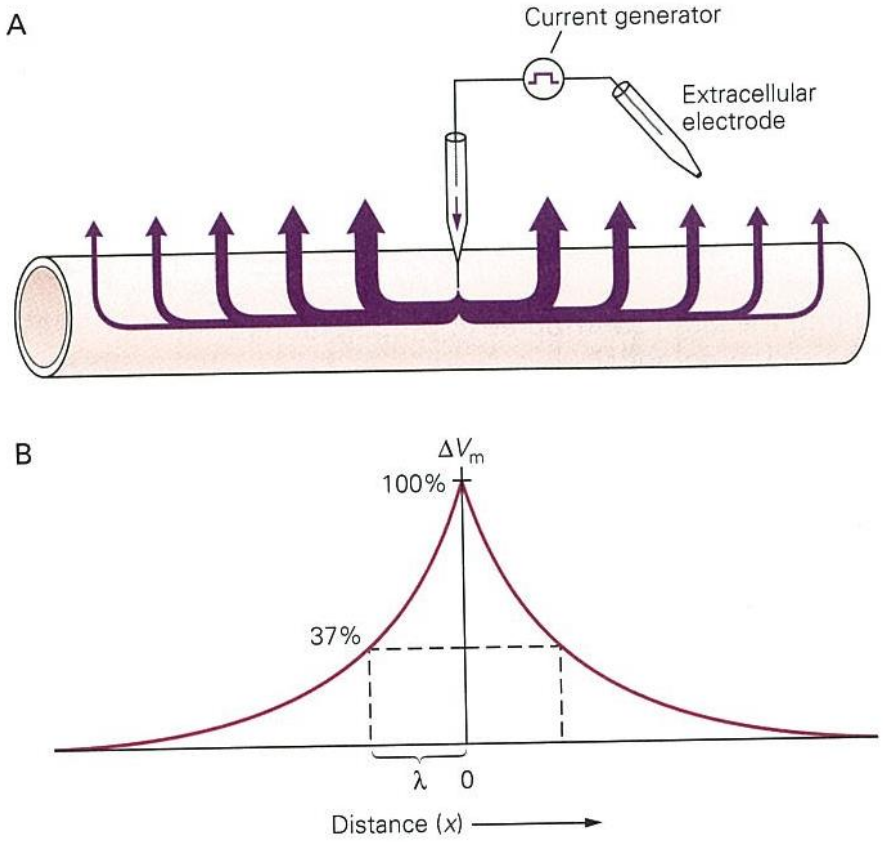

Figure 1.7. The voltage response in a passive neuronal process decays with distance due to electronic conduction. Current injected into a neuronal process by a microelectrode follows the path of least resistance to the return electrode in the extracellular fluid (A). The thickness of the arrows represents membrane current density at any point along the process. Under these conditions the change in V_m decays exponentially with distance from the site of current injection (B). The distance at which ΔV_m has decayed to 37% of its value at the point of current injection defines the length constant, λ. This figure was reprinted, with permission, from Principles of Neural Science, 4th edition, Kandel E, Schwartz J, Jessel T, ⓒ McGraw-Hill Medical (2000).

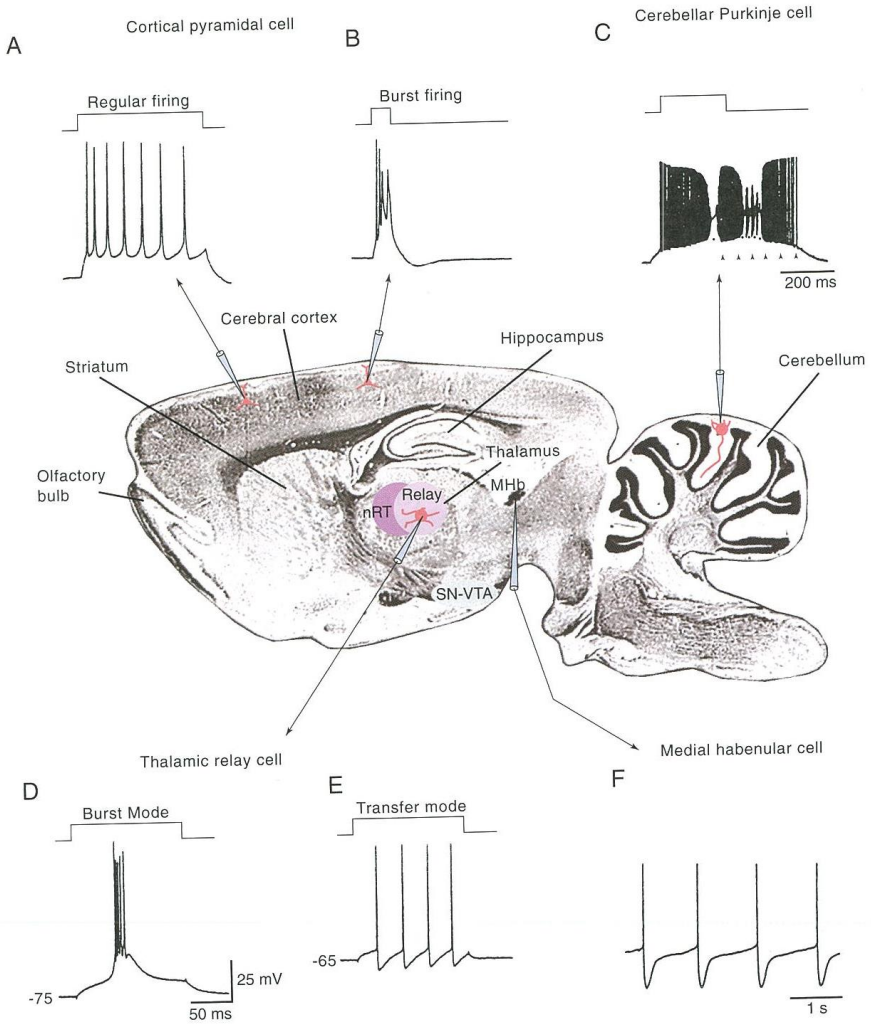

Figure 1.8. Neurons in the mammalian brain exhibit widely varying electrophysiological properties. (A) Intracellular injection of a depolarizing current pulse in a cortical pyramidal cell results in a train of action potentials that slow down in frequency. This pattern of activity is known as "regular fi ring." (B) Some cortical cells generated bursts of three or more action potentials, even when depolarized only for a short period of time. (C) Cerebellar Purkinje cells generate high-frequency trains of action potentials in their cell bodies that are disrupted by the generation of Ca^{2+} spikes in their dendrites. These cells can also generate "plateau potentials" from the persistent activation of Na^{+} conductances (arrowheads). Thalamic relay cells may generate action potentials either as bursts (D) or as tonic trains of action potentials (E) due to the presence of a large low-threshold Ca^{2+} current. (F) Medial habenular cells generate action potentials at a steady and slow rate in a "pacemaker" fashion. This figure was reprinted, with permission, from Fundamental Neuroscience, Third Edition, Squire LR, Bloom FE, Spitzer NC, Darwin B, Lac S, Ghosh A, ⓒAcademic Press (2008).

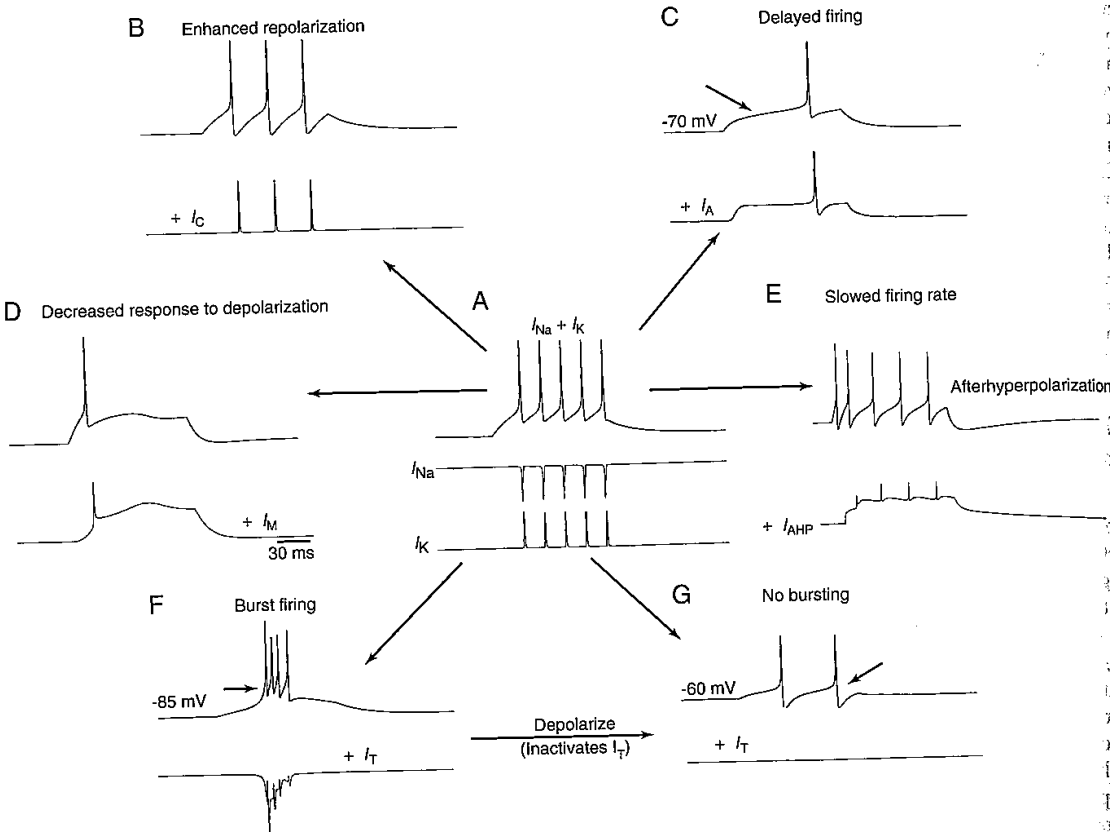

Figure 1.9. Simulation of the effects of the addition of various ionic currents to the pattern of activity generated by neurons in the mammalian central nervous system. (A) The repetitive impulse response of the classical Hodgkin–Huxley model (voltage recordings above, current traces below). With only I_{Na} and I_K, the neuron generates a train of five action potentials in response to depolarization. Addition of I_C (B) enhances action potential repolarization. Addition of I_A (C) delays the onset of action potential generation. Addition of I_M (D) decreases the ability of the cell to generate a train of action potentials. Addition of I_{AHP} (E) slows the firing rate and generates a slow after-hyperpolarization. Finally, addition of the transient Ca^{2+} current I_T results in two states of action potential firing: (F) burst firing at −85 mV and (G) tonic firing at −60 mV. This figure was reprinted, with permission, from Fundamental Neuroscience, Third Edition, Squire LR, Bloom FE, Spitzer NC, Darwin B, Lac S, Ghosh A, ©Academic Press (2008).

1.2 Recording of neural activity

1.2.1 Intracellular voltage recording

As mentioned above, an action potential is an important phenomenon that realizes information processing in the brain. Therefore, electrophysiological measurements of action potentials have been a major approach used in neuroscience. The most reliable method for measuring action potentials is intracellular voltage recording, which is realized by the insertion of an electrode into a neuron or patch-clamp techniques that use electrodes in glass pipettes attached to the membrane of a neuron. This method has the advantage of a fine signal/noise ratio, as shown in Figure 1.10, and it enables the measurement of small changes in the membrane potential. Therefore, this method has been used to measure not only action potentials but also small changes in the membrane potential caused by synaptic transmissions (post synaptic potentials) (Lampl et al., 1999; Shu et al., 2003). However, this method requires delicate and time-consuming actions in order to measure from a neuron, and this makes multiunit recording difficult. Long-term recording is also difficult because the cell body is damaged by the recording.

1.2.2 Extracellular voltage recording

Multiunit and long-term recordings of action potentials can be realized easily by extracellular voltage recording, as shown in Figure 1.11. For example, Utah electrodes for recording *in vivo* (shown in Figure 1.12) and multi-electrode arrays (MEAs) for recording *in vitro* (shown in Figure 1.13) have been developed for multi-unit and long-term recordings. They have been used in many applications, such as brain-machine interface systems (Donoghue, 2002; Lebedev and Nicolelis, 2006), the recording of the development of cultured neuronal networks (Van et al., 2004; Steganga et al., 2008; Brewer et al., 2009; Ito et al., 2010), and research on the adaptation of neuronal networks to electrical stimulation (Ruaro et al., 2005; Chiappalone et al., 2008). However, this method has the disadvantage of a low signal/noise ratio. Although the change in the membrane voltage during action potential is approximately 100 mV, the voltage of the extracellularly recorded spikes is approximately 100 μV (Figure 1.10).

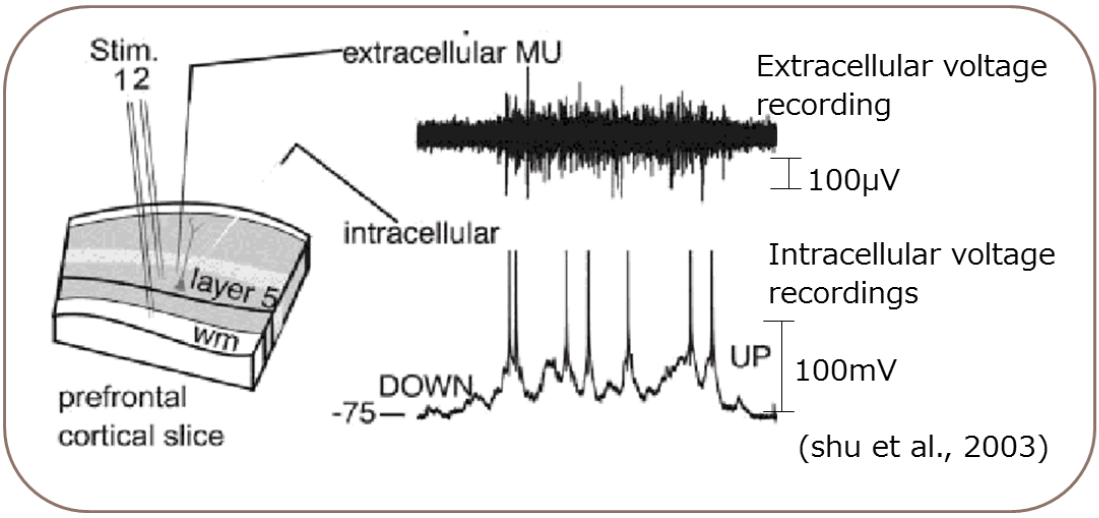

Figure 1. 10. Simultaneous extracellular recording in layer 5 and intracellular recording from a layer 5 cell. Reprinted and modified from Shu Y, Hasenstaub A, Badoual M, Bal T, McCormick DA. Barrages of Synaptic Activity Control the Gain and Sensitivity of Cortical Neurons, Journal of Neuroscience, Vol. 23, No. 32, pp. 10388-10401, Copyright (2003) Society for Neuroscience.

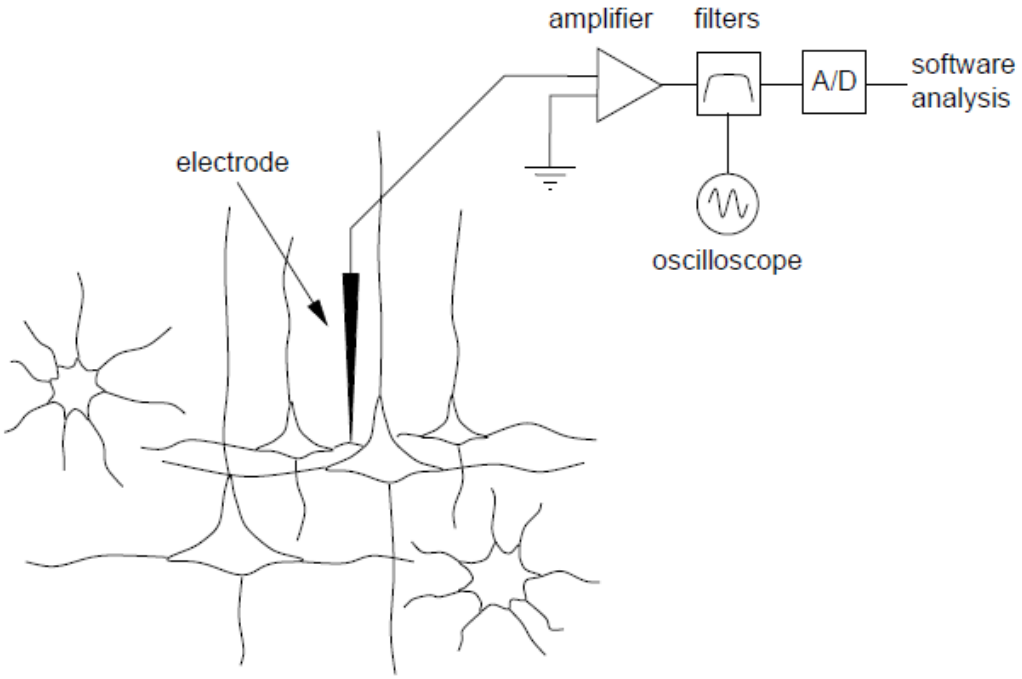

Figure 1.11. The basic set-up for measuring and analyzing extracellular neural signals. Lewicki MS, Network: Computation in Neural Systems, 1998;9(4):53-78, ⓒ(1998), Informa Healthcare. Reproduced with permission of Informa Healthcare.

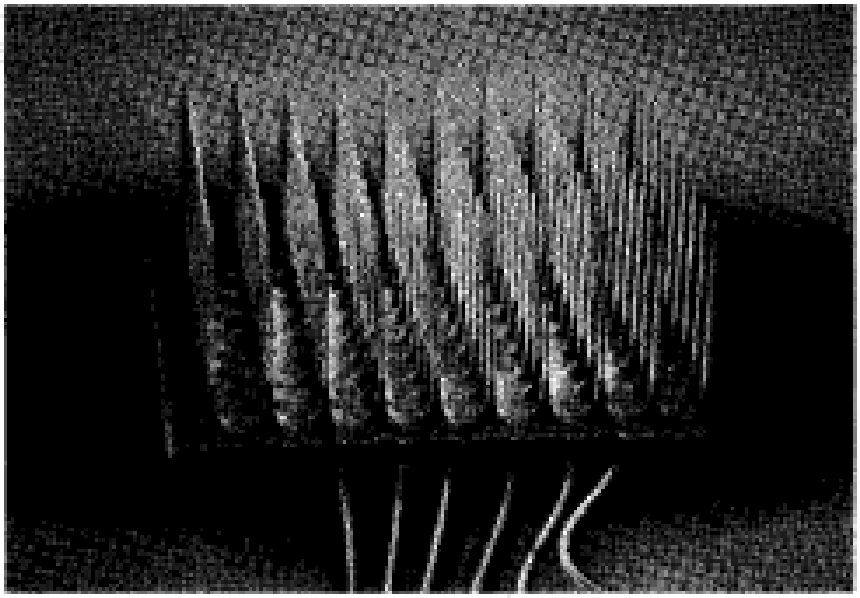

(a)

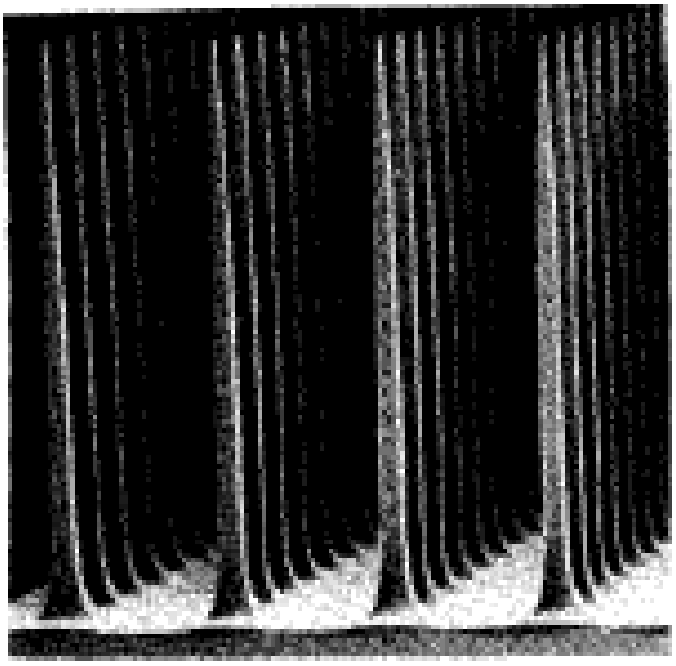

(b)

Fig. 1.12. (a) A scanning electron micrograph of a Utah electrode (silicon 100 electrode array). The center to center spacing between electrodes is 400 μm. (b) An enlarged view of a Utah electrode. © 1991 IEEE. Reprinted, with permission, from Campbell PK, Jones KE, Huber RJ, Horch KW, Normann RA. A silicon-based, three-dimensional neural interface: manufacturing processes for an intracortical electrode array, IEEE Transactions on Biomedical Engineering, 1991.

(a)

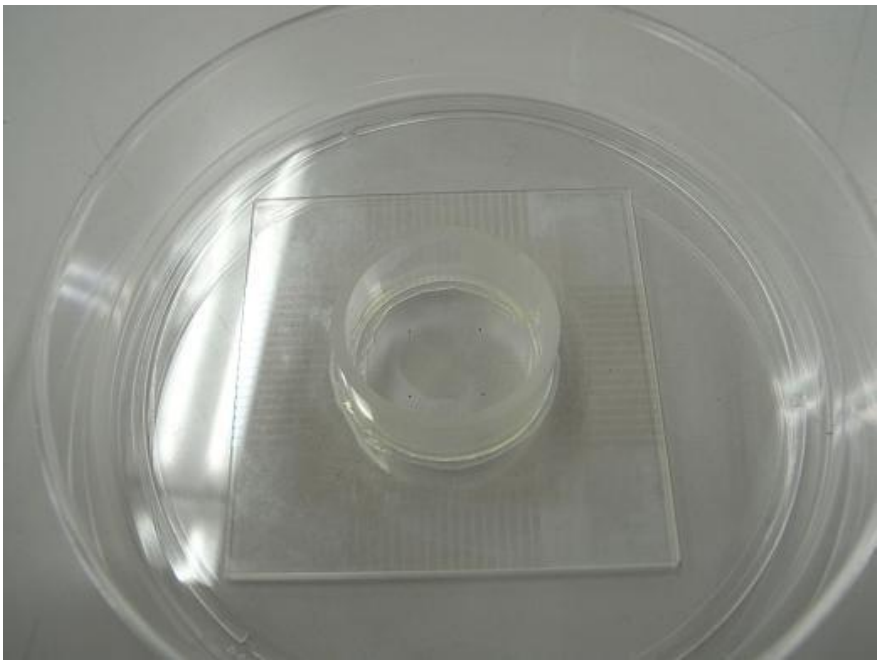

(b)

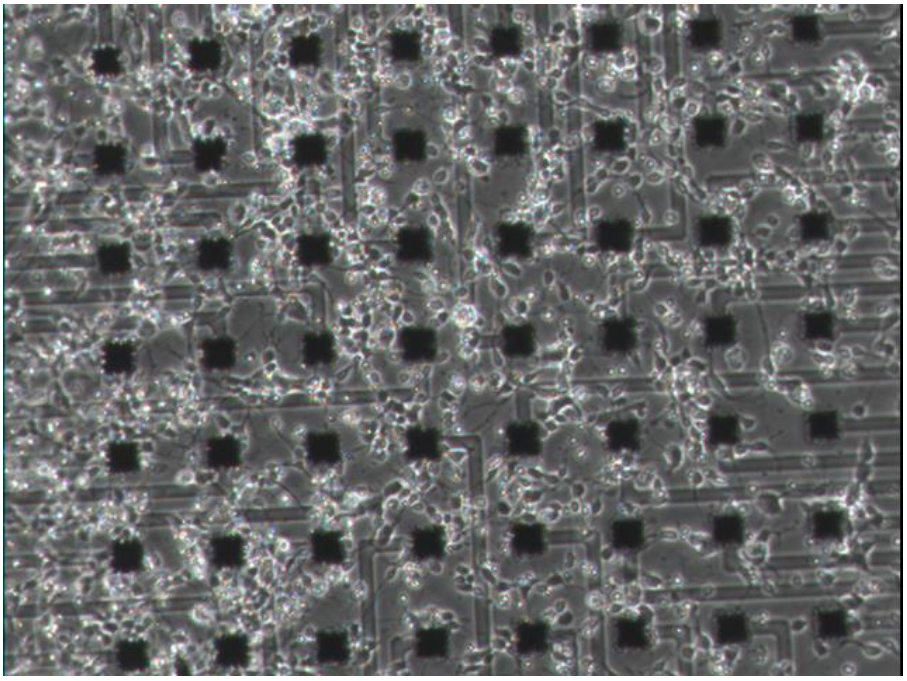

Figure 1. 13. (a) The appearance of Multi-electrode array (MED545A; Alpha MED Scientific Inc.). (b) Cortical neurons cultured on MEA. Black squares are 50μm square electrodes.

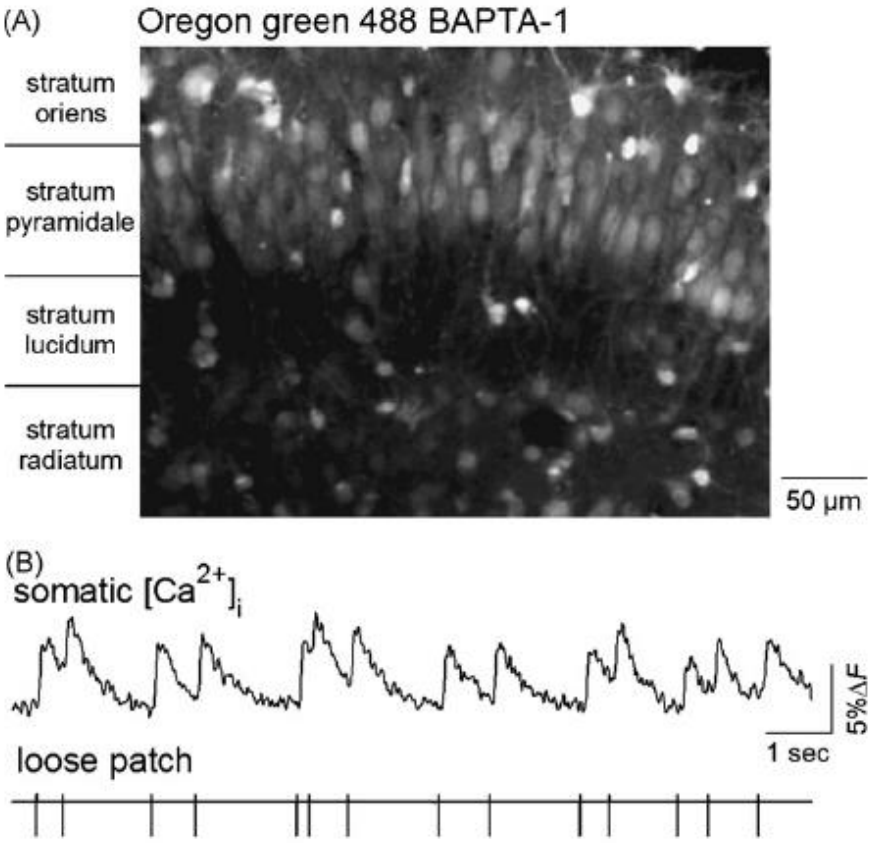

Figure 1.14. An example of calcium imaging. (A) Confocal image of the CA3 region in an organotypically cultured rat entorhino-hippocampal slice bolus-loaded with Oregon green 488 BAPTA-1. (B) Simultaneous monitoring of somatic calcium signal and loose-patch recording from the same neuron. Note that action potentials are mirrored in calcium transients. Reprinted from Takahashi N, Sasaki T, Usami A, Matsuki N, Ikegaya Y, Watching neuronal circuit dynamics through functional multineuron calcium imaging (fMCI), Neuroscience Research, Vol.58, No. 3, pp.219-225, ⓒ (2007), with permission from Elsevier.

1.2.3 Optical imaging

The excitation of neurons can also be observed optically with calcium ion fluorescent indicators (Takahashi et al., 2007) and voltage-sensitive dyes (Ferezou et al., 2006). For example, the concentration of calcium ions can be measured, as shown in Figure 1.14 (Takahashi et al., 2007). The estimation of spike timings from calcium signals has been realized (Vogelstein et al., 2009). The advantage of this method is the ability to record individually from a greater number of neurons than is possible with extracellular voltage recordings. However, a low signal/noise ratio, low time resolution, drug toxicity, and inapplicability to humans can be disadvantages.

1.3 Mechanisms of extracellular voltage recording

1.3.1 Polarization of electric charges in the extracellular medium

In the present thesis, we focus attention on extracellular voltage recording, which has many applications in neural engineering. In Section 1.2, we showed that the distributions of membrane currents during action potentials can be expressed by the Hodgkin-Huxley equation and cable theory. In this section, we discuss how the electric potential recorded at an extracellular electrode is determined from the distribution of the membrane currents.

First, we discuss the polarization of electric charges in the extracellular medium. Assuming an initial charge distribution ρ_0 in the homogeneous extracellular medium that has conductivity σ and permittivity ϵ at $t = 0$, Gauss's law

$$\nabla \cdot (\epsilon \mathbf{E}) = \rho \tag{1.18}$$

holds for an electric field $\mathbf{E}$ and charge distribution ρ. Furthermore, charge conservation

$$\nabla \cdot \mathbf{J} + \frac{\partial \rho}{\partial t} = 0 \tag{1.19}$$

and Ohm's law

$$\sigma \mathbf{E} = \mathbf{J} \tag{1.20}$$

hold for current distribution $\mathbf{J}$. From these three equations, we can derive the differential equation:

$$\frac{\partial \rho}{\partial t} = -\frac{\sigma}{\epsilon}\rho. \tag{1.21}$$

The solution of this equation is

$$\rho = \rho_0 \exp\left(-\frac{\sigma}{\epsilon}t\right) \tag{1.22}$$

which has the time constant $\frac{\epsilon}{\sigma}$ and the charge distribution ρ becomes $\rho = \left(\frac{1}{e}\right)^n \rho_0$ after $n\frac{\epsilon}{\sigma}$.

Because $\sigma \approx 1\,\mathrm{S/m}$ and $\epsilon \approx 10^{-10}\,\mathrm{F/m}$ (Bedard et al., 2004), $\frac{\epsilon}{\sigma}$ is approximately 10^{-10} s. Therefore, the electric field produced by the polarization of charges can be ignored when we consider action potentials that have a millisecond time scale.

1.3.2 The extracellular potential produced by a single current source

Next, we consider the potential produced by the current density distribution. We assume a current source with magnitude I in the homogeneous extracellular medium that has conductivity σ and permittivity ϵ. In the homogenous field, the current outspreads along a sphere centered at the current source. The magnitude of the current density on the surface of the sphere of radius r' centered on

the current source is

$$j(r') = \frac{I}{4\pi r^2} \tag{1.23}$$

Ohm's law implies a spherically symmetric electric field that has outward direction, and the magnitude is calculated as

$$E(r') = \frac{1}{\sigma} j(r') = \frac{I}{4\pi\sigma r^2}. \tag{1.24}$$

Consequently, the electric potential at the point at distance r from the current source is

$$V(r) = -\int_{\infty}^{r} E(r')\,dr' = \frac{I}{4\pi\sigma r} \tag{1.25}$$

(Holt et al., 1998; Bedard et al., 2004; Gold et al., 2006).

1.3.3 The relationship between the intracellular potential and the extracellular potential

Assuming a single-compartment model and no input current, the Hodgkin-Huxley equation is

$$I = -C_{\mathrm{m}} \frac{dV_m}{dt}. \tag{1.26}$$

Therefore,

$$V(r) \approx -\frac{1}{4\pi\sigma r} C_{\mathrm{m}} \frac{dV_m}{dt} \propto -\frac{dV_m}{dt}. \tag{1.27}$$

Therefore, the extracellular voltage signal is proportional to the negative of the first derivative of the intracellular voltage signal, as shown in Figure 1.17(A). However, Henze et al. (2000) have reported experimental data that show that this approximation is true in the initial ascending phase of the action potential but it breaks up in the descending phase after the initial ascending phase (Figure 1.15). One possible reason is that a whole cell cannot be approximated as a single compartment except in the initial phase of the action potential. An action potential that starts at one part of the membrane influences the rest areas by cable theory and propagates through the cell. After propagation, a single compartment is insufficient to describe the extracellular potential produced by the complicated distribution of membrane currents.

1.3.4 The extracellular potential produced by distributed membrane currents

When there are distributed active and passive membrane currents described by cable theory, the extracellular potential is calculated by summing the effects from multiple current sources. When *N* current sources exist and the *i*-th current source position is $\mathbf{r}_n$ and has the magnitude I_n, the

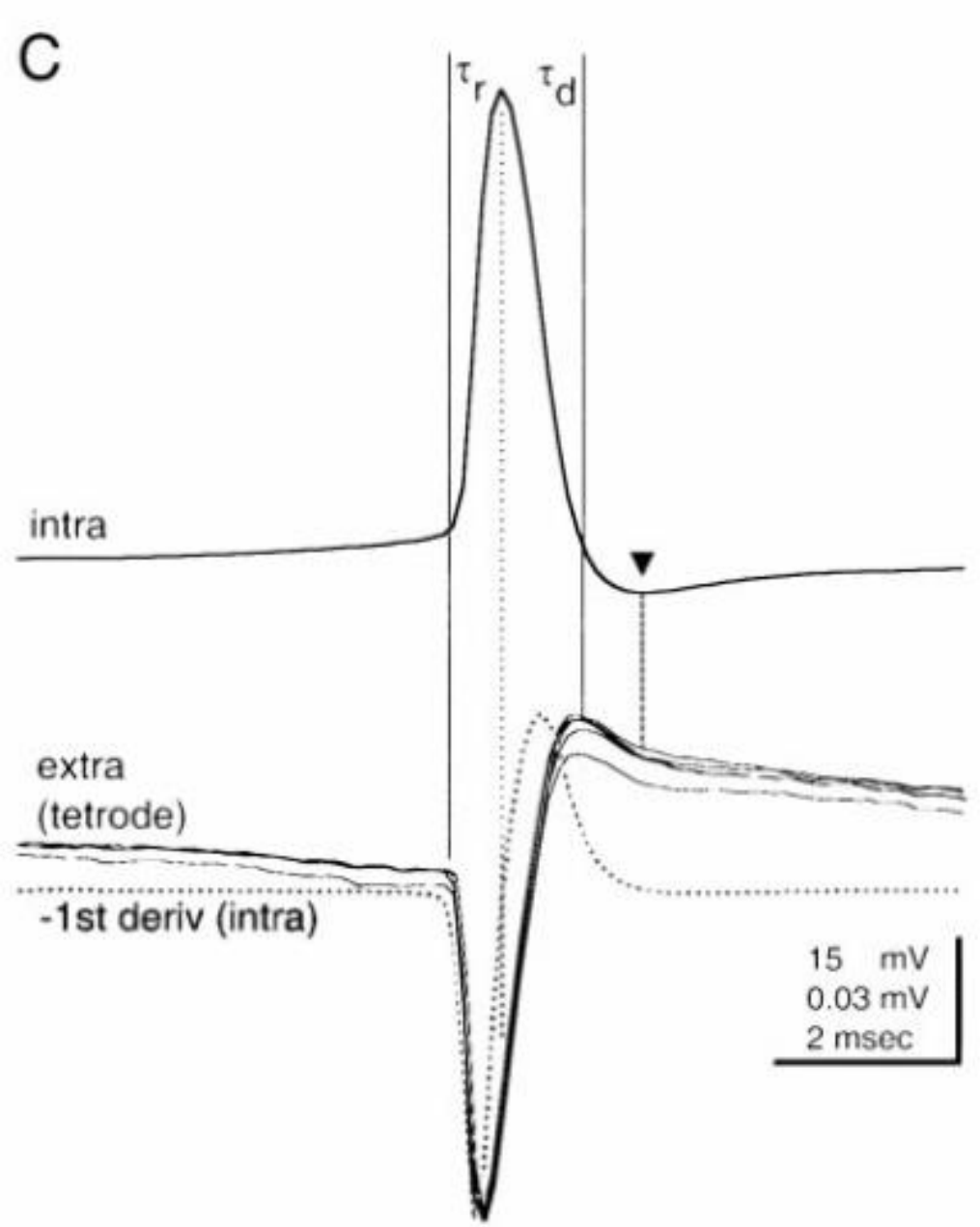

Figure 1.15. Simultaneous intracellular and extracellular voltage recording of an action potential from a pyramidal cell in hippocampus CA1. Intracellularly-recorded signal corresponds to membrane potential. The dotted line superposed on extracellularly-recorded voltage signal is the negative of the first derivative of intracellularly-recorded voltage signal. Reprinted from Henze DA, Borhegyi Z, Csicsvari J, Mamiya A, Harris KD, Buzsaki G. Intracellular features predicted by extracellular recordings in the hippocampus in vivo, Journal of Neurophysiology Vol. 84, No. 1 pp. 390-400, ⓒ (2000) American Physiological Society.

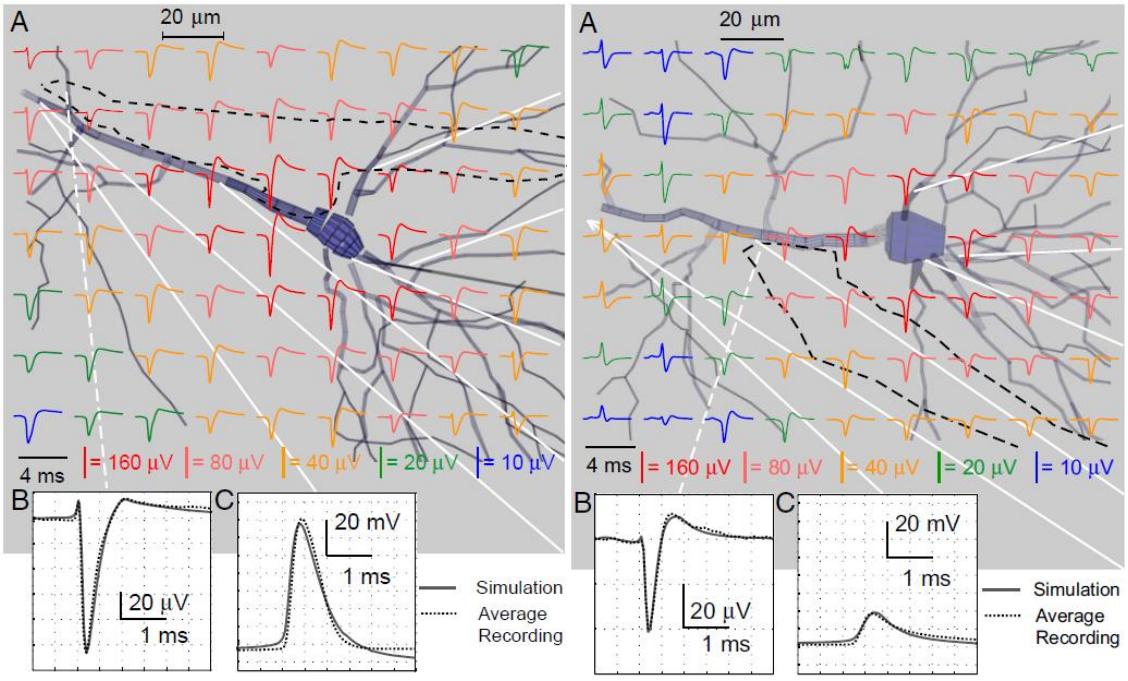

Figure 1.16. Recording and simulation of extracellular recording of action potentials from two different neurons. A: (Left) Extracellular action potentials in the transverse section containing the soma and the tip of the electrode track (dotted line). (Right) Extracellular action potentials in the transverse section containing the tip of electrode track (dotted line), about 5 μ m caudal to the soma and apical trunk (the z-axis is the axis perpendicular to the plane of the section). B: Comparison of extracellular recording (strongest channel of the tetrode) and simulation at the estimated electrode position. C: (Right) Comparison of the average intracellular recording with the simulated spike in the proximal apical trunk. (Left) Comparison of intracellular recording and the simulation in the apical trunk approximately 120 m from the soma. Reprinted from Gold C, Henze DA, Koch C, Buzsaki G. On the origin of the extracellular action potential waveform: a modeling study, Journal of Neurophysiology Vol. 95, No.5, pp. 3113-3128, ⓒ (2006) American Physiological Society.

electric potential at $\mathbf{r}$ is calculated from the superposition principle:

$$V(\mathbf{r}) = \sum_{n=1}^{N} \frac{I_n}{4\pi\sigma|\mathbf{r} - \mathbf{r}_n|}. \tag{1.28}$$

For a linear single current source having length Δs, the potential is

$$V(r,h) = \frac{1}{4\pi\sigma}\int_{-\Delta s}^{0} \frac{Ids}{\Delta s\sqrt{r^2 + (h-s)^2}} = \frac{I}{4\pi\sigma\Delta s}\log\left(\frac{\sqrt{h^2 + r^2} - h}{\sqrt{l^2 + r^2} - l}\right) \tag{1.29}$$

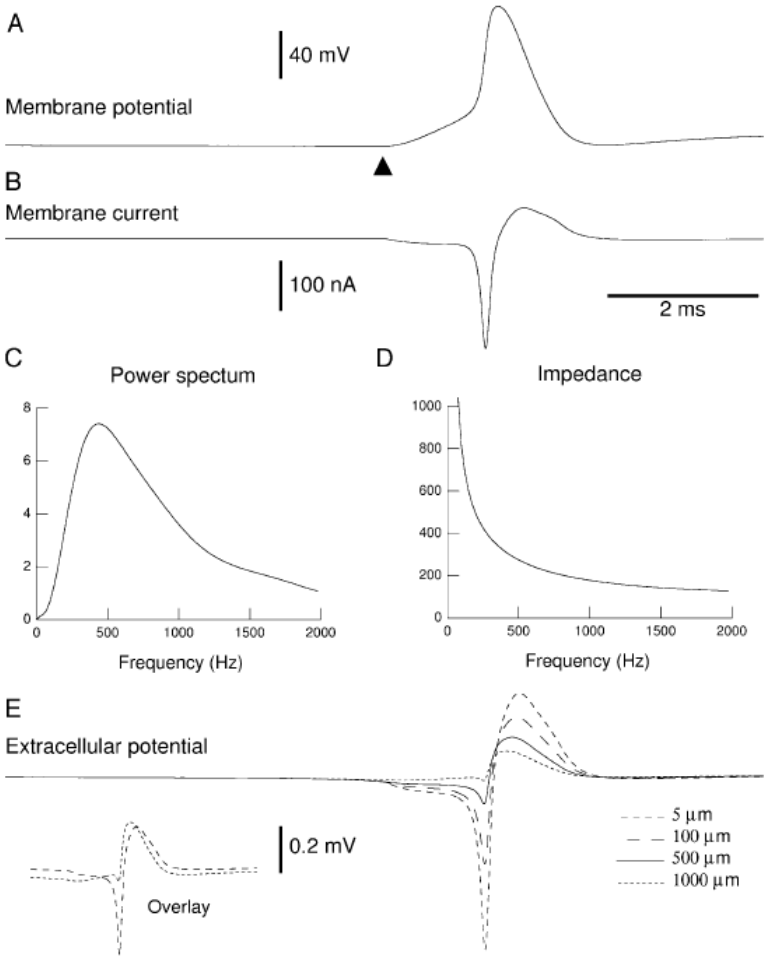

Figure 1.17. Frequency-filtered extracellular field potentials in a conductance-based model. (A) Membrane potential of a single-compartment model containing voltage-dependent sodium and potassium conductances and a glutamatergic synaptic conductance. The glutamatergic synapse was stimulated at t ¼ 5 ms (m) and evoked an action potential. (B) Total membrane current generated by this model. Negative currents correspond to sodium and glutamatergic conductances (inward currents), whereas positive currents correspond to potassium conductances (outward currents). (C) Power spectrum of the total current shown in B. (D) Impedance at 500 mm from the current source assuming a radial profile of conductivity and permittivity. (E) Extracellular potential calculated at various distances from the source (5, 100, 500, and 1000 mm). The frequency filtering properties can be seen by comparing the negative and positive deflections of the extracellular potential. The fast negative deflection almost disappeared at 1000 mm whereas the slow positive deflection was still present. The inset in E (Overlay) shows the traces at 5 and 1000 mm overlaid. Reprinted from Bedard C, Kroger H, Destexhe A, Modeling extracellular field potentials and the frequency-filtering properties of extracellular space, Biophysical Journal, Vol.86, No. 3, pp.1829-1842, Copyright (2004), with permission from Elsevier.

at the point where the radial distance from the line is r, the longitudinal distance from the end of the line is h, and the distance from the start of the line is $l = \Delta s + h$. Gold et al. (2006) have simulated spike shapes recorded at various points in extracellular medium around a neuron with this equation and the NEURON simulator and they were able to obtain good approximations of actual measurements (Figure 1.16).

However, we cannot ignore the effects of inhomogenous permittivity and conductivity that are observed in many areas in the brain. In such conditions, Bedard et al. (2004) have shown that the impedance of the extracellular medium shows low-pass filtering characteristics [Figure 1.17(D)] and that more high-frequency contents are reduced with distance between the neuron and the recording point [Figure 1.17(E)].

As described above, extracellularly recorded spike shapes show a variety of amplitudes and shapes affected by a number of factors, including the structure of the neurons and the neurites, distribution of the membrane currents, position of the extracellular electrode, and inhomogeneity of extracellular medium.

1.4 Signal processing for neural spikes

1.4.1 Extraction of neural activity from extracellular voltage signals

In the present thesis, we discuss the methods used to extract neural activity from extracellular neural signals. Two types of neural activities are normally recorded by extracellular voltage recording: the local field potential (LFP) and spikes.

LFP is the low-frequency signal that mainly reflects synchronous postsynaptic potentials in the broad area around an electrode (B´edard et al., 2004; Buszaki et al., 2012). LFP is often analyzed in time-frequency representation with a Fourier analysis or wavelet analysis (Heldman et al., 2006; Slutzky et al., 2011; Zhang et al., 2011).

Spikes are also important components. They are high-frequency transient signals produced by the action potentials of the neurons around the electrode. However, as mentioned in Sections 1.2 and 1.3, the voltage of extracellularly recorded spikes is so low that their shapes are strongly distorted by external noise. Furthermore, spikes generated from several neurons are often recorded with an electrode (multiunit recording). Because of these two reasons, techniques that extract single-unit spike trains from multiunit extracellular recordings have been a major subject of research.

1.4.2 Spike detection and sorting

The detection and classification of neural spikes in order to extract spike trains of each single neuron from multiunit extracellular voltage recordings, which is often referred to as spike detection

and spike sorting, are basic techniques used in neural engineering and neuroscience (Lewicki, 1998; Brown et al. 2004).

Spike sorting has been typically based on the assumption that spike shapes recorded from the same neuron are similar and that spikes recorded from different neurons have different waveforms (an example is shown in Figure 1.18). As shown in Sections 1.2 and 1.3, spikes from a neuron have similar shapes in the same structure of the neuron and with the same position of the recording electrode, except for bursting neurons or other neurons that have special firing properties. Conversely, different spike shapes are obtained from different neurons with different structures and different distances to the electrode. Therefore, if we want to obtain the spike trains of each single neuron recorded from multiunit recordings, we have to detect spike shapes and classify them into groups. There are a large number of methods that detect and sort spikes by using feature quantities extracted from spike waveforms. For example, methods that use the height of spikes (Maccione et al., 2009), principal component analyses (Lewicki et al., 1998), and wavelet transforms (Hulata et al., 2002; Quian Quiroga et al., 2004) have been proposed. These methods often have lower computational costs than the direct computation of spike waveforms because of the reduced dimension of the processed data.

For off-line use, spike sorting can be interpreted as an estimation problem of the unique spike shape (spike templates) and spike timings that correspond to each neuron. In many previous spike-sorting methods, spikes in the recorded signal were extracted by detecting voltage signals that exceeded a predefined threshold, and the extracted waveforms were classified by some clustering method to obtain the spike templates and spike timings (Yang and Shamma, 1988; Shoham et al., 2003; Quian Quiroga et al., 2004; Thakur et al., 2007; Kim and McNames, 2007; Takekawa et al., 2010).

Furthermore, robust and computationally efficient real-time spike sorting methods are required for applications such as brain-machine interfaces (Donoghue, 2002; Lebedev and Nicolelis, 2006; Sato et al., 2007) and real-time experimental feedback systems (Bakkum et al., 2008). Many previous real-time spike sorting systems have been constructed with two phases, a pre-processing phase to obtain spike templates and a real-time template-matching phase (Yang and Shamma, 1988; Thakur et al., 2007; Kim and McNames, 2007). In the pre-processing phase, spike waveforms are collected by detecting voltage signals that exceed a predefined threshold, and the mean spike shape corresponding to each neuron is obtained for use as a template by using a clustering method off-line. Then, in the real-time template-matching phase, spikes detected on the basis of the threshold are matched to those templates.

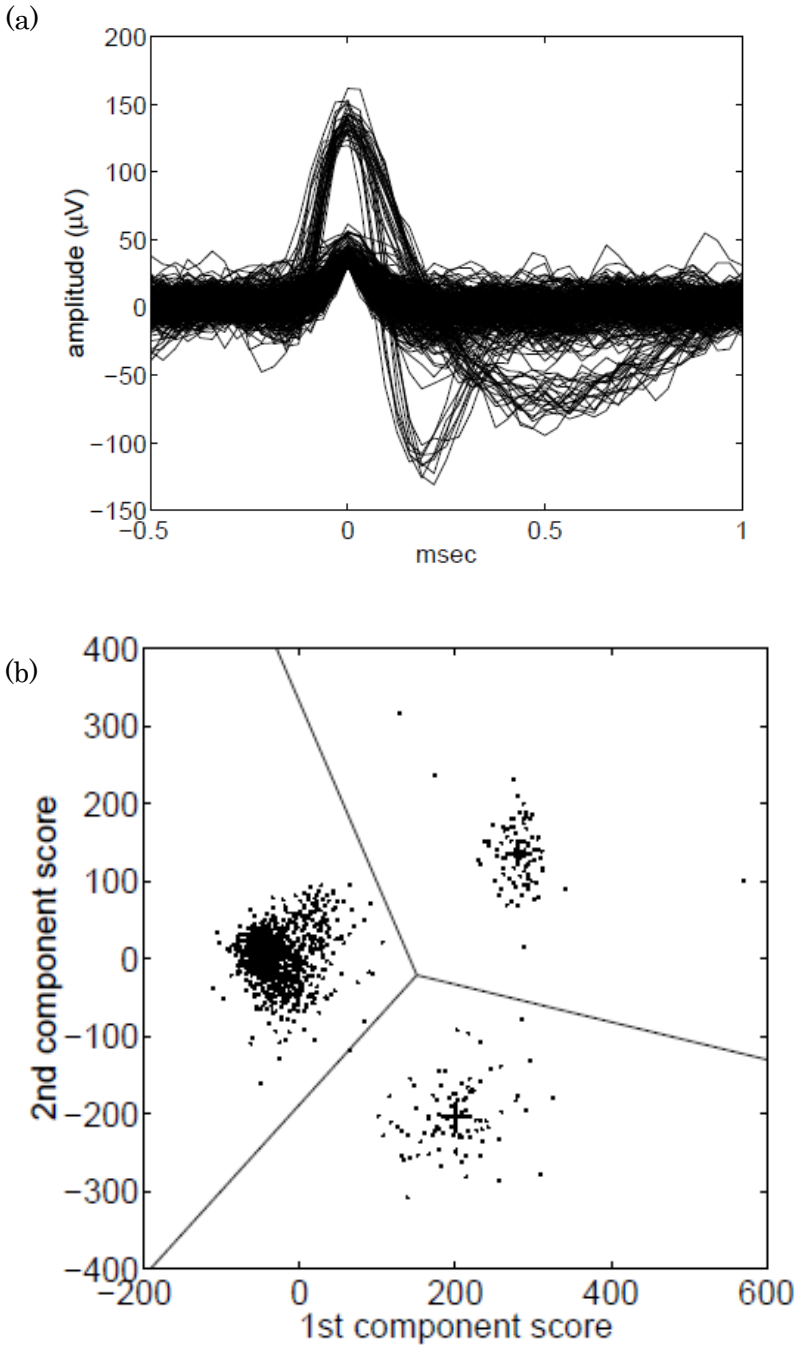

Figure 1.18. (a) Typical spike waveforms recorded by extracellular multi-unit recordings. (b) The plot of first and second principal component scores. Lines indicate the decision boundaries for nearest-neighbor clustering and + symbols indicate the cluster centers. In spike sorting, three clusters are considered to be spikes from different neurons. Lewicki MS, Network: Computation in Neural Systems, 1998;9(4):53-78, ⓒ(1998), Informa Healthcare. Reproduced with permission of Informa Healthcare.

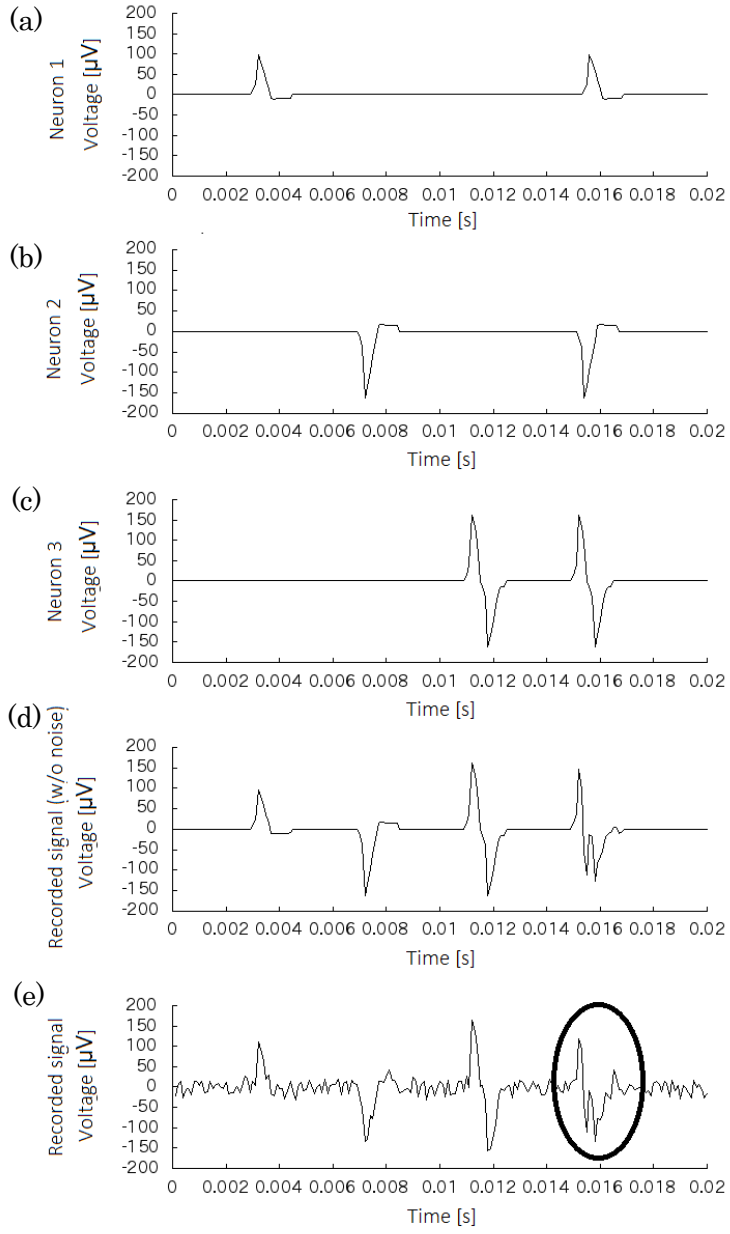

Figure 1. 19. Example of simulated spike overlapping. We assumed that three spike waveforms from three neurons were recorded and that these three waveforms appeared independently in the recording signal. However, the last one in the black circle is the waveform made by the overlap of the three spike waveforms. This waveform was interpreted as a single spike and incorrectly sorted by using the conventional template-matching method. (a) - (c) Signal generated by each neuron. (d) Recorded signal without noise (sum of signals generated from three neurons). (e) Recorded signal with noise. Only this signal could be obtained by extracellular voltage recording.

1.4.3 Issues in spike detection and sorting

Several issues in spike detection and sorting have been targets of interest for a long time. Here we discuss the issues raised by Lewicki (1998).

First, the shapes of spikes can be nonstationary. This makes it impossible to classify spikes by their shapes. The long-term changes caused by the drifts of electrodes and the short-term changes caused by burst firing are often problematic.

A second problem is intractable noise. For example, nonstationary background noise makes it difficult to determine the threshold for detect spikes. In addition, artifact noises with spike-like shapes often cause detection errors.

Last, if more than two spikes overlap, it is difficult to detect and sort spikes by their shapes. The typical methods used for spike detection and sorting have trouble handling overlapping spikes: that is, they cannot properly classify more than two spikes that occur simultaneously and merge into a complex waveform (Lewicki et al., 1998; Brown et al., 2004). An example of an overlap is shown in Figure 1.19. Many spikes are overlapped when the spikes are distributed densely and synchronously. Dense and synchronous spiking has been a frequent phenomenon found in bursting over a neuronal network (Wagenaar et al., 2006), responses evoked by electrical stimuli (Suzuki et al., 2007), and so on. The errors in spike detection and sorting caused by overlaps are non-negligible because they can produce invalid analysis results, such as spurious correlations between pairs of neurons, as has been shown by Bar-Gad et al. (2001). This thesis focuses on this issue.

1.4.4 Previous studies dealing with spike overlaps

Various methods have been proposed for dealing with the problem of overlaps in spike sorting. A method that use independent component analysis (Takahashi et al., 2003a, 2003b; Takahashi and Sakurai, 2003) and another that use an optimal filter (Franke et al., 2010) have been shown to perform fairly well, even for signals containing overlaps. However, these methods can be applied only to signals recorded with a multitrode, which has multichannel electrodes at a single recording point. Although these electrodes can be used to obtain spatial information about recorded spikes, they are unsuitable when interfaces are needed with as many neurons as possible from a large area because the number of recording points is limited to the number of measurement resources (i.e., amplifiers, filters, and analog/digital converters). For example, Utah electrodes for recording *in vivo* (Campbell et al., 1991; Donoghue, 2002; Lebedev and Nicolelis, 2006) and multi-electrode arrays (MEAs) for recording *in vitro* (Bakkum et al., 2008), both of which are sparse electrode arrays, have been used in many applications. For such electrodes, a method that uses the k-d tree data structure (Lewicki, 1994) is available. However, implementing such a method requires the preparation of a

limited number of overlapping waveform patterns before real-time template matching, and thus, patterns detected without matching prepared patterns cannot be treated. An off-line method based on a hidden Markov model (Herbst et al., 2008) also has a limitation of a number of overlapping patterns.

Methods for decomposing electromyographic signals (Stashuk 2001, McGill 2002, Ge et al., 2010) can be applied to neural spikes. These methods can process the data recorded with a single electrode, and they have been shown to be robust against overlaps. The method by Ge et al. has the particular advantage of placing no restriction on the number of spikes in each overlap. However, this method also has limitations. First, it does not have the capability of the fast and sequential estimation needed for real-time use, and none have achieved the fast and sequential detection and classification of arbitrarily overlapping spikes recorded with arbitrary types of electrodes. Second, the regularity of the interspike interval is assumed in the method. However, this is an unrealistic assumption for most neurons in the brain.

1.5 Scope and contributions

As shown in Section 1.4, spike detection and sorting algorithms are generally classified into two types, the ones that estimate spike templates and spike timings from the recorded signal offline (e.g., spike detection by threshold and applying clustering algorithms) and the ones that detect spikes in real-time with given spike templates (e.g., spike detection by threshold and classifying detected spike shapes into the prepared spike template with the least mean square error). The previous spike-sorting methods of both types that deal with spike overlaps have undesirable limitations on spike patterns, the choice of electrodes, or the allowed number of spikes in an overlap. We focus on this problem and propose two methods based on Bayesian statistics in the present thesis. One is for off-line use and can be used to estimate unknown spike templates and spike timings simultaneously from the recorded signal and the other is for real-time spike detection and sorting by using given spike templates. Both methods can detect and sort spikes robustly in complex overlaps of arbitrary numbers of spikes without restrictions of the choice of electrodes and spike patterns. The aim of these methods is to help in the analysis of highly synchronized and overlapping neural activities recorded in extracellular voltage recording, which has been unmanageable in neuroscience research and in applications in neural engineering, such as the brain-machine interface.

1.6 Organization

The present thesis deals with the detection and sorting of complexly overlapped neural spikes

recorded by extracellular voltage recording. For this purpose, this thesis proposes two methods. In Chapter 2, a method for the fast and sequential detection of arbitrarily overlapping spikes in real-time processing is proposed and the performance is assessed with simulated and real neural signals. In Chapter 3, a method for the simultaneous estimation of spike templates and timings of highly overlapped spikes is proposed and the performance is assessed with simulated and real neural signals. In Chapter 4, we apply the two methods to various signals in combination in order to solve the weak points of the two methods complementarily. Chapter 5 summarizes the results and contributions of the thesis and discusses future research directions.

In the present thesis, all processing was programmed in C++ and performed on a standard laptop computer with no special parallel computing.

Chapter 2
Real-time Detection and Sorting of Overlapped Neural Spikes

2.1 Overview

In this chapter, we present a method for fast and sequential detection of arbitrarily overlapping spikes, which are inevitable in the real-time template-matching phase, by using a computationally efficient model-based sequential Bayesian inference algorithm. In our approach, multi-unit recording and spike-train generation are modeled and probabilities of possible spike trains are estimated based on the models.

As shown in Chapter 1, various shapes of spikes are recorded in the extracellular recording, which are influenced by various complex conditions such as the structure and the type of the neuron, the position of the neuron and the electrode, and inhomogenous properties of the extracellular medium. It is difficult to derive the general function which represents all possible spike shapes in the condition that we cannot know such informations preliminarily, which is usual in many applications. Therefore, to enable our method to be used in general conditions, we applied no restrictions on spike shapes and we assume that the waveform of length M which repeatedly appears in the recorded signal is neural spikes. That is, we ignored conditions which can change spike shapes in a signal (e.g. bursting neurons, moving of neurons and electrodes). It is the same assumption with previous researches shown in Chapter 1. However, unlike most previous approaches, spike shapes in the recorded signal can be superposed and summed in our models, so arbitrary overlaps are considered in the estimation. Furthermore, we take the same approach to the spike-train generation which corresponds to the generation of action potentials. We assumed the random firing processes of neurons which are independent of each other and affected only by the refractory period which is the general property of neurons. It becomes a kind of inhomogenous Poisson process (Dayan et al., 2005). By using these models and sequential Bayesian inference, we evaluate the probability of each possible spike train and obtain the spike train with the highest probability. Since the number of spike trains for which probabilities are to be evaluated in the inference is too large to calculate, we censor the candidates with low probability to limit the number of candidates to be evaluated at the next

sampling time. Furthermore, the use of the "look-ahead probability," the probability based on considering the data for a few sampling times ahead, leads to more efficient calculation due to the faster elimination of candidates.

We assessed the performance of our method with simulated neural signals and a real neural signal recorded from primary rat cortical neurons cultured on the MEA. In the experiment with simulated signals, we assessed the capability of the real-time processing and the validity of the estimation by our method by comparing its computational time and error rates with those of a conventional real-time template-matching method for various conditions. In the experiment with the real neural signal, in which we could not know the correct spike train, we showed that our method could appropriately decompose complexly overlapped spikes by reconstructing the signal from estimated spike trains and templates.

2.2 Methods

2.2.1 Models of spike-train generation and multi-unit recording

We derived two probabilistic models for spike-train generation and multi-unit extracellular voltage recording. These models were constructed to be able to generate overlapping spikes.

First, the generation of spikes from the neurons recorded at each sampling time is modeled as a multinomial distribution with a refractory period. Supposing the recorded signal contained *N* spike waveforms recorded from *N* neurons, we defined x_t as a spike train variable that takes $n\,(n = 1,2,\dots,N)$ when neuron n starts to generate spikes at sampling time t and 0 otherwise. At every sampling time, neurons that had generated a spike in the previous *M* samples are assumed to be in a refractory period, and the probability for each neuron to generate a spike is assumed to be zero. The set of such neurons can be written as $\mathrm{S_{ref}} = \{n | \exists \tau \in \mathbb{N}\ \mathrm{s.t.}\ 1 \le \tau \le M, x_{t-\tau} = n\}$. The neurons that had not generated a spike in the previous *M* samples are assumed to be able to generate a spike, and the probability for each neuron to generate a spike at each sampling time is assumed to be p_t. The set of such neurons can be written as $\mathrm{S_{fire}} = \{n | \forall \tau \in \mathbb{N}\ \mathrm{s.t.}\ 1 \le \tau \le M, x_{t-\tau} \neq n\}$. Under these assumptions, the probability of non-spiking is $1 - N_f p_t$ (N_f is the number of elements in $\mathrm{S_{fire}}$) and the probabilistic spike-train generation model can be written as

$$\mathrm{p}(x_t = n | x_{t-M}, \dots, x_{t-1}) = \begin{cases} 1 - N_f p_f, & \text{if } n = 0 \\ p_f, & \text{if } n \in \mathrm{S_{fire}} \\ 0, & \text{if } n \in \mathrm{S_{ref}} \end{cases} \quad (2.1)$$

.

Second, recorded signal y_t is modeled by using the spike train $\{x_{t-M}, \dots, x_t\}$, the spike template

for the neuron n $\boldsymbol{\mu}_n = (\mu_n[0], \ldots \mu_n[M])$ and additive Gaussian noise with standard deviation σ. The probabilistic recording model can be written as

$$\mathrm{p}(y_t|x_{t-M}, \ldots, x_t) = \frac{1}{\sqrt{2\pi\sigma^2}} \exp\left(\frac{\left(y_t - \sum_{\tau=0}^{M} \mu_{x_{t-\tau}}[\tau]\right)^2}{2\sigma^2}\right). \tag{2.2}$$

2.2.2 Sequential Bayesian inference

Probability $\mathrm{p}(x_{t-M}|y_1, \ldots, y_t)$, the assumed estimated probability of spike existence, is calculated at every sampling time on the basis of sequential Bayesian inference. First, the conditional joint distributions of $\{x_{t-M}, \ldots, x_t\}$ and y_t given $y_1, \ldots, y_{t-1}$ are derived from $\mathrm{p}(x_{t-M}, \ldots, x_{t-1}|y_1, \ldots, y_{t-1})$ (probabilities of spike trains obtained at previous sampling time) and the probabilistic models given above.

$$\begin{aligned}&\mathrm{p}(x_{t-M}, \ldots, x_t, y_t|y_1, \ldots, y_{t-1}) \\ &\quad = \mathrm{p}(y_t|x_{t-M}, \ldots, x_t)\mathrm{p}(x_t|x_{t-M}, \ldots, x_{t-1})\mathrm{p}(x_{t-M}, \ldots, x_{t-1}|y_1, \ldots, y_{t-1})\end{aligned} \tag{2.3}$$

The marginal likelihood of y_t given previous data $y_1, \ldots, y_{t-1}$ is calculated, and the posterior probabilities of spike trains $\mathrm{p}(x_{t-M}, \ldots, x_t|y_1, \ldots, y_t)$ are obtained by normalizing $\mathrm{p}(x_{t-M}, \ldots, x_t, y_t|y_1, \ldots, y_{t-1})$ by the likelihood.

$$\mathrm{p}(y_t|y_1, \ldots, y_{t-1}) = \sum_{x_{t-M}, \ldots, x_t} \mathrm{p}(x_{t-M}, \ldots, x_t, y_t|y_1, \ldots, y_{t-1}) \tag{2.4}$$

$$\mathrm{p}(x_{t-M}, \ldots, x_t|y_1, \ldots, y_t) = \frac{\mathrm{p}(x_{t-M}, \ldots, x_t, y_t|y_1, \ldots, y_{t-1})}{\mathrm{p}(y_t|y_1, \ldots, y_{t-1})} \tag{2.5}$$

The estimated probabilities of spike existence are obtained by marginalizing out $\{x_{t-M+1}, \ldots, x_t\}$.

$$\mathrm{p}(x_{t-M}|y_1, \ldots, y_t) = \sum_{x_{t-M+1}, \ldots, x_t} \mathrm{p}(x_{t-M}, \ldots, x_t|y_1, \ldots, y_t) \tag{2.6}$$

Finally, $\mathrm{p}(x_{t-M+1}, \ldots, x_t|y_1, \ldots, y_t)$ is obtained by marginalizing out x_{t-M} (the oldest sample in spike trains). It is carried over to the next sampling time and used as $\mathrm{p}(x_{t-M}, \ldots, x_{t-1}|y_1, \ldots, y_{t-1})$ in equation (2.3).

$$\mathrm{p}(x_{t-M+1}, \ldots, x_t|y_1, \ldots, y_t) = \sum_{x_{t-M}} \mathrm{p}(x_{t-M}, \ldots, x_t|y_1, \ldots, y_t) \tag{2.7}$$

2.2.3 Approximation of probabilities to reduce computational cost

Computational cost is reduced by eliminating the instances of $\{x_{t-M+1}, \ldots, x_t\}$ that have a probability lower than threshold p_{th} at each sampling time and calculating the probabilities of only the remaining instances. This process can be interpreted as the approximation of low probabilities to zero. With this approximation, we avoid the evaluation of $\mathrm{p}(x_{t-M+1}, \ldots, x_t|y_1, \ldots, y_t)$ for all

instances, which is computationally expensive and prevents real-time application.

Computational cost is further reduced by the use of the look-ahead probability to eliminate candidates. In the estimation procedure, the waveform peaks usually correspond to the biggest difference between spike templates including the zero-filled one corresponding to $n = 0$ (no spikes). This difference leads to an imbalance in probabilities between candidates and triggers the elimination of many candidates. Therefore, the look-ahead evaluation of spike template peaks reduces the number of candidates. The L last recorded data samples are buffered and "look-ahead probability" $\mathrm{p}(x_{t-M+1}, \dots, x_t | y_1, \dots, y_t, y_{t+L})$ is calculated:

$$\mathrm{p}(x_{t-M+1}, \dots, x_t, y_{t+L} | y_1, \dots, y_t) = \mathrm{p}(y_{t+L} | x_{t-M+1}, \dots, x_t) \mathrm{p}(x_{t-M+1}, \dots, x_t | y_1, \dots, y_t) \quad (2.8)$$

$$\mathrm{p}(y_{t+L} | y_1, \dots, y_t) = \sum_{x_{t-M+1}, \dots, x_t} \mathrm{p}(x_{t-M+1}, \dots, x_t, y_{t+L} | y_1, \dots, y_t) \quad (2.9)$$

$$\mathrm{p}(x_{t-M+1}, \dots, x_t | y_1, \dots, y_t, y_{t+L}) = \frac{\mathrm{p}(x_{t-M+1}, \dots, x_t, y_{t+L} | y_1, \dots, y_t)}{\mathrm{p}(y_{t+L} | y_1, \dots, y_t)} \quad (2.10)$$

where

$$\mathrm{p}(y_{t+L} | x_{t-M+1}, \dots, x_t) = \frac{1}{\sqrt{2\pi\sigma^2}} \exp\left(\frac{\left(y_{t+L} - \sum_{\tau=0}^{M-L} \mu_{x_{t-\tau}}[\tau + L]\right)^2}{2\sigma^2} \right). \quad (2.11)$$

The instances $\{x_{t-M+1}, \dots, x_t\}$ that have a probability lower than p_{th} are eliminated at each sampling time.

In equation (2.11), the effects of the spikes generated at $t+1, t+2, \dots, t+L-1$ are ignored in the evaluation of the probability of y_{t+L}. However, this approximation does not cause inappropriate candidate eliminations because the amplitude of the waveform is low enough immediately after spike generation.

The value of L should be equal to or lower than the position of the highest peaks to achieve the purpose of look-ahead elimination. That is, if the peaks in the spike templates are at $\mu_n[2]$, L should be set to 2 or lower. If L is set to a larger value, the look-ahead probability will be evaluated ignoring the most important features in the spike waveforms and thus cause inappropriate candidate eliminations.

2.2.4 Algorithms

Making use of these approximations, we derived an updating algorithm that is processed at every sampling time. At sampling time t, a new datum y_{t+L} is recorded, and equation (2.3) is evaluated for the instances by using buffered datum y_t, as shown below (the variables and functions used in the pseudo codes in this section are defined in Table 2.1).

Table 2.1: Definitions of variables and functions used in pseudo codes in this section.

Name	Definition
X	2D array containing instances of spike trains considered at current sampling time ($x_{t-M:t}$).
Xprev	2D array containing instances of spike trains estimated at previous sampling time ($\{x_{t-M}, \ldots, x_{t-1}\}$, $\{x_{t-M+1}, \ldots, x_t\}$).
P	1D array containing probabilities of elements in *X* ($\mathrm{p}(x_{t-M}, \ldots, x_t, y_t | y_1, \ldots, y_{t-1})$, $\mathrm{p}(x_{t-M}, \ldots, x_t | y_1, \ldots, y_t)$).
Pprev	1D array containing probabilities of elements in *Xprev* ($\mathrm{p}(x_{t-M}, \ldots, x_{t-1} | y_1, \ldots, y_{t-1})$, $\mathrm{p}(x_{t-M+1}, \ldots, x_t | y_1, \ldots, y_t)$).
Pahead	1D array containing look-ahead probabilities of elements in *Xprev.*
C	Number of elements in *X*.
Cprev	Number of elements in *Xprev.*
Likelihood	Likelihood of y_t ($\mathrm{p}(y_t | y_1, \ldots, y_{t-1})$).
Result	1D array containing estimated probabilities of spike existence ($\mathrm{p}(x_{t-M} | y_1, \ldots, y_t)$).
Tmp	Temporary variable.
GenModel(spike_train)	Function that returns probability of spike train calculated with model of spike-train generation ($\mathrm{p}(x_t | x_{t-M}, \ldots, x_{t-1})$).
RecModel(data, spike_train)	Function that returns probability of data for given spike train calculated with recording model ($\mathrm{p}(y_t | x_{t-M}, \ldots, x_t)$).
LookaheadModel(data, spike_train)	Function that returns look-ahead probability of data for given spike train calculated with the model of look-ahead probability ($\mathrm{p}(y_{t+L} | x_{t-M+1}, \ldots, x_t)$).

Algorithm 1

$C \Leftarrow 0$
for $i = 0 : Cprev - 1$ **do**
  for $n = 0 : N$ **do**
    $X[C][0] \Leftarrow n$
    for $j = 1 : M$ **do**
      $X[C][j] \Leftarrow Xprev[i][j-1]$
    end for
    if $GenModel(X[C]) > 0$ **then**
      $P[C] \Leftarrow RecModel(y_t, X[C]) * GenModel(X[C]) * Pprev[i]$
      $C \Leftarrow C + 1$
    end if
  end for
end for

Next, equations (2.4) and (2.5) are evaluated.

Algorithm 2

$likelihood \Leftarrow \sum_{i=1}^{C} P[i]$
for $i = 1 : C$ **do**
  $P[i] \Leftarrow \frac{P[i]}{likelihood}$
end for

The estimated result is obtained by evaluation of equation (2.6).

Algorithm 3

for $n = 0 : N$ **do**
  $result[n] \Leftarrow 0$
  for all i such that $X[i][M] = n$ **do**
    $result[n] \Leftarrow result[n] + P[i]$
  end for
end for

Equation (2.7) is then evaluated to obtain the information to be used at the next sampling

Algorithm 4

$Cprev \Leftarrow 0$
for $i = 0 : C - 1$ **do**
  $FLAG \Leftarrow 1$
  for $j = 0 : Cprev - 1$ **do**
    if $0 \leq \forall k \leq M - 1, X[i][k] = Xprev[j][k]$ **then**
      $Pprev[j] \Leftarrow Pprev[j] + P[i]$
      $FLAG = 0$
    end if
  end for
  if $FLAG \neq 0$ **then**
    for $k = 0 : M - 1$ **do**
      $Xprev[Cprev][k] \Leftarrow X[i][k]$
    end for
    $Pprev[Cprev] \Leftarrow P[i]$
    $Cprev \Leftarrow Cprev + 1$
  end if
end for

Spike trains with low probabilities are eliminated.

Algorithm 5

for all i such that $Pprev[i] < p_{th}$ **do**
  delete $Xprev[i]$
  delete $Pprev[i]$
  $Cprev \Leftarrow Cprev - 1$
end for

If look-ahead elimination is enabled (L>0), further elimination of spike trains by look-ahead elimination is performed at the end of the processing at each sampling time.

Algorithm 6

if $L > 0$ then
  $tmp \Leftarrow 0$
  for $i = 0 : Cprev$ do
    $Pahead[i] \Leftarrow LookaheadModel(y_{t+L}, Xprev[i]) * Pprev[i]$
    $tmp \Leftarrow tmp + Pahead[i]$
  end for
  for all i such that $Pahead[i]/tmp < p_{th}$ do
    delete $Xprev[i]$
    delete $Pprev[i]$
    $Cprev \Leftarrow Cprev - 1$
  end for
end if

Xprev and *Pprev* are carried over to the next sampling time, and algorithm 1 is processed again with a newly recorded datum.

2.3 Experiments

2.3.1 Assessment of computational efficiency and error rates with simulated signals

To assess the computational efficiency and estimation accuracy of our method, we compared its computational time, spike detection error rate with those of a conventional real-time spike detection method. We used signals simulated under various firing rates (corresponding to overlap frequency) and noise levels. As the conventional real-time spike detection method, we used a method that detects spikes with a threshold that is four times the standard deviation of the noise level (4σ) and that classifies spike waveforms into spike templates on the basis of minimum distance.

The assessment was performed with sixty seconds of simulated signals containing the five spike shapes shown in Figure 2.2 with additive white Gaussian noise. The five spikes shapes are manually created mimicking different amplitudes (around +/- 100μV) and shapes (mono-phasic and bi-phasic pulses of the length 1.5 ms) of spikes found in actual recordings and simulations of cortical neurons as shown in Figure 1.9, 1.10.

The standard deviation of noise (σ) was 15 or 30 μV, and the sampling rate (f_s) was 10 kHz. We assumed that the generation of spikes from each neuron followed an independent Poisson process and set the expected number of spikes for one neuron (firing rate; f_{fire}) in 1 s to 1, 5, 10, 50, or 100. In this experiment, 1, 5, and 10 Hz were used as relatively low firing rates, and 50 and 100 Hz were chosen as relatively high firing rates. Signals simulated under the various conditions are shown in

Figure 2.3.

Obviously, the higher firing rates were expected to generate more overlapping spikes, so the change in performance due to overlaps could be evaluated in this experiment. The content rate of overlapped spikes can be theoretically estimated for various firing rates. First, the probability of non-overlapping spike generation is calculated as the probability of no further spike generation in M samples after a spike has been generated. The probability of spike generation at a sampling time is $\frac{f_{\text{fire}}}{f_s}$ (ignoring the effect of the refractory period) and the probability of no further spike generation at a sampling time is $1-n\frac{f_{\text{fire}}}{f_s}$ if there are n neurons that can fire. In the M samples after a neuron has fired, there are $N-1$ neurons that can generate spikes. Consequently, the probability of non-overlapping spike generation is

$$\mathrm{P}(\text{no overlap}) = \left(1-(N-1)\frac{f_{\text{fire}}}{f_s}\right)^M. \tag{2.12}$$

Overlaps occur when spikes are generated in *M* samples after previous spikes. And when no spikes are generated in *M* samples, a series of overlapping is terminated. The probability of n neurons generating more than one spike in *M* samples is $1-\left(1-n\frac{f_{\text{fire}}}{f_s}\right)^M$. Thus, the probability of generating overlaps containing λ spikes ($1 \leq \lambda \leq N$) after a spike has occurred is

$$\mathrm{P}(\lambda \text{ spikes overlapped}) = \left(1-(N-\lambda)\frac{f_{\text{fire}}}{f_s}\right)^M \prod_{n=N-\lambda+1}^{N-1}\left(1-\left(1-n\frac{f_{\text{fire}}}{f_s}\right)^M\right) \tag{2.13}$$

This equation corresponds to equation (2.12) for $\lambda = 1$. The number of spikes in the overlaps of λ spikes is

$$\lambda\mathrm{P}(\lambda \text{ spikes overlapped}) = \lambda\left(1-(N-\lambda)\frac{f_{\text{fire}}}{f_s}\right)^M \prod_{n=N-\lambda+1}^{N-1}\left(1-\left(1-n\frac{f_{\text{fire}}}{f_s}\right)^M\right) \tag{2.14}$$

Table 2.2. Estimated content rates of overlapped spikes in simulation. Each column corresponds to number of spikes in one sequence of overlaps, and each row corresponds to firing rate used in simulation.

Sampling rate	non-overlap	2 spikes	3 spikes	4 spikes	5 spikes
1Hz	99%	1.1 %	6.9×10^{-3} %	2.6×10^{-6} %	4.6×10^{-8} %
5Hz	95%	5.3 %	0.17 %	3.1×10^{-3} %	2.7×10^{-5} %
10Hz	90%	9.8 %	0.62 %	2.3×10^{-2} %	4.1×10^{-4} %
50Hz	58%	31 %	9.3 %	1.8 %	0.16 %
100Hz	35%	35 %	21 %	8.0 %	1.6 %

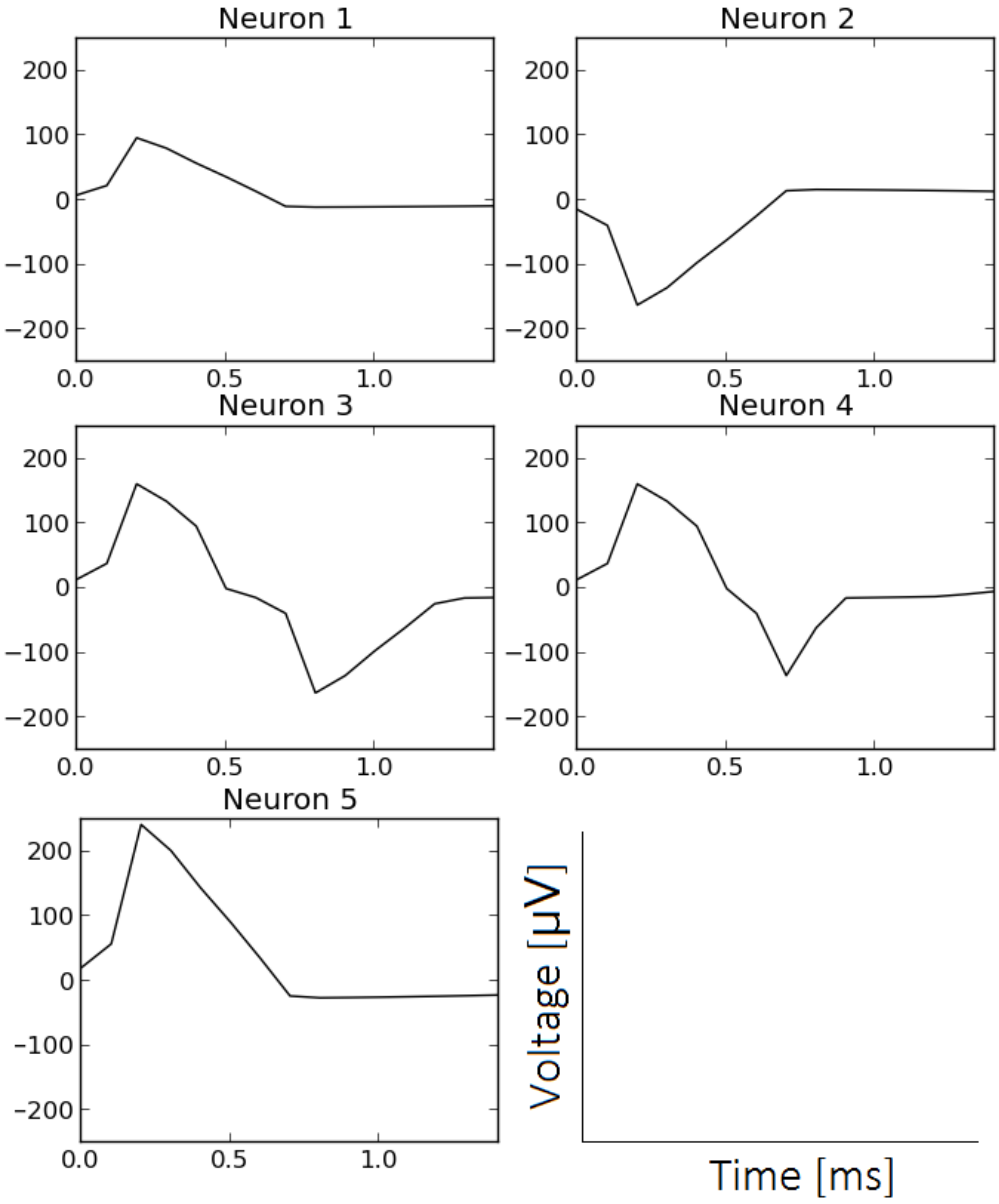

Figure 2.2. Five spike shapes used in assessment. Each template was assumed to correspond to spikes from one neuron. Mono-phasic waveforms (Neurons 1, 2, 3) and bi-phasic waveforms (Neurons 4, 5) were prepared.

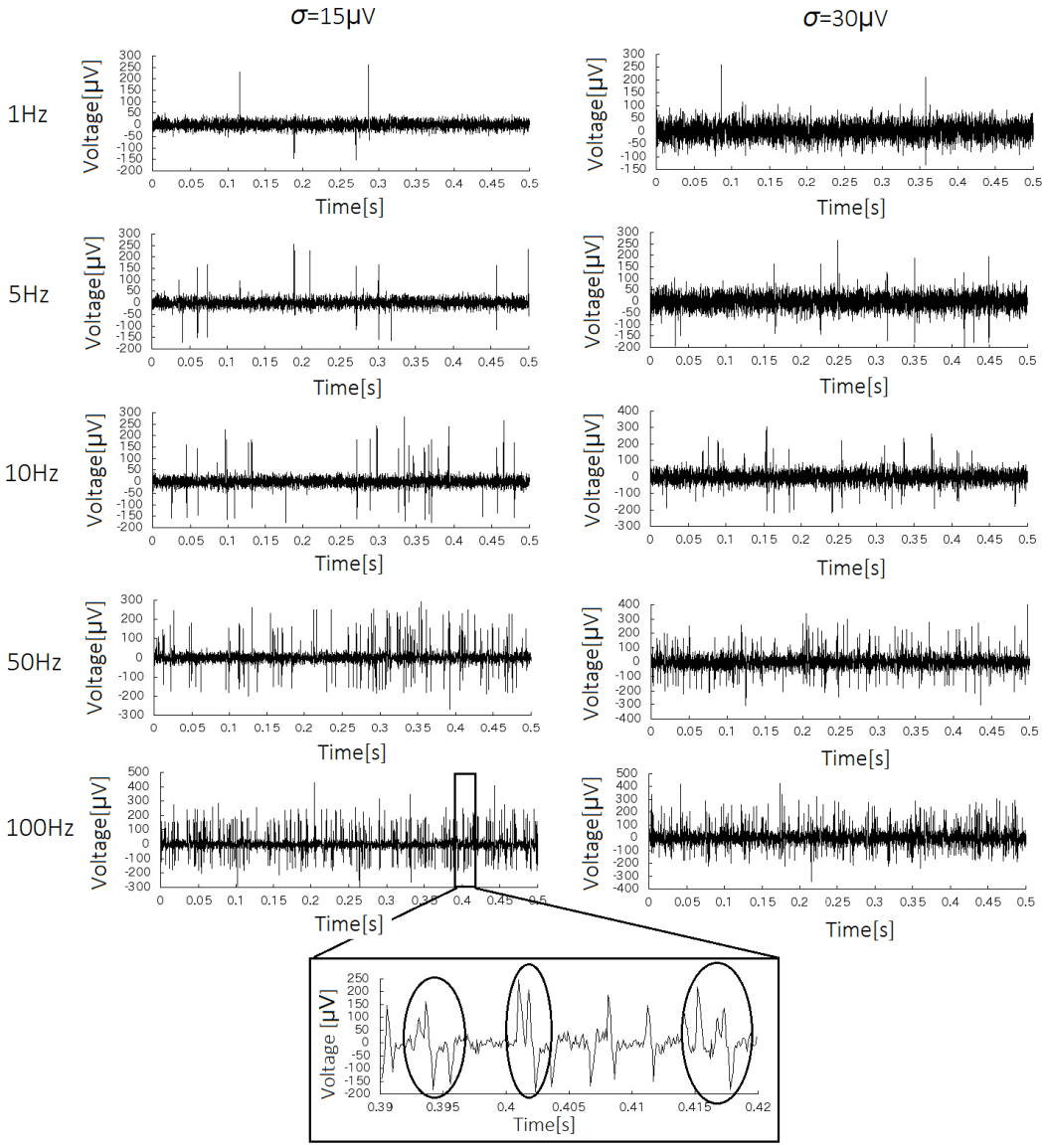

Figure 2.3. Parts of signals simulated under various conditions. Firing rate was 1, 5, 10, 50, or 100 Hz. Overlap frequency increased with firing rate. Standard deviation of noise (σ) was set to 15 or 30 μV.

The content rate of spikes in the overlaps of λ spikes can be estimated by normalizing equation (2.14) by the total number of spikes. The content rates of overlapped spikes for various firing rates can be estimated by using equation (2.14). The estimated rates are shown in Table 2.2, and the ones measured from the simulated signals are shown in Table 2.3.

We applied the conventional method and our method with look-ahead elimination ($L = 2$) and without it ($L = 0$) to simulated signals and counted the number of false positives (FPs), false negatives (FNs) and true positives (TPs) occurring in the spike detection and calculated the positive error rate (PER), the negative error rate (NER), and the total error rate (TER).

$$\mathrm{PER} = 100\left(\frac{\mathrm{FP}}{\mathrm{TP}+\mathrm{FN}}\right) \tag{2.15}$$

$$\mathrm{NER} = 100\left(\frac{\mathrm{FN}}{\mathrm{TP}+\mathrm{FN}}\right) \tag{2.16}$$

$$\mathrm{TER} = 100\left(\frac{\mathrm{FP}+\mathrm{FN}}{\mathrm{TP}+\mathrm{FN}}\right) \tag{2.17}$$

We recorded the computational time for processing the data at each sampling time. Our method was applied with $p_f = 1\times10^{-2}, p_{\mathrm{th}} = 1\times10^{-6}, M = 1.5\mathrm{ms}$, and spikes were detected when $\mathrm{p}(x_{t-M} = n|y_1,\dots,y_t)$ exceeded 0.5 for $1 \le n \le N$. The setting of the threshold was heuristically chosen for the best performance and was not changed over the course of the experiment.

Additionally, we evaluated the effect of the setting of p_f by applying our method with look-ahead elimination to signals simulated for various firing rates (σ=15μV) and comparing the error rates for $p_f = 1\times10^{-2}, 1\times10^{-3}, 1\times10^{-4}$.

Table 2.3. Content rates of overlapped spikes measured from simulated signals. Each column corresponds to number of spikes in one sequence of overlaps, and each row corresponds to firing rate used in simulation.

Sampling rate	non-overlap	2 spikes	3 spikes	4 spikes	5 spikes
1Hz	98%	2.3 %	0 %	0 %	0 %
5Hz	93%	6.4 %	0.42 %	0 %	0 %
10Hz	88%	11 %	0.84 %	0.14 %	0 %
50Hz	55%	31 %	10.4 %	2.5 %	0.92 %
100Hz	31%	33 %	20 %	9.4 %	7.0 %

2.3.2 Assessments with the real neural signal

With the real neural signal, we assessed whether our method could appropriately decompose overlapped spikes by reconstructing the signal from estimated spike trains and templates. We used a signal recorded from neurons cultured on the MEA (the signal was shown in Figure 2.4). Details of cell culture and recording methods are written in Appendix A.

Intrinsically bursting neurons, which is outside the scope of our methods, are contained in cortical neurons. However, Baltz et al.(2011) showed that they were found only in cultures younger than 3week in vitro and activities of those neurons were not recorded after that. Therefore, it is assumed that spikes from bursting neurons are not recorded from cultured neurons used in the experiment.

In the pre-processing phase, we detected and collected spike waveforms exceeding the threshold (4σ) from the recorded data. We then obtained spike templates by clustering these spike waveforms by using density-based spatial clustering of applications with noise (DBSCAN), a clustering method robust to outliers (Ester et al., 1996). By using these templates, we applied the conventional template-matching method and our method with look-ahead elimination to a part of the signal (shown in Figure 4) and reconstructed the signal from the estimated spike trains and spike templates by using the recording model (equation (2.2)). The parameter settings for our method were $p_f = 1 \times 10^{-5}, p_{\mathrm{th}} = 1 \times 10^{-10}, M = 2.0\mathrm{ms}, L = 2$, and spikes were detected when $\mathrm{p}(x_{t-M} = n | y_1, \ldots, y_t)$ exceeded 0.5 for $1 \leq n \leq N$.

In all the experiments, the standard deviation of noise σ was estimated by the equation below, in accordance with previous studies (Quian Quiroga et al., 2004; Kim and McNames, 2007).

$$\sigma = \mathrm{median}\left\{\frac{|y_t|}{0.6745}\right\} \tag{2.18}$$

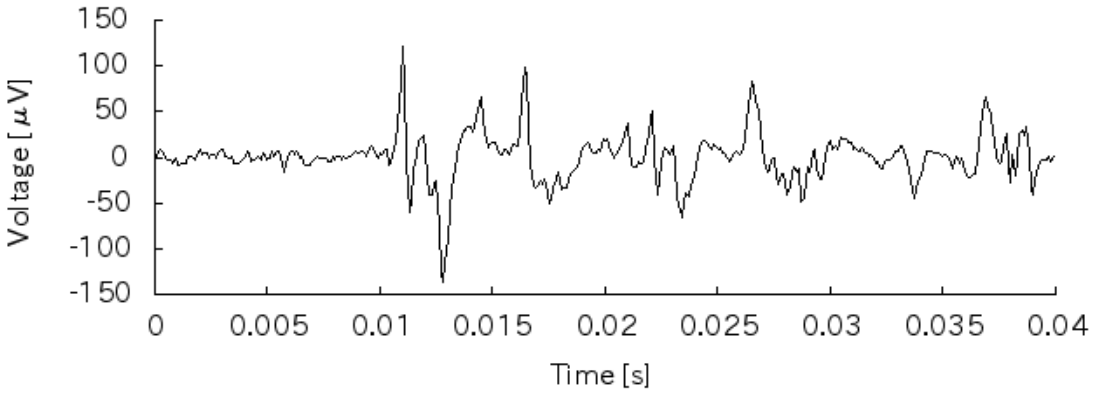

Figure 2.4. Part of signal recorded from primary cortical neurons cultured on MEA. Many complex spike waveforms were expected to be produced by spike overlaps.

2.4 Results

2.4.1 Computational efficiency and error rates for simulated signals

Figure 2.5 (a) shows the positive error rate (PER) of the estimation for signals simulated under various conditions. Under all conditions, the error rate of our method, both with and without look-ahead elimination, was lower than that of the conventional method. The difference was significant especially under the high noise condition (σ=30 μV), except for the high error rate of all methods for the 1 Hz firing rate. Under the low noise condition (σ=15 μV), the higher firing rates led to higher error rates and a big difference in results between the conventional method and our method, with and without look-ahead elimination. There was little difference in the results of our method between with and without look-ahead elimination.

Figure 2.5 (b) shows the negative error rate (NER) of the estimation for signals simulated under various conditions. The tendencies were basically the same as for the PER; however, the differences in the error rate between the conventional method and our method, with and without look-ahead elimination, were higher than those for the PER; and the error rate for rate = 1Hz and σ = 30 μV was low.

Figure 2.5 (c) shows the total error rate (TER) of the estimation for signals simulated under various conditions. The error rates of our method with and without look-ahead elimination were almost the same and were lower than those of the conventional method for all conditions, reflecting the PER and NER results. Moreover, the differences increased with the firing rate and noise level.

For all these metrics under the various conditions, our method, with and without look-ahead elimination, performed better than the conventional method. It performed especially better for the high firing rates, which produced many overlaps (see Table 2.2 and Table 2.3). These results show the robustness of our method for treating overlaps. They also show that the conventional method is sensitive to high noise whereas the performance of our method is negligibly impaired by high noise and that the look-ahead elimination did not impair the performance of our method.

Figure 2.5 (d) shows the computational time of the estimation from the signal simulated in various conditions by the three methods. In contrast to error rates, the computational time of our method, with and without look-ahead, was higher than the conventional method in all conditions and the differences were bigger under high firing rates and higher noise. However, the worst time (our method without look-ahead for the 100Hz firing rate and σ=30μV) was shorter than the length of the data (60s). Besides, we showed that the look-ahead strategy reduced the computational time of our method to less than half the time of our method without look-ahead.

We evaluated the delays of our method with look-ahead elimination in a real-time application on

the basis of the computational time at each sampling point or each short-time window (Figure 2.6). For a firing rate of 100 Hz and a σ of 15 μV (Figure 2.6 (a)) and for a firing rate of 50 Hz and a σ of 30 μV (Figure 2.6 (b)), real-time processing without delay (meaning that all the processing at a sampling point completes within the sampling interval) is possible because the computational time was less than the sampling interval at all sampling points. On the other hand, for a firing rate of 100 Hz and a σ of 30μV (Figure 2.6 (c)), real-time processing without delay was impossible because there were some sampling points where the computational time was longer than the sampling interval. However, the computational time for 10ms bins (each bin contained 100 sampling points) was less than 10ms for all bins, meaning that real-time processing with < 10 ms delay is possible.

Figure 2.7 shows the error rates for our method with different settings of p_i for signals simulated under various conditions. All the settings of p_i resulted in comparable performance for the lower firing rates. In contrast, for the higher firing rates, a higher value of p_i resulted in better performance.

2.4.2 Assessments with the real neural signal

Figure 2.8 shows clusters and spike templates created by DBSCAN from spike waveforms in the signal recorded from cultured neurons. Eight different spike templates were obtained.

Figure 2.9 shows spike trains estimated from the signal shown in Figure 5 by using the conventional method and our method with look-ahead elimination and Figure 2.10 shows the estimated spike waveforms and the signal reconstructed from the estimated spike trains and spike templates. The number of spikes was estimated to be 12 by the conventional method (Figures 2.9 (a) and 2.10 (b)), and the accuracy of reconstruction was low (Figure 2.10 (c)). In contrast, the number of spikes was estimated to be 26 by our method, and closely generated spikes were separately detected (Figure 2.9 (b) and Figure 2.10 (d)). Moreover, the signal was correctly reconstructed from the estimated spike trains (Figure 2.10 (e)). These results mean that our method can appropriately decompose overlapped spikes, which could not be done by the conventional method. This enabled the detection of 14 spikes miss

2.5 Discussion

The results of our assessment showed that the performance of the conventional real-time template-matching method we used was seriously impaired by frequent overlaps caused by relatively high firing rates. These overlaps mainly caused negative errors because the NER values (Figure 2.5 (b)) under the lower noise conditions were almost the same as the value of the estimated content rate of spike overlaps shown in Table 1. Such negative errors were found in the assessment with the real

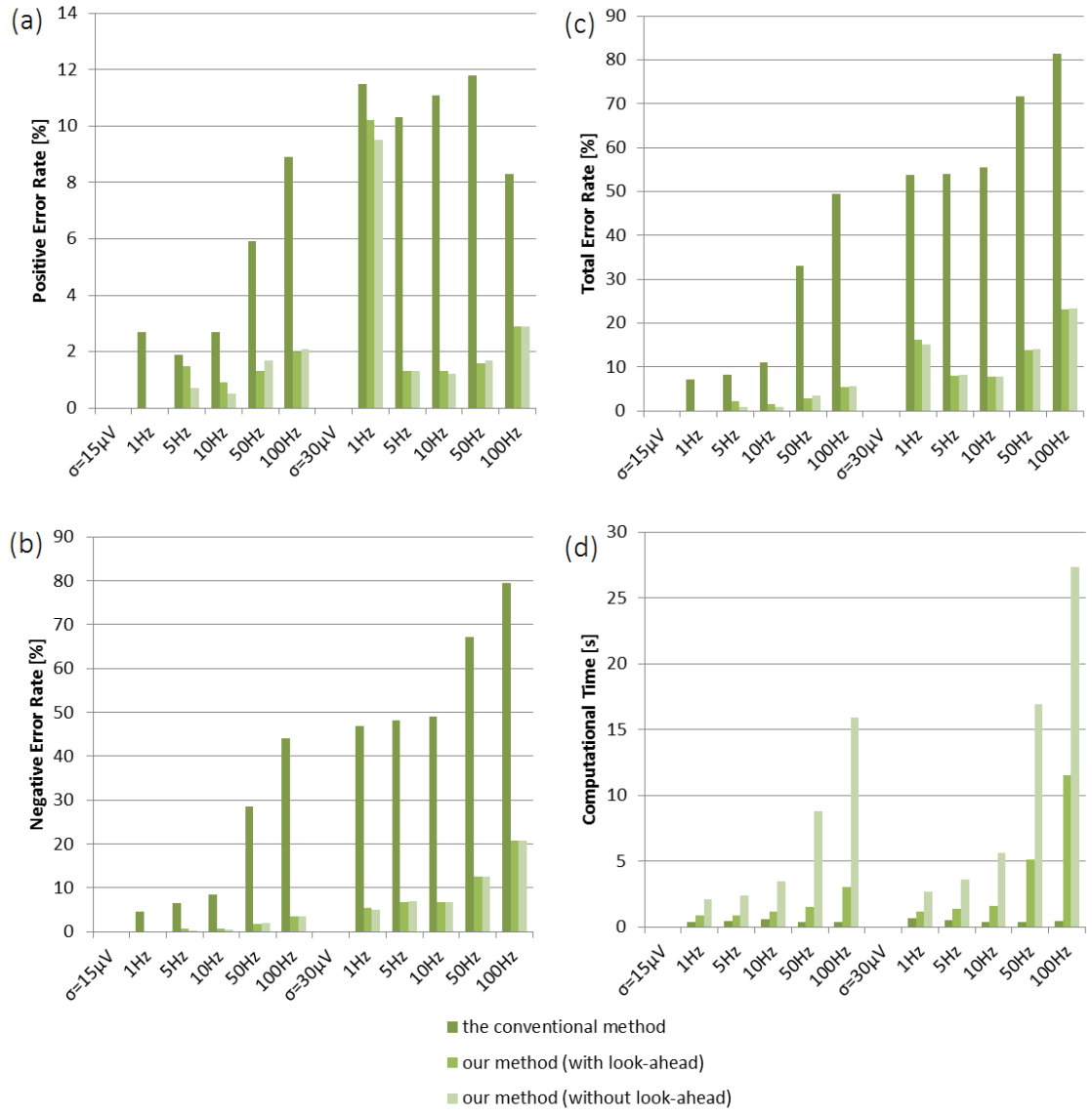

Figure 2.5. Error rates and computational time in spike detection and sorting of simulated signals by using conventional method and our method. Under all conditions, the error rate of our method was lower than that of the conventional method. The difference was particularly big for higher firing rates and higher noise level. The performance of our method was basically the same between with and without look-ahead elimination. The longest computational time (our method without look-ahead elimination for rate = 1 Hz rate and σ = 30 μV) was shorter than the signal length (60s). Look-ahead elimination reduced the computational time of our method to less than half. (a) Positive error rate (PER). (b) Negative error rate (NER). (c) Total error rate (TER). (d) Computational time.

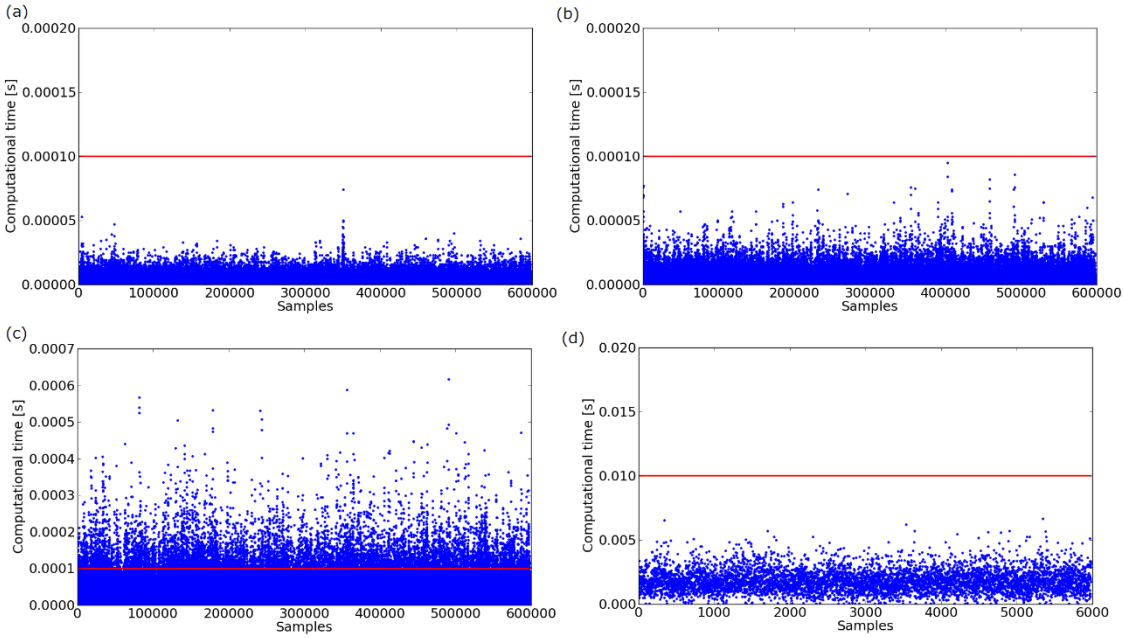

Figure 2.6. Computational time of our method at each sampling point. Red lines indicate sampling interval of each sampling step or each bin. (a) Computational time at each sampling point in processing of simulated signal with σ = 15 μV and firing rate = 100 Hz. Sampling interval was 0.0001 s and computational time was shorter than that at every sampling time, indicating that real-time processing without delay is possible. (b) Computational time at each sampling point in processing of simulated signal with σ = 30μV and firing rate = 50 Hz. Sampling interval was 0.0001 s and computational time was shorter than that at every sampling time, indicating that real-time processing without delay is possible. (c) Computational time at each sampling point in processing of simulated signal with σ = 30 μV and firing rate = 100 Hz. Sampling interval was 0.0001 s, and there were sampling points where the computational time was longer than that, indicating that real-time processing without delay is impossible. (d) Computational time for each 10 ms bin (100 sampling points per a bin) in processing of simulated signal with σ = 30 μV and firing rate = 100 Hz. Interval between bins was 0.01 s and computational time was shorter than that for every bin, indicating that real-time processing with < 10 ms delay is possible

neural signal. Many spikes were missed by the conventional method, and the signal could not be correctly reconstructed from the estimated spike train. While these negative errors can also be reduced by using previously proposed spike sorting methods for overlapped spikes (Lewicki, 1994; Herbst et al., 2008), those methods have limitations on the number of overlaps, and they miss complexly overlapped spikes (more than three or four spikes are overlapped). Therefore, the NER

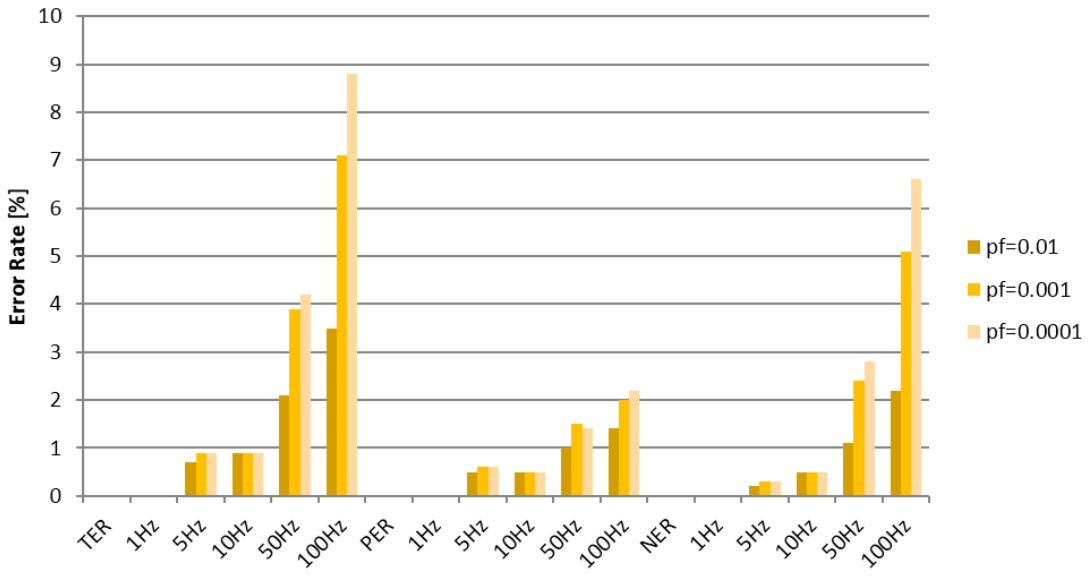

Figure 2.7. Error rates in spike detection and sorting of simulated signals for various firing rates by using our method with look-ahead elimination, when p_t was set to $1 \times 10^{-2}, 1 \times 10^{-3}, 1 \times 10^{-4}$. All the settings of p_t resulted in comparable performance for lower firing rates. In contrast, for higher firing rates, a higher p_t resulted in better performance.

with these methods is higher than the sum of the content rates of spike overlaps including more than three spikes, as shown in Table 1. The NER with our method is lower due to the decomposition of the arbitrary number of spike overlaps, which is one of the advantages of our method.

The error rates of our method, with and without look-ahead elimination, were lower than those of the conventional method not only for a large number of overlaps but also for a higher noise level. One of the reasons for this difference is the use of the voltage threshold to detect spikes in the conventional method. As Herbst et al. (2008) noted, spike detection with a voltage threshold tends to generate detection errors. The high standard deviation of noise increases the frequency of spike detection failure due to the creation of both positive errors (noise exceeding the threshold) and negative errors (spikes below the threshold). Our method is also affected by noise, but detection without a voltage threshold makes our method more robust to higher noise levels. In addition, if the voltage exceeds the threshold at an incorrect position in a spike waveform, the extracted waveform and the spike template will be misaligned (some misalignment is evident in Figure 2.8), possibly causing the sorting to fail. The use of a voltage threshold often causes errors, especially for high noise levels and many spike overlaps.

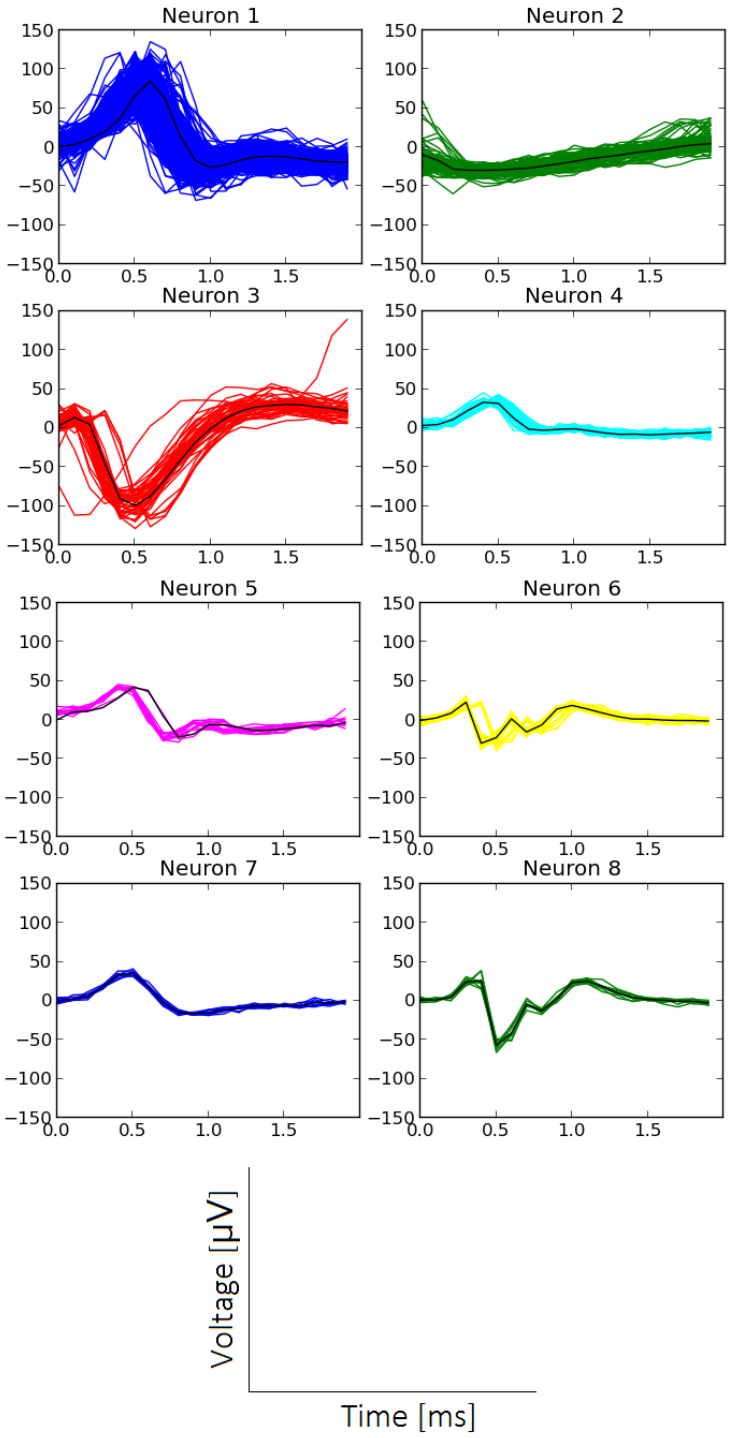

Figure 2.8. Clusters of spike waveforms (colored lines) and spike templates (black lines) extracted from neural signal recorded from cortical neurons cultured on MEA by using DBSCAN. Eight different spike templates were obtained. Colors were determined arbitrarily and do not correspond to those in other figures.

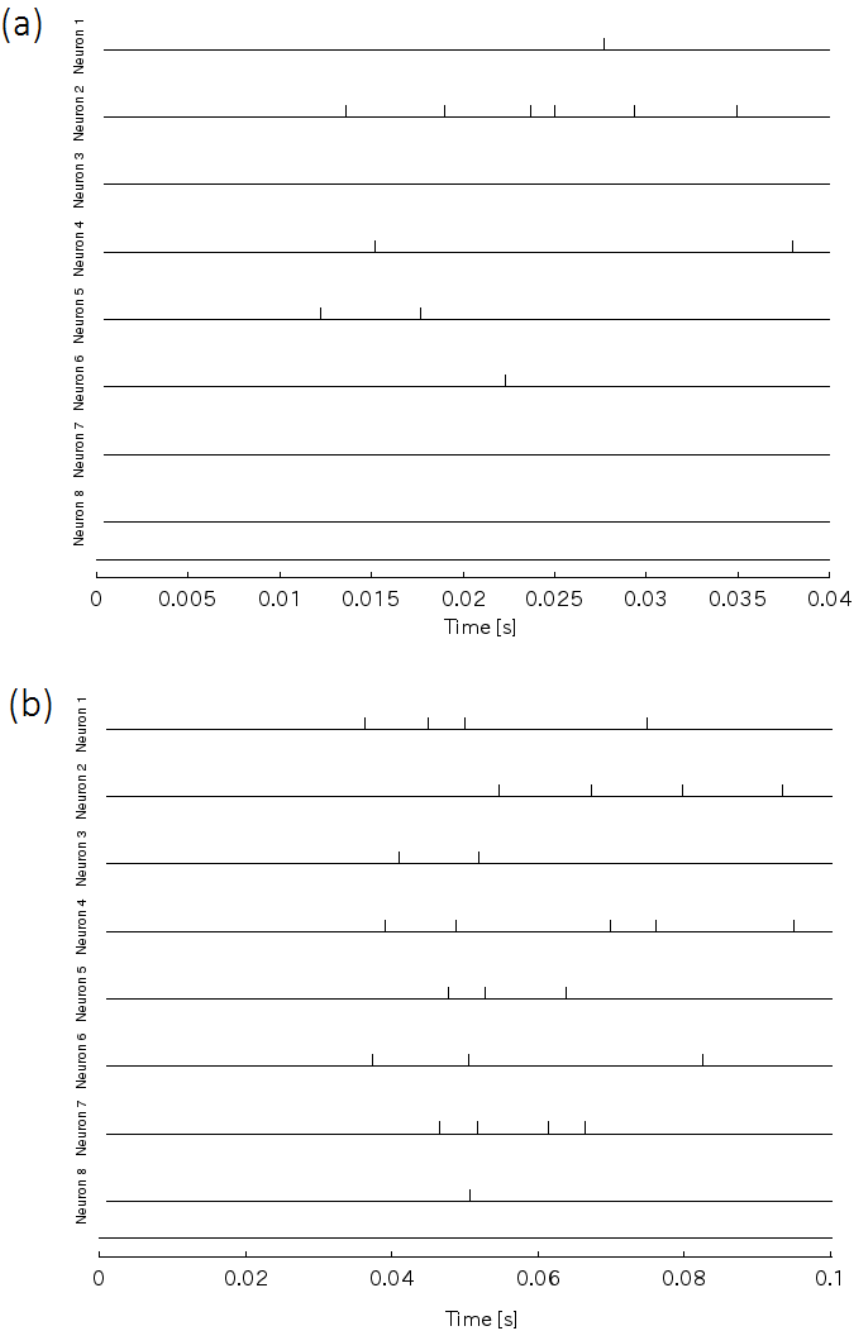

Figure 2.9. Spike trains estimated from signal (shon in Figure 5) recorded from cultured primary cortical neurons by using conventional method and our method with look-ahead elimination. A greater number of spikes was estimated by using our method because overlapped spikes missed by the conventional method were detected by our method. (a) Estimation by using conventional method: 12 spikes were detected. (b) Estimation by using our method: 26 spikes were detected.

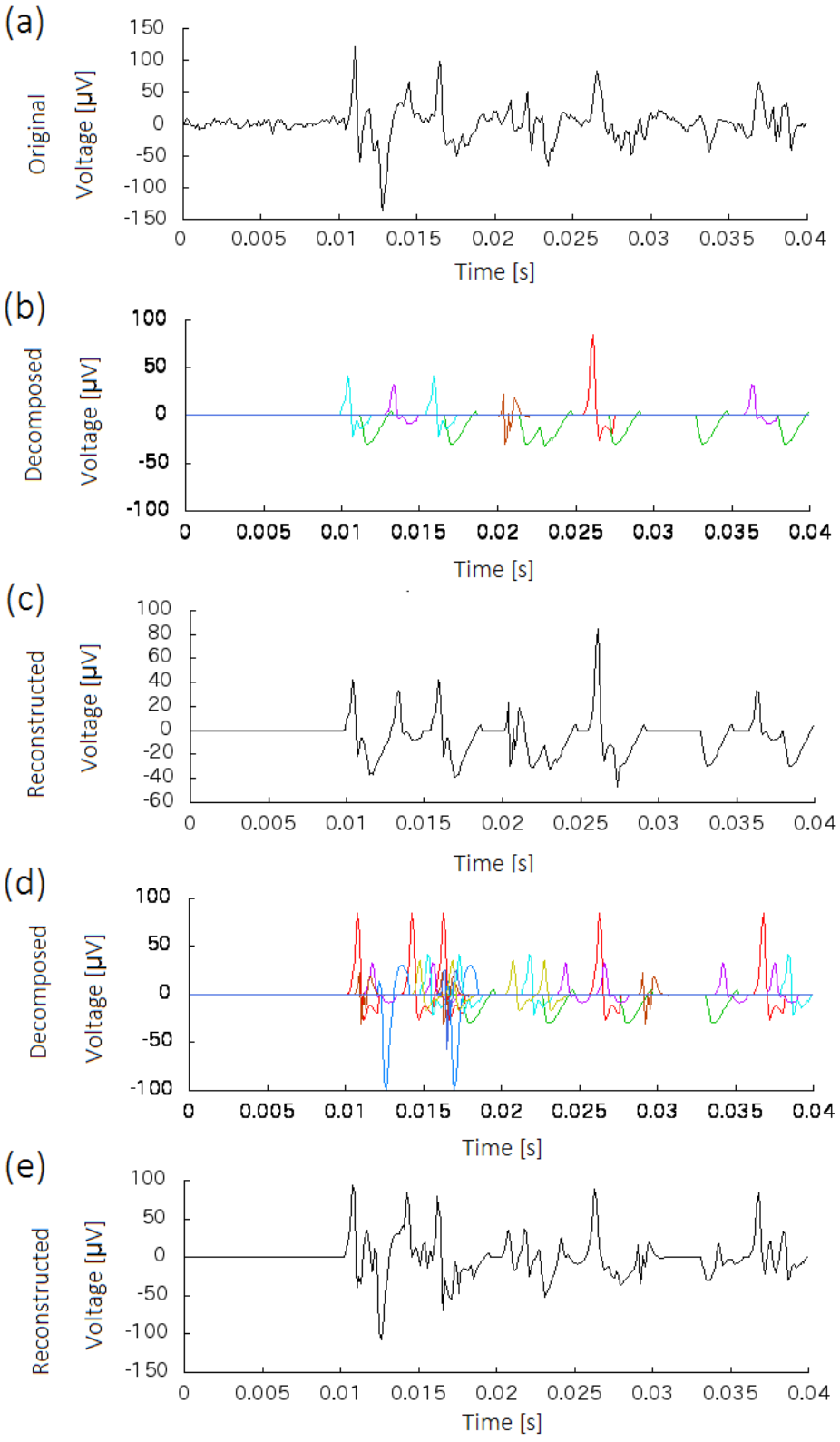
(a)
Original
Voltage [μV]
150
100
50
0
-50
-100
-150
0
0.005
0.01
0.015
0.02
0.025
0.03
0.035
0.04
Time [s]
(b)
Decomposed
Voltage [μV]
100
50
0
-50
-100
0
0.005
0.01
0.015
0.02
0.025
0.03
0.035
0.04
Time [s]
(c)
Reconstructed
Voltage [μV]
100
80
60
40
20
0
-20
-40
-60
0
0.005
0.01
0.015
0.02
0.025
0.03
0.035
0.04
Time [s]
(d)
Decomposed
Voltage [μV]
100
50
0
-50
-100
0
0.005
0.01
0.015
0.02
0.025
0.03
0.035
0.04
Time [s]
(e)
Reconstructed
Voltage [μV]
100
50
0
-50
-100
-150
0
0.005
0.01
0.015
0.02
0.025
0.03
0.035
0.04
Time [s]

Figure 2.10. Original shape of neural signal (shown in Figure 2.5) recorded from primary cortical neurons cultured on MEA, spike waveforms detected by conventional method and our method with look-ahead elimination, and signal reconstructed from detected spike waveforms. A greater number of spikes was estimated by our method because overlapping spikes missed by conventional method were detected by our method. Moreover, the signal reconstructed by our method was closer to the original signal than that reconstructed by the conventional method, which means the estimation accuracy of our method is better. (a) Original shape of neural signal recorded from primary cortical neurons cultured on MEA. (b) Spike waveforms detected by conventional method (colors were determined arbitrarily and do not correspond to those in other figures). (c) Signal reconstructed from spike templates and spike trains estimated by the conventional method. (d) Spike waveforms detected by our method. (e) The signal reconstructed from spike templates and spike trains estimated by our method (colors were determined arbitrarily and do not correspond to those in other figures).

The unnaturally high PER for our method with and without look-ahead elimination at 1 Hz and σ = 30 μV (Figure 2.5 (a)) was also caused by the effect of a high noise level. If the standard deviation of noise is high, noise which could not be distinguished from spikes (artifact noise) is created. The detection of artifact noise was interpreted as a positive error, and a lower firing rate made the denominator smaller in the PER calculation. Consequently, with our methods (with and without look-ahead elimination), only the PER was unnaturally high in this condition. This phenomenon is inevitable in spike detection and sorting with spike templates. Moreover, our method suffered false detections due to artifact noise with a spike-like shape. The reason for the high PER with the conventional method for 1 Hz and σ = 15 μV is attributed to the same cause. In contrast, the PER with our method was low under the same conditions. This means that the standard deviation of noise that produced these positive errors was higher with our method than that with the conventional one.

Our finding that the computational time of our method was shorter than the signal length under all assessed conditions (especially with look-ahead elimination) and that there was no delay in the processing at each sampling points under almost all conditions show that our method is suitable for real-time application. Though the higher firing rates and higher noise levels caused relatively high computational cost and a < 10 ms delay, this delay will not cause the system to fail because the firing rates of most neurons depend on the internal state of the neuronal network and on the external inputs (Brown et al, 2004) and firing with a high frequency is often an instantaneous phenomenon. Moreover, for brain-machine interface applications having a < 100 ms delay (Lebedev et al., 2005), the < 10 ms delay will not significantly degrade total performance.

In contrast to our method, a nearly constant time was needed for the conventional method under

various conditions. It is natural that the computational cost increases with the number of spikes to be computed, and the constant computational time was due to the high NER. This means that many overlapped spikes were detected as a single spike, and many spikes needing to be computed were missed.

Another reason for increased computational cost is the larger number of spike templates, which leads to a larger number of spike train candidates. Furthermore, the existence of more candidates reduces the probability for each candidate and causes a larger number of candidates to be eliminated. Therefore, the computational cost will not increase like the cost of the Baum-Welch algorithm, which has a cost of $O(N^M)$.

The experimental results (Figure 2.7) indicated that our algorithm showed better performance when p_t was set to the high value. However, unrealistic values of p_t should be avoided. For example, $p_t = 0.5$ means the 5000 Hz firing rate for the experimental conditions in this paper and such an unrealistic setting causes invalid estimation. Consequently, p_t should be determined around the maximum firing rate which can appear in recorded signals.

One expansion of our method is the non-parametric Bayesian approach, which assumes the Dirichlet prior for the spiking probabilities and integrates out parameters in the posterior distribution (Rasmussen, 2000; Gasthaus et al., 2008; Wood and Black, 2008). Though this approach enables estimation independent of parameters like p_t, the resulting performance improvement would be slight because the experimental results indicated that using the optimally tuned p_t resulted in good performance under various conditions, so p_t did not have to be individually tuned for each datum and each neuron.

Though our method can robustly detect and sort spikes under various conditions, it has some limitations. First, the simultaneous generation of spikes by more than two neurons in one sampling time is not considered in our model. While this limitation does not exclude most of the overlaps and is looser than that for previous methods (Lewicki, 1994; Herbst et al., 2008), a few non-modeled overlaps still remain. Second, the shapes of the spikes are assumed to be fixed in our model though spike waveforms can change due to bursting or electrode drift (Lewicki, 1998). This change could be modeled like Calabrese and Paninski (2011) did, but doing so would increase the computational cost. Finally, our method does not work properly if invalid spike templates are generated in the pre-processing phase. Though spike templates could be extracted from non-overlapped spikes in the work reported here, if there are only a few non-overlapped spikes and the extraction of spike templates is impossible, the procedure will not work correctly. The possible extension of our method is to the on-line generation of spike templates without the conventional pre-processing process; however, that requires the method which can accommodate the change of the number of neurons in analyses based on estimated spike trains.

2.6 Summary of the chapter

In this chapter, we proposed the fast sequential method that can robustly detect and sort arbitrarily overlapped spikes recorded with arbitrary types of electrodes. We constructed probabilistic models of the extracellular voltage recording and spike generation, which can generate overlapped spikes. We derived a computationally efficient sequential Bayesian inference algorithm based on these models that is used to calculate the probability of spike existence at each sampling time. Assessment of the feasibility of our method with simulated neural signals and a real neural signal showed that our method can robustly detect and sort complexly overlapped spikes. Our method with look-ahead elimination was demonstrated to be suitable for real-time application as it has a delay of less than < 10 ms even under the worst case conditions.

The contents of this section was partly published in

Tatsuya Haga, Osamu Fukayama, Yuzo Takayama, Takayuki Hoshino, Kunihiko Mabuchi, ``Efficient Sequential Bayesian Inference Method for Real-time Detection and Sorting of Overlapped Neural Spikes," Journal of Neuroscience Methods, Vol. 219, Issue 1, pp. 92-103, 2013.

Chapter 3
Simultaneous Inference of Templates and Timings of Highly Overlapped Neural Spikes

3.1 Overview

In Chapter 2, we have developed the algorithm to detect and sort overlapped spikes in real-time with given spike templates. In the experiment, we extracted spike templates from the signal by the traditional approach that uses the threshold and the clustering algorithm. However, overlaps can degrade the estimation of spike templates. Especially if we only have the short data which contains many overlaps (e.g. recording of bursts or responses to external stimuli), each single template cannot be extracted by the traditional approach. If we know either spike templates or spike timings, we can calculate the other by the method in Chapter 2 or signal averaging. However, spike overlaps make it difficult to identify not only spike templates but also spike timings.

In this chapter, we attempted to develop a spike sorting method to estimate spike templates and spike timings simultaneously from the signal containing arbitrarily overlapped spikes. Extracellular recordings and generation of spikes were modeled under the same assumption and approximation made in Chapter 2. The model becomes a kind of the hidden Markov model (HMM) and spike templates and spike timings were simultaneously estimated by α-β algorithm and Expectation-Maximization (EM) algorithm. However, if overlaps of arbitrary numbers of spikes are allowed in the estimation of spike templates, over-decomposition of a non-overlapped spike waveform into many tiny spike-like waveforms which are obtained as spike templates can occur because that is the best way to fit the model to the data. To avoid that undesirable decomposition, we imposed the probabilistic penalty on the number of overlaps in the model. Computational cost of estimation was reduced by approximating low probabilities to zero, which is the same approximation as Chapter 2. These implementation enable us to remove the restriction of the number of spikes in an overlap without the problem of high computational cost and over-decomposition of spikes. We

applied our method to simulated neural signals and recordings from cortical neurons cultured on MEA and confirmed that our method could robustly estimate appropriate templates and timings of complexly overlapped spikes.

3.2 Methods

3.2.1 The model of extracellular voltage recordings

We assumed that T time samples of the recorded signal $y_{1:T} = \{y_1, y_2, \dots, y_T\}$ contain spikes generated by N neurons with additive Gaussian noise with variance σ, and the vector $\boldsymbol{\mu}_n = (\mu_n[1], \mu_n[2], \dots, \mu_n[M])$ was defined as the waveform of the spike generated by neuron n. Furthermore, $x_{1:T} = \{x_1, x_2, \dots, x_T\}$ was defined as the number of the neuron which started to generate a spike at each time samples (if there is no spike, $x_t = 0$). Based on these assumptions, we had the recording model with the spike train vector $\mathbf{z}_t = (x[t], x[t-1], \dots, x[t-M+1])$:

$$\mathrm{p}(y_t|\mathbf{z}_t, \boldsymbol{\mu}_{1:N}, \sigma) = \frac{1}{\sqrt{2\pi\sigma}} \exp\left(-\frac{\left(y_t - \sum_{\tau=1}^{M} \mu_{z_t[\tau]}[\tau]\right)^2}{\sigma}\right) \tag{3.1}$$

3.2.2 The model of spike trains

We also derived the model of the spike train $\mathbf{z}_t$. We assumed x_t followed the multinomial distribution and the probability for a neuron to fire was determined with the parameters ω and $\boldsymbol{\pi} = (\pi_1, \dots, \pi_N)$. We also took into account the refractory period, to be more precise, once a neuron fired, it cannot fire again in M time samples. Furthermore, in our model, the probability for a neuron to fire was reduced in M time samples after another neuron fired. This assumption made our method avoid decomposing the signal to too many overlapped spikes.

After all, the model was

$$\mathrm{p}(\mathbf{z}_t|\mathbf{z}_{t-1}, \boldsymbol{\pi}) = \begin{cases} \omega\pi_{z_t[1]}\mathrm{F}(\mathbf{z}_t, \mathbf{z}_t[1]) & , \text{if } z_t \in \mathrm{C}_z \wedge 1 \le z_t[1] \le N \\ \omega\left(1 + \sum_{k=1}^{N} \pi_k\left(1 - \mathrm{F}(\mathbf{z}_t, k)\right)\right) & , \text{if } z_t \in \mathrm{C}_z \wedge z_t[1] = 0 \\ 0 & , \text{if } \mathbf{z}_t \notin \mathrm{C}_z \end{cases} \tag{3.2}$$

$$\mathrm{C}_z = \{\mathbf{z}_t | 2 \le \forall\tau \le M, z_t[\tau] = z_{t-1}[\tau - 1]\} \tag{3.3}$$

$$\mathrm{F}(\mathbf{z}_t, n) = \begin{cases} 0, \text{if } 2 \le \exists\tau \le M, z_t[\tau] = n \\ \phi^{\sum_{\tau=2}^{M}\sum_{k=1}^{N}\delta_{k,z_t[\tau]}}, \text{else} \end{cases} \tag{3.4}$$

$$\omega\left(1 + \sum_{k=1}^{N} \pi_k\right) = 1 \tag{3.5}$$

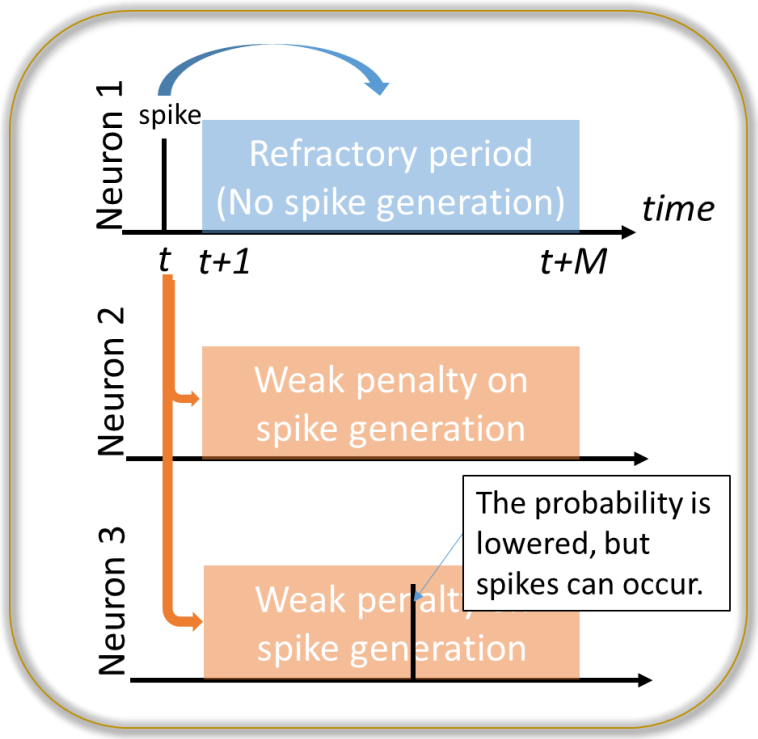

Figure 3.1. The schematic view of the model of spike trains. When a neuron generates a spike, the neuron cannot generate spikes (the refractory period) and probabilities for other neurons to generate spikes are lessened (the probabilistic penalty to avoid too much decomposition of a spike) in a certain period of time.

$\delta_{0,x_{t-1}[\tau]}$ was Dirac's delta and ϕ was the weighting coefficient preventing over-decomposition. The schematic view of the model is shown in Figure 3.1.

3.2.3 Estimation of hidden variables and parameters

Expectation-Maximization (EM) algorithm (Bishop, 2006) was used to estimate parameters in above-mentioned model. EM algorithm can estimate model parameters in the presence of hidden variables by repeating two steps, E-step and M-step. The schematic view of EM algorithm is shown in Figure 3.2.

In E-step, probability distributions of hidden variables $\gamma(\mathbf{z}_t) = p(\mathbf{z}_t|y_{1:T}, \Theta)$, $\xi(\mathbf{z}_t, \mathbf{z}_{t-1}) = \mathrm{p}(\mathbf{z}_t, \mathbf{z}_{t-1}|y_{1:T}, \Theta)$ were estimated under fixed model parameters by α-β algorithm (Bishop, 2006). The schematic view of α-β algorithm is shown in Figure 3.3. In this algorithm, alpha-messages $\hat{\alpha}(\mathbf{z}_t) = p(\mathbf{z}_t|y_{1:t}, \Theta)$ were recursively estimated as

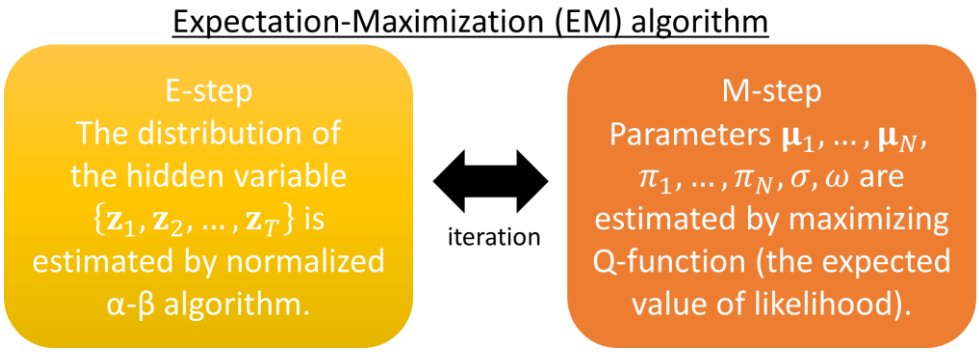

Figure 3.2. Schematic view of expectation-maximization algorithm. Probabilistic distributions of hidden variables at every sampling time and maximum-likelihood parameters are alternately estimated. The likelihood function monotonically increases in each update and the convergence to local optima is warranted.

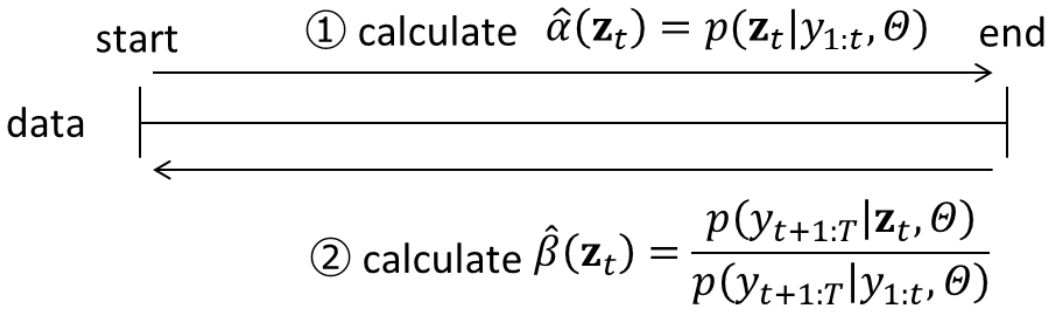

Figure 3.3. Schematic view of α-β algorithm. Firstly, alpha messages are sequentially calculated for datum at every sampling time in the forward direction from the start to the end, by using the alpha message at previous sampling time. Secondly, alpha messages are sequentially calculated for datum at every sampling time in the backward direction from the end to the start. Finally, at every sampling time, probabilistic distributions of hidden variables ($\gamma(\mathbf{z}_t)$, $\xi(\mathbf{z}_t, \mathbf{z}_{t-1})$). are calculated from the alpha message and the beta message.

$$\hat{\alpha}(\mathbf{z}_1) = \frac{p(y_1|\mathbf{z}_1, \Theta)p(\mathbf{z}_1)}{\sum_{\mathbf{z}_1} p(y_1|\mathbf{z}_1, \Theta)p(\mathbf{z}_1)} \tag{3.6}$$

$$\alpha(\mathbf{z}_t) = p(y_t|\mathbf{z}_t, \Theta) \sum_{\mathbf{z}_{t-1}} p(\mathbf{z}_t|\mathbf{z}_{t-1}, \Theta)\hat{\alpha}(\mathbf{z}_{t-1}) \tag{3.7}$$

$$c_t = p(y_t|y_{1:t-1}, \Theta) = \sum_{\mathbf{z}_t} \alpha(\mathbf{z}_t) \tag{3.8}$$

$$\hat{\alpha}(\mathbf{z}_t) = \frac{\alpha(\mathbf{z}_t)}{c_t} \tag{3.9}$$

After that, beta-messages $\hat{\beta}(\mathbf{z}_t) = \frac{p(y_{t+1:T}|\mathbf{z}_t,\theta)}{p(y_{t+1:T}|y_{1:t},\theta)}$ were recursively estimated as

$$\hat{\beta}(\mathbf{z}_T) = 1 \tag{3.10}$$

$$\hat{\beta}(\mathbf{z}_t) = \frac{1}{c_{t+1}} \sum_{\mathbf{z}_{t+1}} \hat{\beta}(\mathbf{z}_{t+1}) p(y_{t+1}|\mathbf{z}_{t+1},\theta) p(\mathbf{z}_{t+1}|\mathbf{z}_t,\theta) \tag{3.11}$$

$\gamma(\mathbf{z}_t)$ and $\xi(\mathbf{z}_t, \mathbf{z}_{t-1})$ were calculated from alpha-messages and beta-messages.

$$\gamma(\mathbf{z}_t) = \hat{\alpha}(\mathbf{z}_t)\hat{\beta}(\mathbf{z}_t) \tag{3.12}$$

$$\xi(\mathbf{z}_t, \mathbf{z}_{t-1}) = (c_n)^{-1} \hat{\alpha}(\mathbf{z}_{t-1}) \mathrm{p}(y_t|\mathbf{z}_t) \mathrm{p}(\mathbf{z}_t|\mathbf{z}_{t-1}) \hat{\beta}(\mathbf{z}_t) \tag{3.13}$$

In M-step, model parameters were updated to maximize the expected value of the complete data log-likelihood (Q-function):

$$\mathrm{Q}(\theta) = \sum_{z_{1:T}} \mathrm{p}(z_{1:T}|y_{1:T}, \theta^{\mathrm{old}}) \log \mathrm{p}(\, y_{1:T}, z_{1:T} |\, \theta^{\mathrm{new}})$$

$$= \log p(z_1) + \sum_{t=2}^{T} \sum_{z_t, z_{t-1}} \xi(z_t, z_{t-1}) \log \mathrm{p}(z_t|z_{t-1}, \theta) \tag{3.14}$$

$$+ \sum_{t=1}^{T} \sum_{z_t} \gamma\,(z_t) \log p(y_t|z_t, \theta)$$

Details of derivation is provided in Appendix B. ω and $\boldsymbol{\pi}$ were updated as

$$\omega = \frac{1}{(1 + \sum_{k=1}^{N} \pi_k)} \tag{3.14}$$

$$\pi_n = \frac{\sum_{t=1}^{T} \sum_{\mathbf{z}_{t-1}} \sum_{\mathbf{z}_t \, s.t. \, z_t[1]=n} \xi(\mathbf{z}_t, \mathbf{z}_{t-1})}{\sum_{t=1}^{T} \sum_{\mathbf{z}_{t-1}} \left(\sum_{\mathbf{z}_t} \xi(\mathbf{z}_t, \mathbf{z}_{t-1}) - \sum_{\mathbf{z}_t \, s.t. \, z_t[1]=0} \xi(\mathbf{z}_t, \mathbf{z}_{t-1}) (1 - \mathrm{F}(\mathbf{z}_t, n)) \right)} \tag{3.15}$$

$\boldsymbol{\mu}_n$ was updated by solving following equation:

$$\mathbf{A}\boldsymbol{\mu}_{\mathbf{all}} = \mathbf{b} \tag{3.16}$$

$$\boldsymbol{\mu}_{\mathbf{all}} = (\mu_1[1], \mu_1[2], \dots, \mu_1[M], \mu_2[1], \mu_2[2], \dots, \mu_N[M])^T \tag{3.17}$$

$$\mathbf{b}^{(\tau+(n-1)(M+1))} = \sum_{t=1}^{T} y_t \sum_{\mathbf{z}_t \, s.t. \, z_t[\tau]=n} \gamma(\mathbf{z}_t) \tag{3.18}$$

$$\mathrm{A}_{\tau+(n-1)(M+1), \tau'+(n'-1)(M+1)} = \begin{cases} \sum_{t=1}^{T} \sum_{\mathbf{z}_t \, s.t. \, z_t[\tau]=n} \gamma(\mathbf{z}_t) \;, \tau = \tau', n = n' \\ 0, \tau = \tau', n \neq n' \\ \sum_{t=1}^{T} \sum_{\mathbf{z}_t \, s.t. \, z_t[\tau]=n, z_t[\tau']=n'} \gamma(\mathbf{z}_t) \;, \tau \neq \tau' \end{cases} \tag{3.19}$$

σ was updated as

$$\sigma = \frac{1}{T}\sum_{t=1}^{T}\sum_{\mathbf{z}_t}\gamma(\mathbf{z}_t)\left(y_t - \sum_{\tau=1}^{M+1}\mu_{z_t[\tau],\tau}\right)^2 \tag{3.20}$$

The number of neurons *N* was chosen by minimizing Bayesian information criterion (BIC) (Bishop, 2006).

$$\mathrm{BIC} = -2\log p(y_{1:T}|\theta) + \log T\ (\mathrm{N}(\mathrm{M}+1)+2) \tag{3.21}$$

$$\log p(y_{1:T}|\theta) = \sum_{t=1}^{T}\log c_t \tag{3.22}$$

These procedure needed too high computational cost because of high dimensionality of $\mathbf{z}_t$. To reduce the computational cost, $\hat{\alpha}(\mathbf{z}_t)$ smaller than a given threshold p_{th} was approximated by zero and we calculated all the probabilities for only $\left\{\mathbf{z}_t^{(i)}\right\}_{1\le i\le I_t}$, nonzero instances of z_t. I_t was the number of nonzero instances at sampling time t.

3.3 Experiments

3.3.1 Assessments with simulated signals

We assessed the performance of our method by applying it to the 0.3-second simulated signal containing a lot of complex overlaps of spikes (shown in Figure 3.1). In simulation, spike shapes shown in Fig. 3.2 (a) were present in the signal whenever indicated by the timings shown in Figure 3.3 (a). The signal was additionally corrupted by adding Gaussian noise. The standard deviation of noise was 15 μV and the sampling rate was 10 kHz. We applied our method by setting the parameter values to $\phi = 0.01, p_{\mathrm{th}} = 1\times10^{-15}, M = 1.5\mathrm{ms}$ and detected spikes when the probability $\gamma(\mathbf{z}_t)$of spiking exceeded the value of 0.5.

3.3.2 Assessments with the real neural signal

We also assessed our method with the eight-second signal recorded from neurons cultured on the Multi-Electrode Array (MEA). The signal used in the assessment (shown in Fig. 3.4 (a)) was recorded in the same condition with the signal used in Chapter 2. Details of cell culture and recording methods are shown in Appendix A. We applied our method to the signal with the setting of parameters same as the simulation experiment.

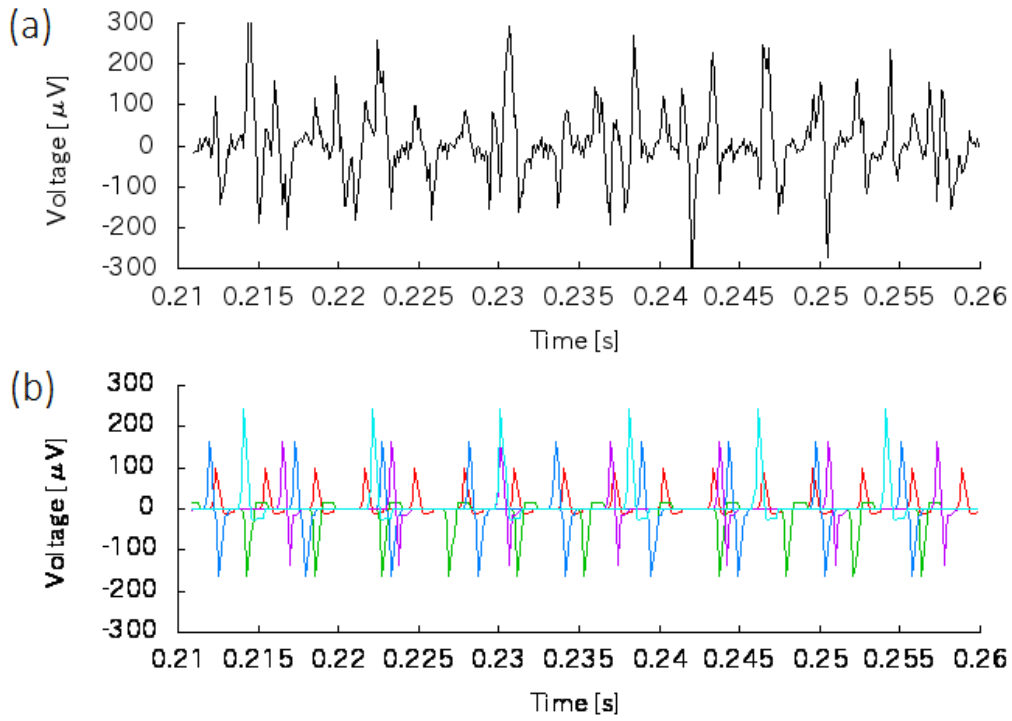

Figure 3. 4. A part of the simulated signal and spike waveforms contained in the signal. Almost all spikes were overlapped and there were complex overlaps of more than three neurons. (a) Simulated signal. (b) Spike waveforms contained in the signal.

3.4 Results

3.4.1 Assessments using simulated signals

As the result, all the spike templates were appropriately estimated as shown in Figure 3.2 (b) and complexly overlapped spikes shown in Fig. 3.1 were all detected. However, 2 positive errors and 25 negative errors were found as shown in Fig. 3.3 (b) (The number of spikes in simulation (Fig. 3.3 (a)) was 302). Note that the numbering of neurons was arbitrary and not same between simulation and in estimation.

3.4.2 Assessments using the real neural signal

As the result, eight spike templates were created as shown in Fig. 4(d) and the spike timings were estimated as shown in Fig. 3.4(b). In Fig. 3.4(b), more than three or four spikes were superimposed at the same position, which means complex overlaps were decomposed. We reconstructed the signal from estimated timings and templates by the recording model and obtained the signal similar with the original (Fig. 3.4(c)). It means that the decomposition of complexly overlapped spikes was appropriate.

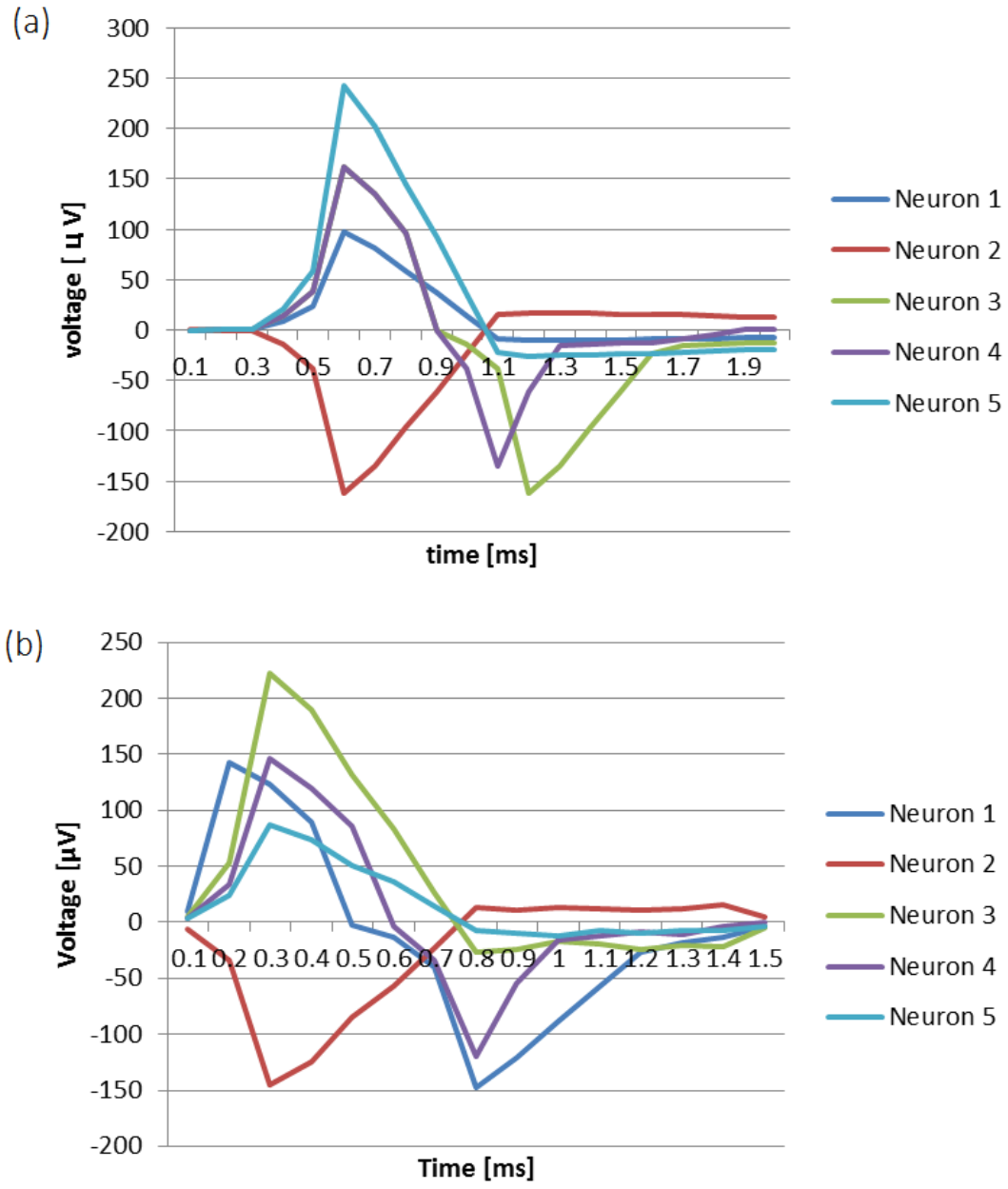

Figure 3. 2. Five spike templates used in the simulation and spike templates estimated by our method. (a) Spike templates used in the simulation. (b) spike templates estimated by our method

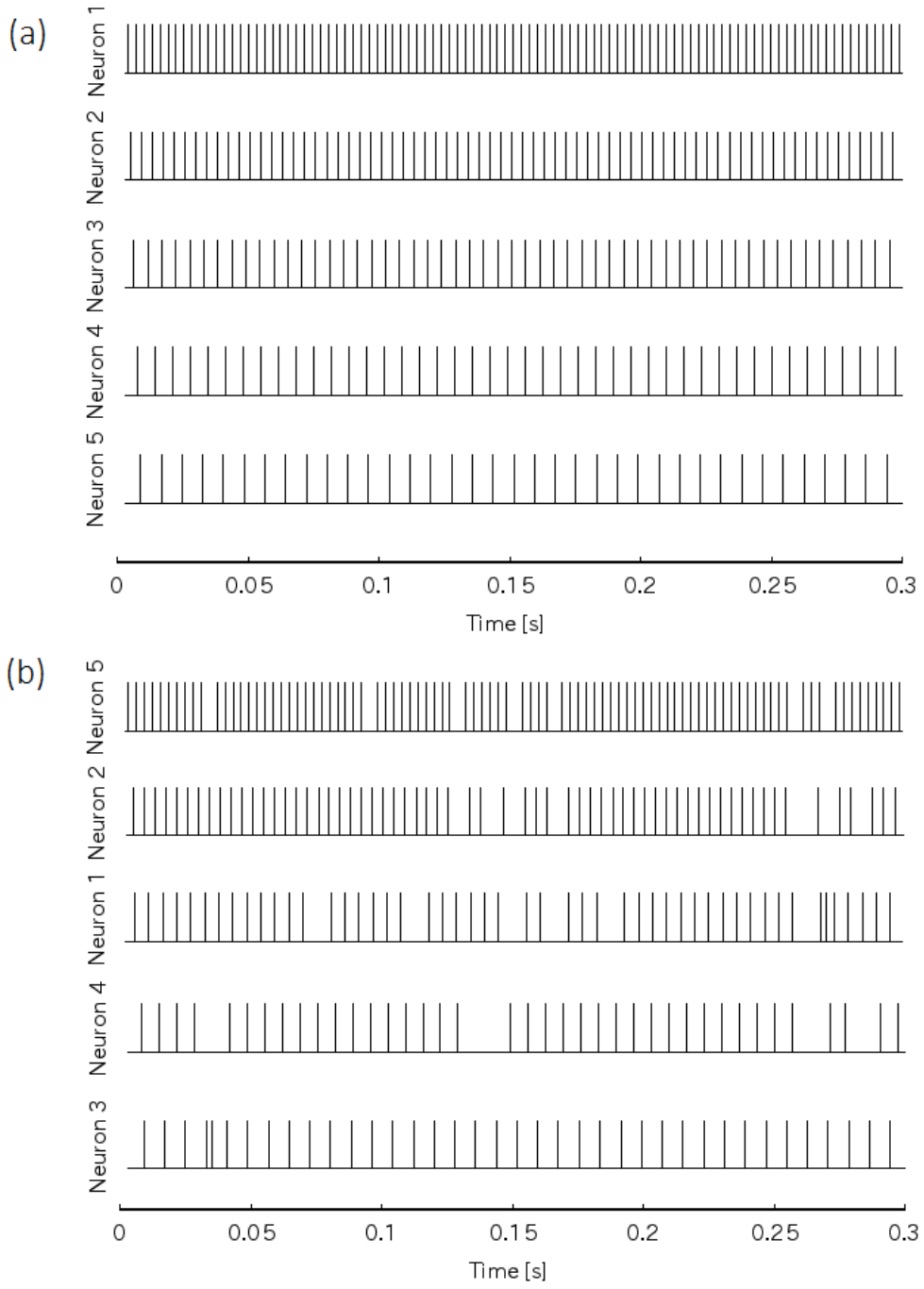

Figure 3. 3. Spike timings used in the simulation and spike timings estimated by our method. (a) Spike timings used in the simulation. (b) spike timings estimated by our method

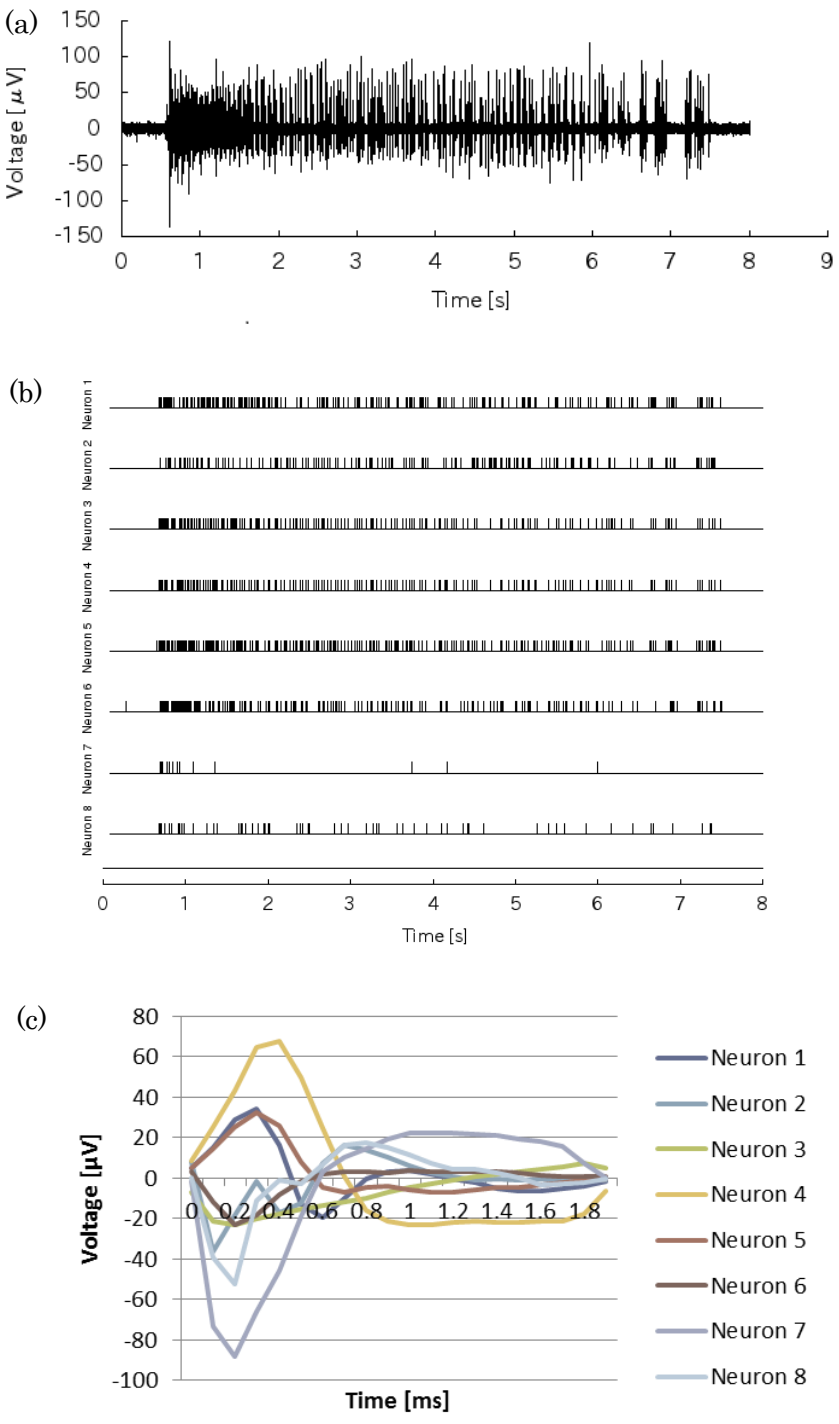

Figure 3. 4. The result of estimation from the signal recorded from cultured cortical neurons by our method. Eight templates and spike timings for eight neurons were obtained. (a) The signal used in the experiment. (b) Spike timings estimated by our method. (d) Eight spike templates estimated by our method.

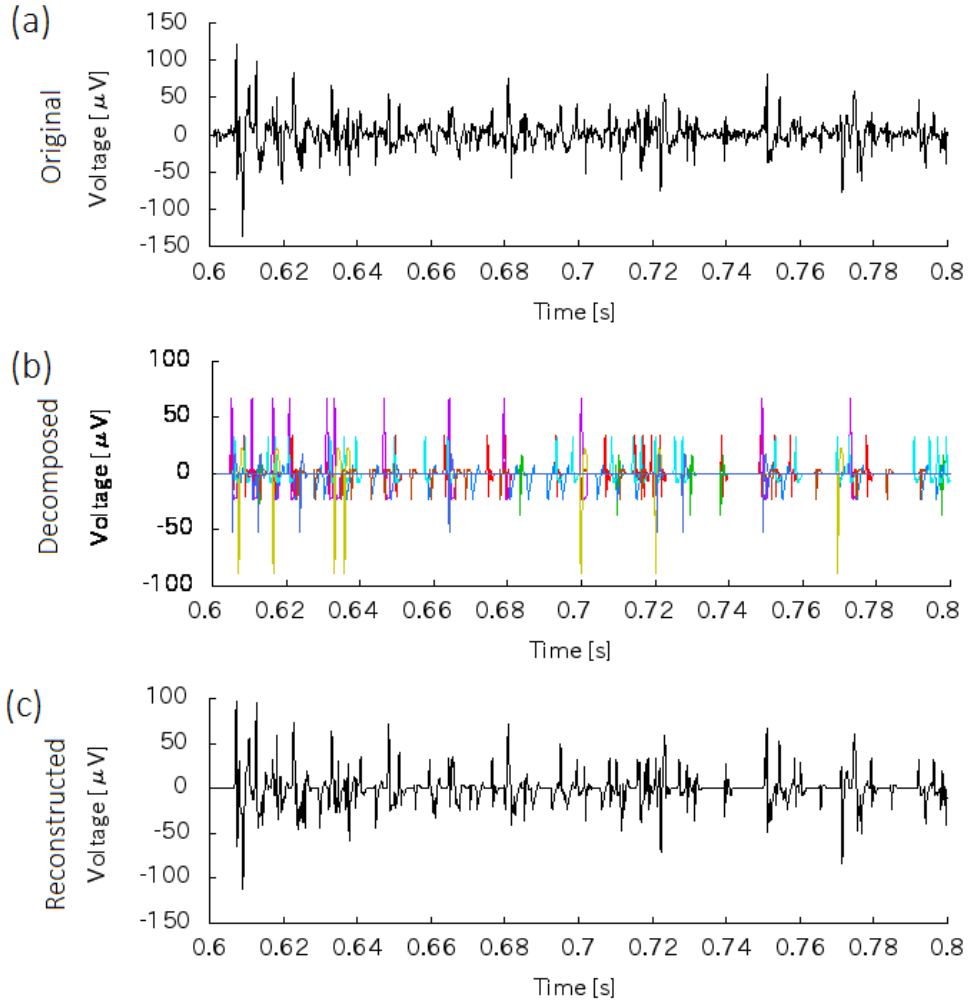

Figure 3. 5. The result of estimation from the signal recorded from cultured cortical neurons by our method. These figures show enlarged view of a part of the signal shown in Figure 3.4 (a). Complexly overlapped spikes could be decomposed and the original signal could be appropriately reconstructed from estimated templates and spike timings. (a) Enlarged plot of a part of the signal shown in Figure 3.4 (a). (b) Spike waveforms detected from the signal by our method. (c) The signal reconstructed from estimated templates and timings.

3.5 Discussion

In the assessments with simulated signals, all the spike templates were appropriately estimated as shown in Figure 3.2 (b). However, 2 positive errors and 25 negative errors were found, as shown in

Figure 3.3 (b) (The number of spikes in simulation (Fig. 3.3 (a)) was 302). One of reasons of these non-negligible negative errors was canceling out of positive and negative spikes. In the worst case, if two spikes that have the same shape and reversed polarities are simultaneously recorded in an electrode, they will be canceled out and nothing will appear in the recorded signal. Even if timings or spike shapes are slightly different, it is possible that levels of spikes are dropped to the same level with noise. It makes spike detection impossible. Another reason is the weak probabilistic penalty on spike overlaps. It prevents a spike is decomposed to many overlapped small spikes, on the other hand, it can be interruption if decomposition to a large number of spikes is appropriate. Whether a spike is decomposed or not is determined by the trade-off of the increase of BIC by the increased number of templates and the decrease of BIC by improved fitting of the model to data. In the assessment, the main reason is the former. (For example, highly overlapped spikes shown in Fig. 3.1 were all decomposed in appropriate level).

We used BIC to determine the number of spike templates in this chapter. Other choices are Akaike information criterion (AIC) (Bishop, 2006), non-parametric Bayesian approach (Rasmussen, 2000; Gasthaus et al., 2008; Wood and Black, 2008), and so on. We also tested them and checked that BIC gives the highest performance. However, the optimality of BIC was checked only for our environment and data. Furthermore, we can obtain only the optimal model that fits data and we cannot prove it is the answer if we use blind data. We should test some criteria for new environments or data and the one which optimizes the performance of the system should be chosen.

In the assessment, long computational time was required for the estimation. Approximately an hour was required to complete the estimation from 8-second real neural signal shown in Figure 3.4 (a). Spike detection and sorting is just the pre-processing of further analyses in many cases, thus long computational time makes users to hesitate to use the method. We present the strategy that reduces the computational time in Chapter 4, but further improvements are required. Otherwise creating templates in parallel with real-time spike detection can improve usability.

In spite of weaknesses mentioned above, the method proposed in this chapter can detect and sort spikes in a case that almost all spikes are complexly overlapped, which have been impossible by previous techniques. However, for these uses, the change of spike shapes by bursting should be modeled. It is the same remaining problem with the method in Chapter 2.

3.6 Summary of the chapter

In this chapter, we developed the method to estimate the spike templates and timings from signals containing overlaps of arbitrary numbers of spikes. In our method, the inference based on HMM with the probabilistic penalty is efficiently calculated with the approximation. We assessed the

performance of the method and showed that it could appropriately decompose the simulated and real signals containing complexly overlapped spikes.

The contents in this section was partly published in

Tatsuya Haga, Yuzo Takayama, Kunihiko Mabuchi, “Estimation of Templates and Timings of Spikes in Extracellular Voltage Signals Containing Overlaps of the Arbitrary Number of Spikes”, 35th Annual International Conference of the IEEE Engineering in Medicine and Biology Society, Osaka, Japan, Jul. 2013

Chapter 4
Combination of the two methods

4.1 Overview

In the previous chapters, we presented the two types of detection and sorting methods of complexly overlapped neural spikes recorded by extracellular voltage recording. In Chapter 2, we proposed the fast sequential method that can detect and sort arbitrarily overlapped spikes in real-time. In Chapter 3, the off-line method for the simultaneous estimation of spike templates and the timings of highly overlapped spikes was proposed. The two methods have the same strong point in that they are robust to overlaps, but their weak points are different. The real-time method (in Chapter 2) can process quickly in order to realize real-time computation, but it cannot create spike templates by itself and requires appropriate spike templates to be prepared. In contrast, the off-line method (in Chapter 3) can extract appropriate spike templates from highly overlapped signals, but it requires a high computational cost and cannot be used for lengthy data or real-time applications. These two methods have complementary characteristics, and their application in combination solves the weak points of the two methods. To detect spikes from lengthy data without spike templates or in real-time applications, it is recommended that the off-line method is applied to clipped data with a short length in order to extract appropriate spike templates and that, subsequently, the real-time method is applied to lengthy data or real-time applications. This procedure will improve performance without long computational time. In this chapter, we applied the two methods to the various data in combination in order to investigate whether the approach increases the performance of the estimation.

4.2 Experiments

We assessed our methods when used in combination with 5-s signals recorded from neurons cultured on the Multi-electrode array. The signal used in the assessment was recorded in the same conditions as the signal used in Chapter 2 and Chapter 3. The details of the cell culture and recording methods are shown in Appendix A. We obtained three single-channel signals, one from the culture at

100 days *in vitro* (signal A) and two from the culture at 45 days *in vitro* (signal B, C). We cut out three 5-s segments from each signal. Consequently, we obtained nine 5-s segments from three signals, and each was named A1, A2, A3, B1, B2, B3, C1, C2, and C3 (shown in Figure 4.1).

First, we applied the off-line method presented in Chapter 3 to the 5-s segments in order to extract the spike templates. The setting of the parameters was the same as those for the experiment in Chapter 3. In consequence, three sets of spike templates were estimated for each single-channel signal. The set that had the largest number of spike templates in each signal was chosen for the next procedure.

Next, we applied the real-time method presented in Chapter 2 in order to detect and sort the spikes. The setting of the parameters was the same as those for the experiment in Chapter 2. This can be applied to the entire signal, but we only show the estimated results in the short length.

In order to compare the estimation performance, we also applied the procedure used in Chapter 2 and Chapter 3. The first one was the traditional approach, that is, creating spike templates by applying DBSCAN clustering to the spikes detected from the entire signal (not the 5-s segments) with thresholding and real-time detection and sorting with thresholding and the least-mean-square with templates created by DBSCAN. The second one was the approach tested in Chapter 2. That is, creating spike templates by applying DBSCAN clustering to the spikes detected with thresholdiing from the entire signal and the real-time detection and sorting with the real-time method presented in Chapter 2 with templates created by DBSCAN.

4.3 Results

The spike templates extracted from the entire signal by DBSCAN clustering and the three sets of spike templates extracted from the 5-s segments by our off-line method are shown in Figures 4.2-4.5. Similar waveforms were extracted for the same signal, and basically, the number of spike templates extracted by our method were larger than that with DBSCAN. Spike templates extracted from A2, B3, and C2 were chosen for the next procedure. Furthermore, there was a tendency that the duration of the spike templates of signal A was longer than that for signal B and signal C.

With the extracted spike templates, three types of spike detection and sorting were applied: threshold and least mean square with spike templates extracted by DBSCAN (DB + TLMS), our real-time method with spike templates extracted by DBSCAN (DB + BAYES), and our real-time method with spike templates extracted by our off-line method (BAYES + BAYES). The estimated results and the signals reconstructed from them (same as Chapter 2) for parts of the signals in the 5-s segments are shown in Figures 4.6–4.14. Overlapped spikes ignored by DB + TLMS were detected by DB + BAYES and BAYES + BAYES, therefore, the reconstructed signals of DB + BAYES and

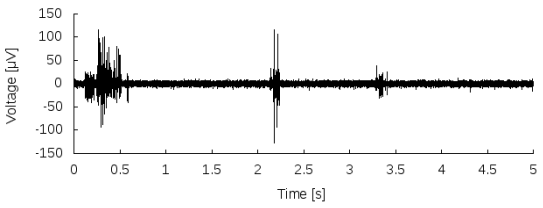

A1

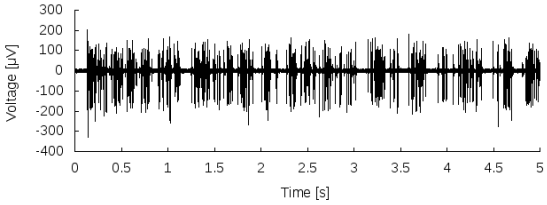

B1

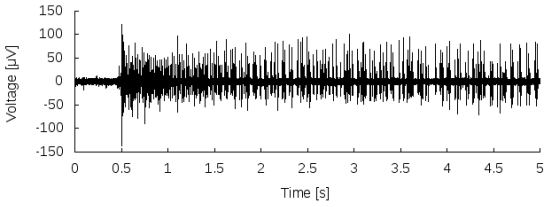

A2

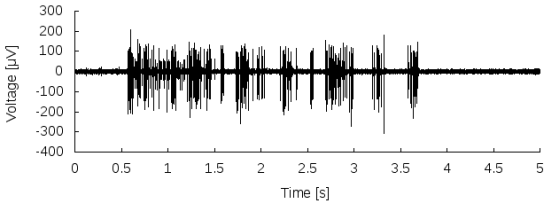

B2

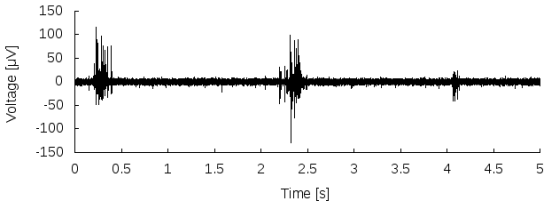

A3

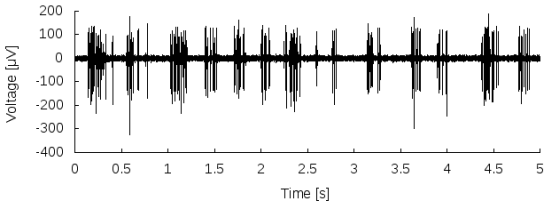

B3

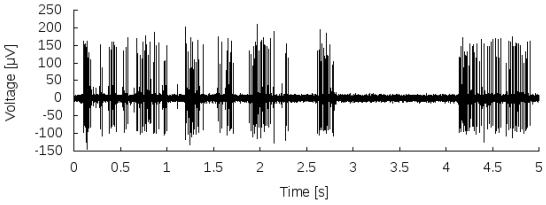

C1

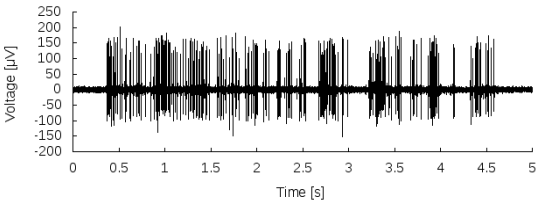

C2

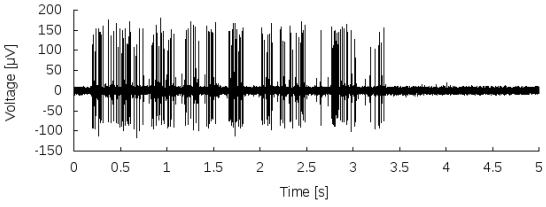

C3

Figure 4.1. Nine 5-s segments clipped from three single-channel signals recorded from the neurons cultured on MEAs. A1, A2, and A3 were clipped from signal A (100 days *in vitro*). B1, B2, B3 and C1, C2, C3 were clipped from signal B, signal C (both were 45 days *in vitro*), respectively. Bursts over the neuronal network and highly synchronized spiking were observed in these signals.

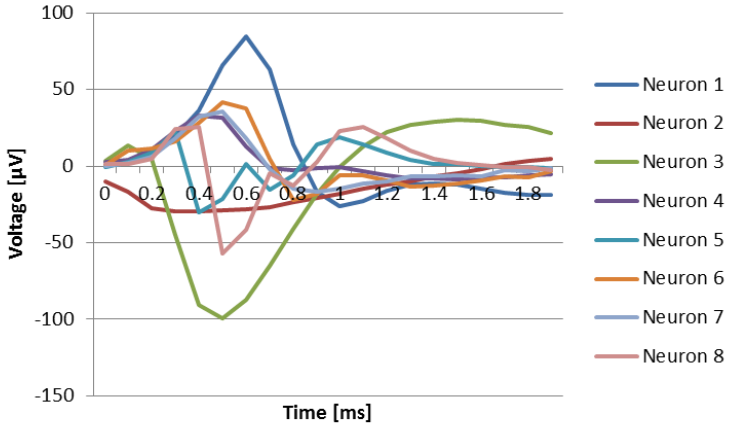

(a)

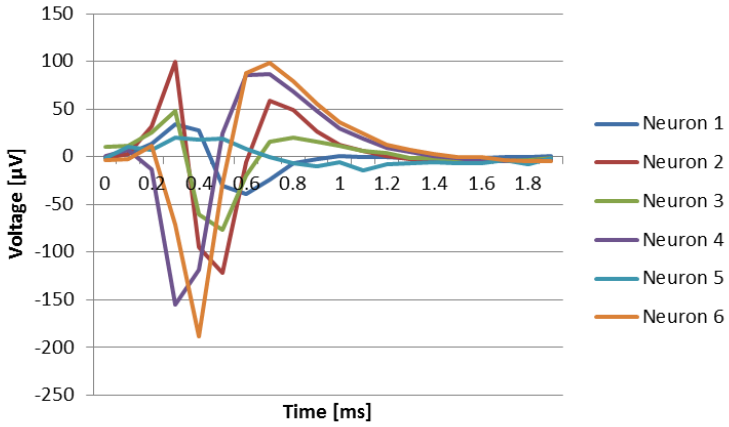

(b)

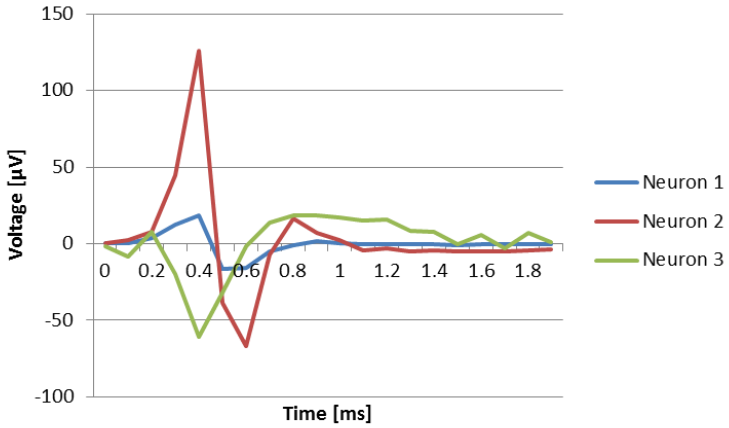

(c)

Figure 4.2. The spike templates extracted with DBSCAN clustering (a) from signal A. (b) from signal B. (c) from signal C.

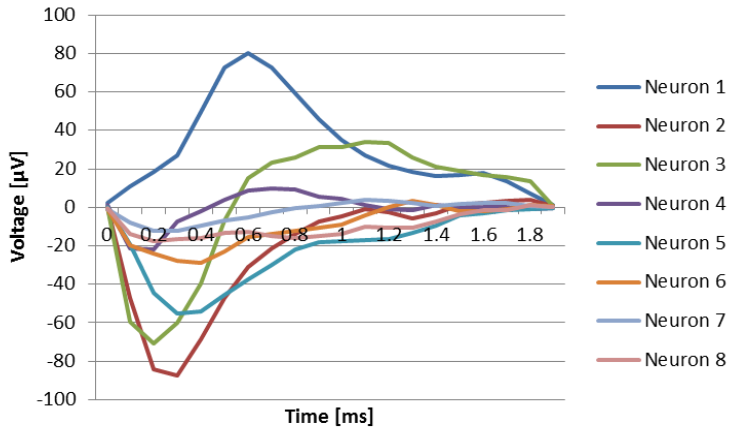

(a)

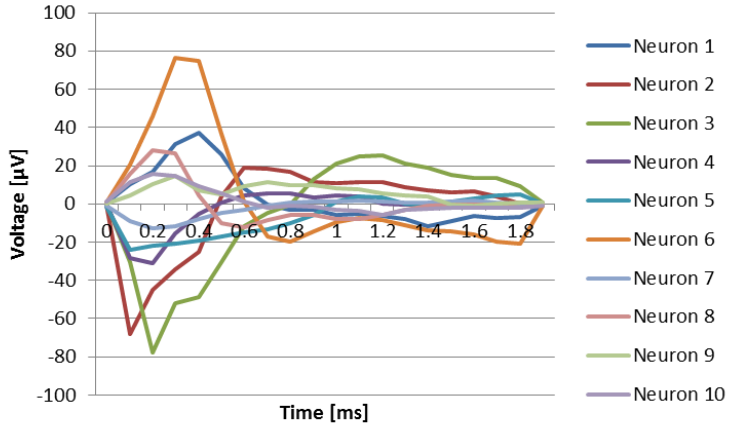

(b)

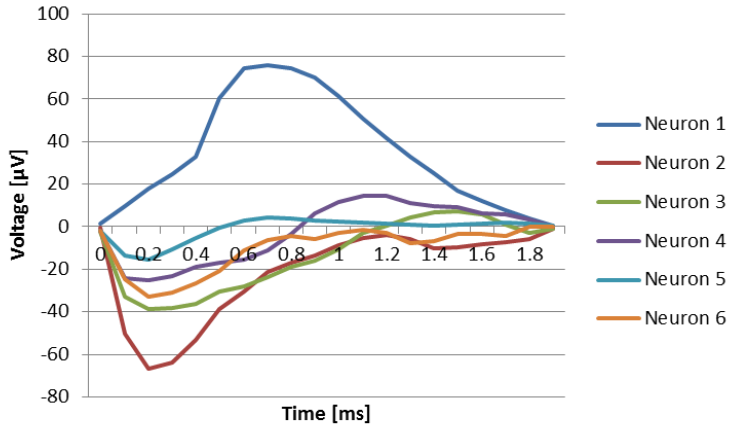

(c)

Figure 4.3. The spike templates extracted with our off-line method (a) from segment A1. (b) from segment A2. (c) from segment A3.

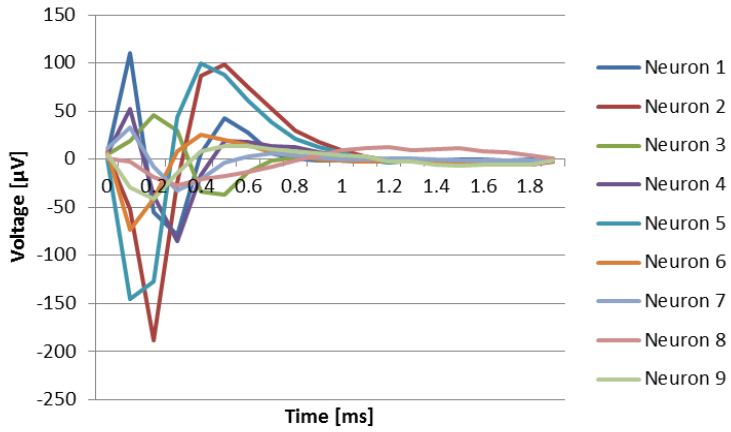

(a)

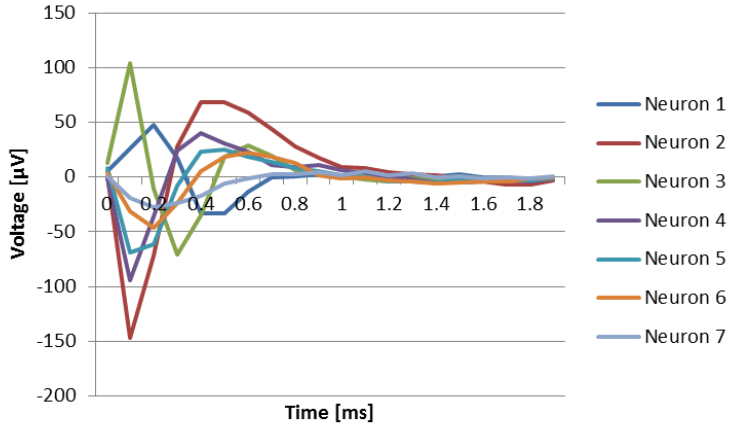

(b)

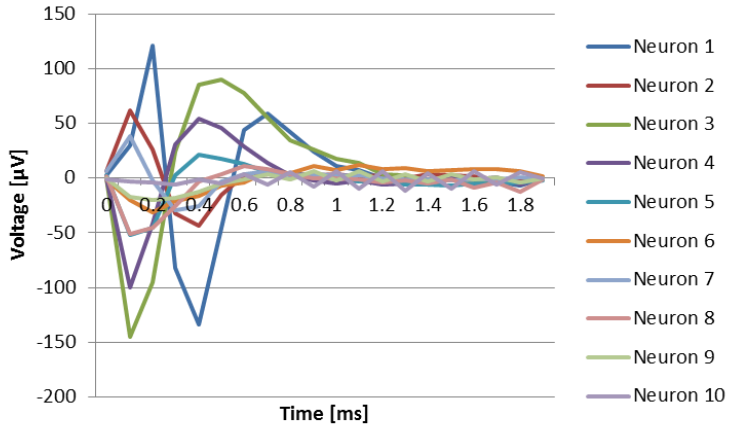

(c)

Figure 4.4. The spike templates extracted with our off-line method (a) from segment B1. (b) from segment B2. (c) from segment B3.

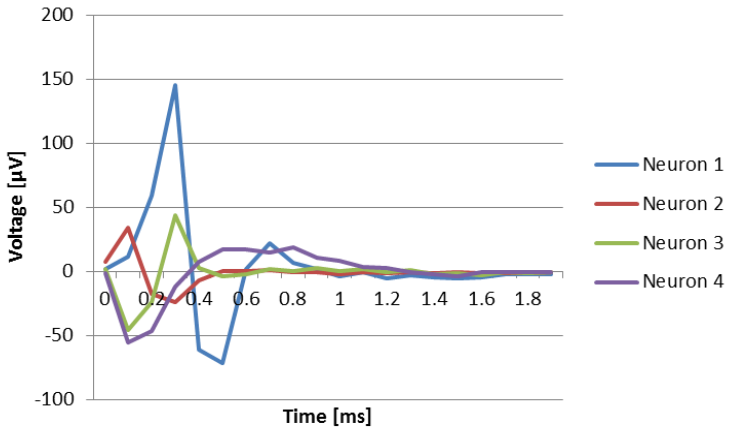

(a)

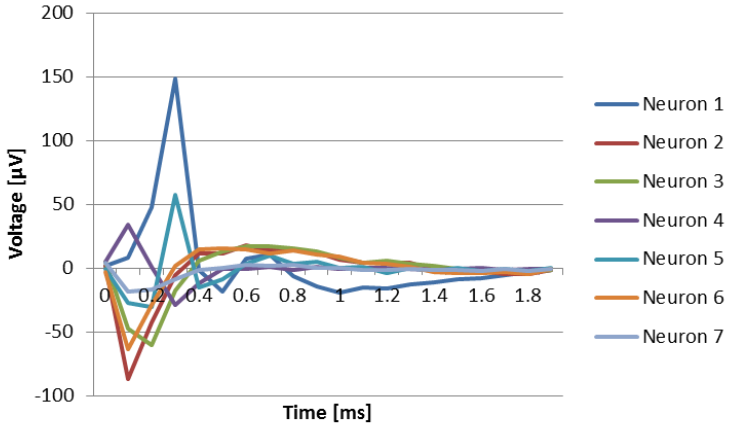

(b)

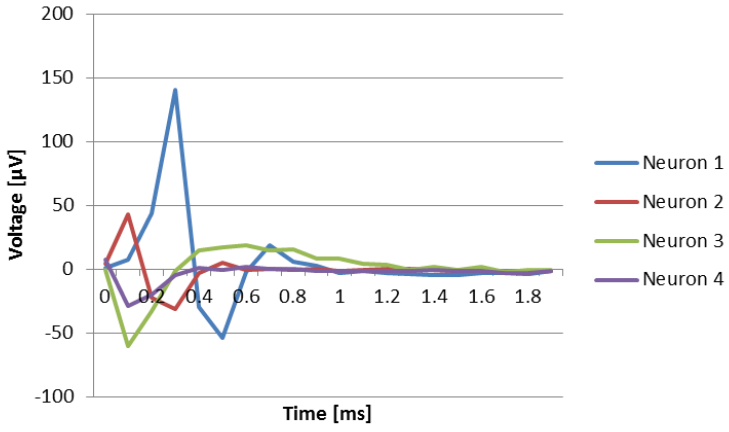

(c)

Figure 4.5. The spike templates extracted with our off-line method (a) from segment C1. (b) from segment C2. (c) from segment C3.

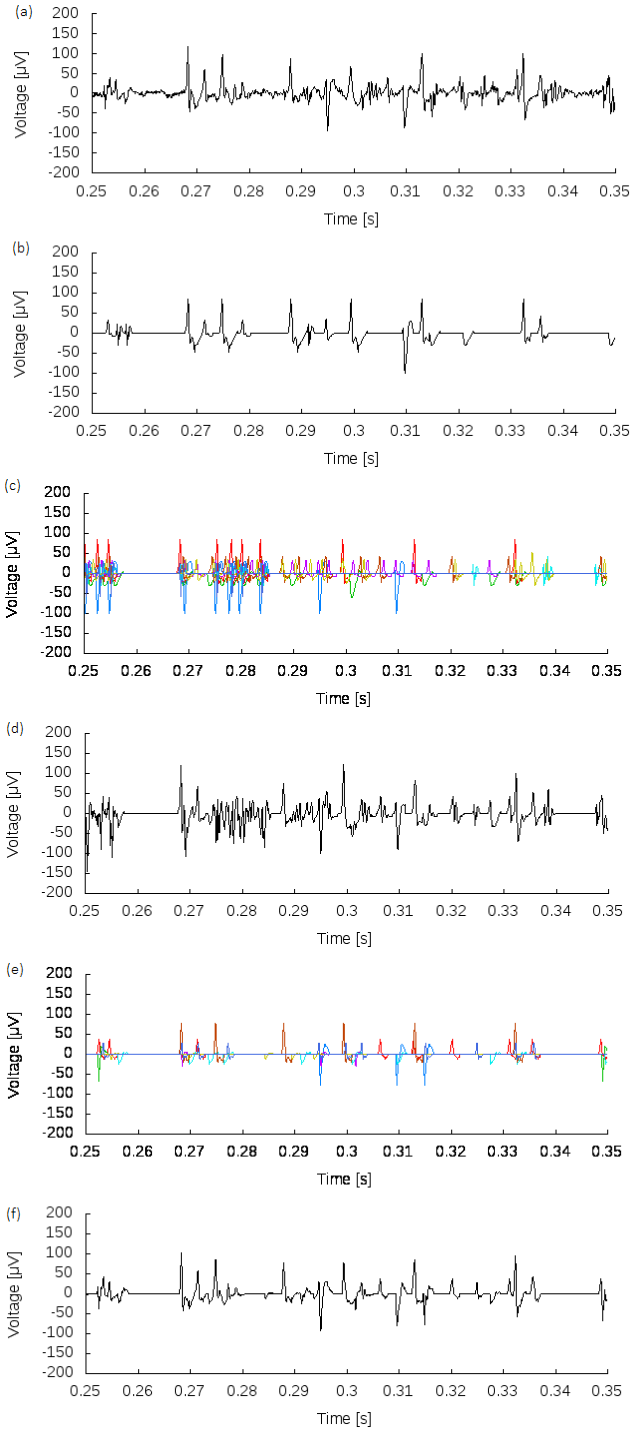

Figure 4.6. The estimated results for the part of the signal in segment A1. Note that different colors in spike trains mean different neurons. (a) The original signal. (b) The reconstructed signal for DB + TLMS. (c) The spike trains estimated with DB + BAYES. (d) The Reconstructed signal for DB + BAYES. (e) The spike trains estimated with BAYES+BAYES. (f) The reconstructed signal for BAYES + BAYES.

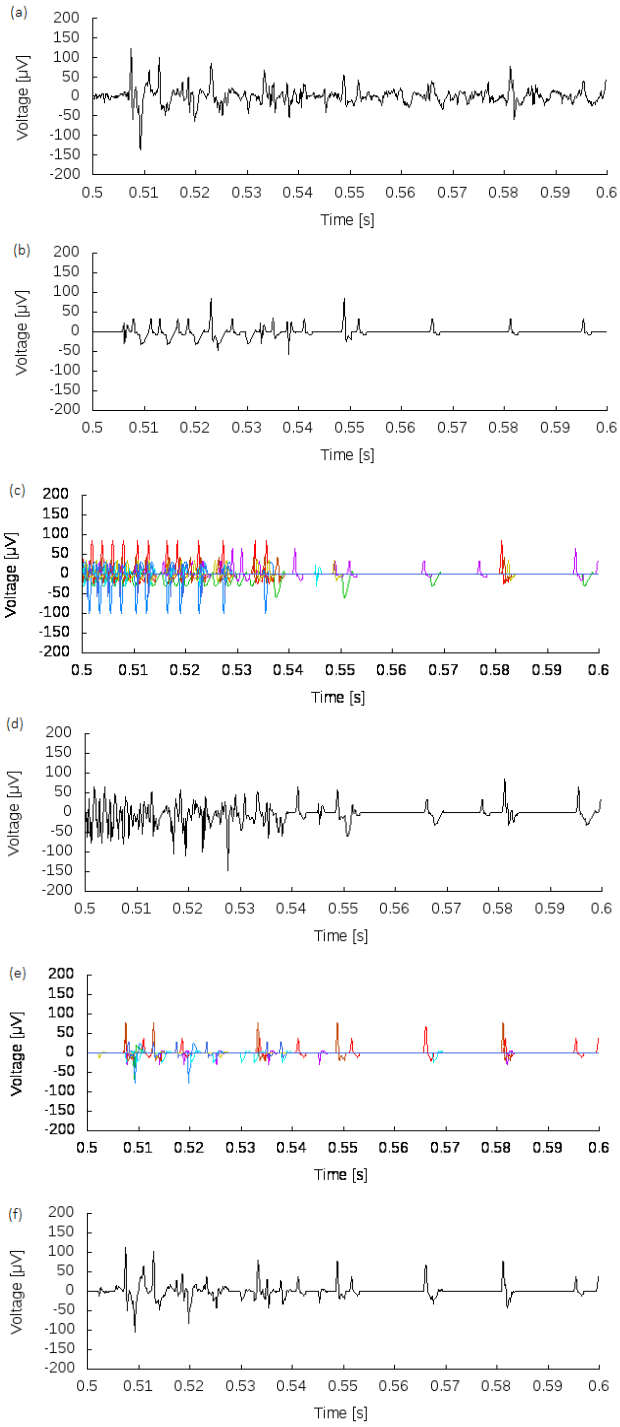

Figure 4.7. The estimated results for the part of the signal in segment A2. Note that different colors in spike trains mean different neurons. (a) The original signal. (b) The reconstructed signal for DB + TLMS. (c) The spike trains estimated with DB + BAYES. (d) The reconstructed signal for DB + BAYES. (e) The spike trains estimated with BAYES + BAYES. (f) The reconstructed signal for BAYES + BAYES.

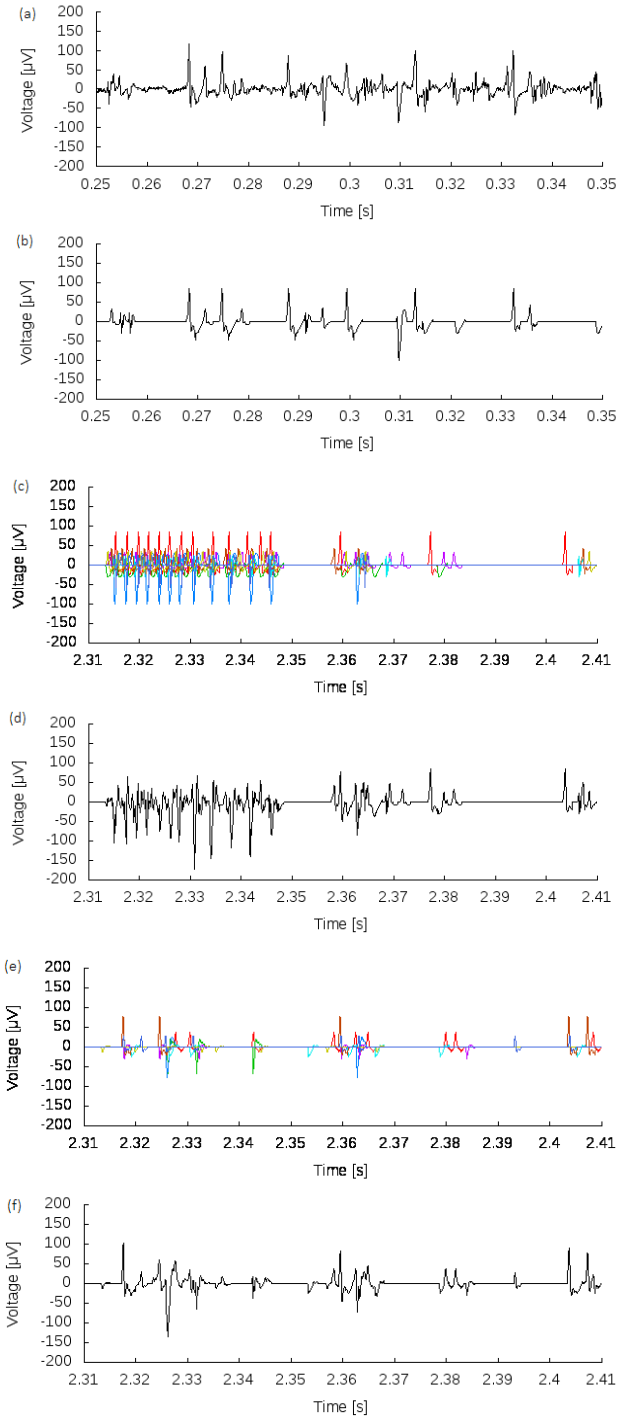

Figure 4.8. The estimated results for the part of the signal in segment A3. Note that different colors in spike trains mean different neurons. (a) The original signal. (b) The reconstructed signal for DB + TLMS. (c) The spike trains estimated with DB + BAYES. (d) The reconstructed signal for DB + BAYES. (e) The spike trains estimated with BAYES + BAYES. (f) The reconstructed signal for BAYES + BAYES.

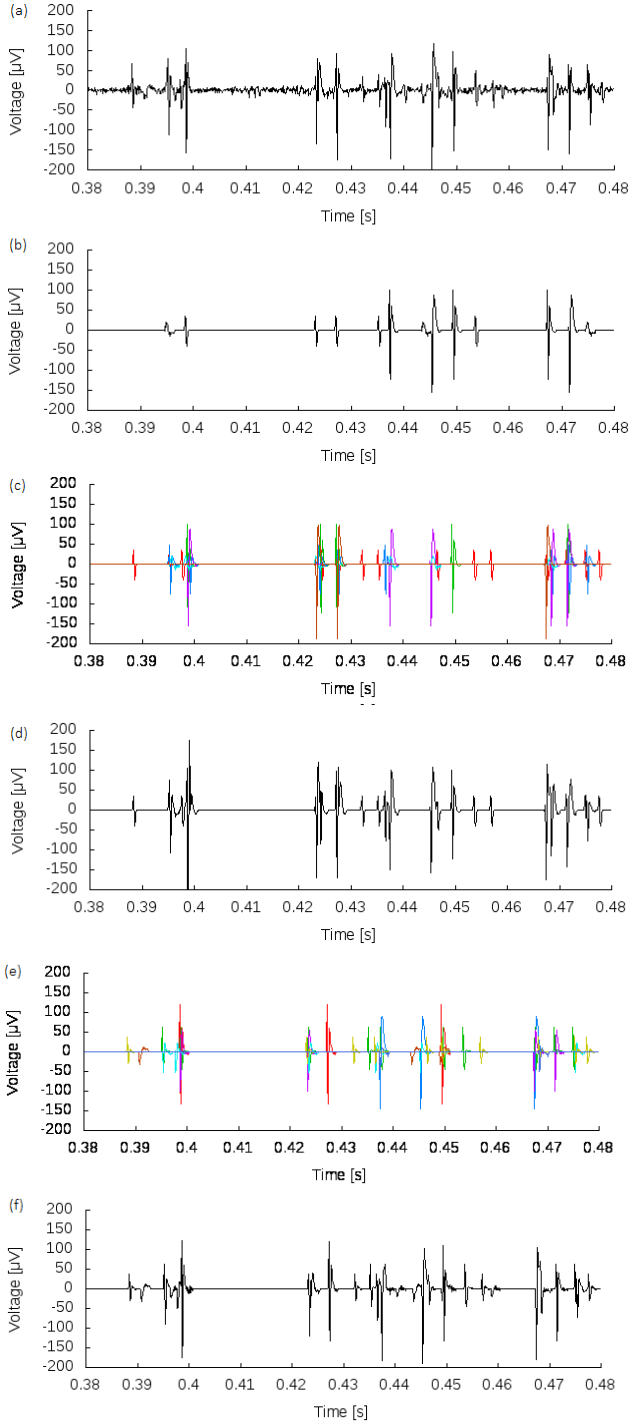

Figure 4.9. The estimated results for the part of the signal in segment B1. Note that different colors in spike trains mean different neurons. (a) The original signal. (b) The reconstructed signal for DB + TLMS. (c) The spike trains estimated with DB + BAYES. (d) The reconstructed signals for DB + BAYES. (e) The spike trains estimated with BAYES + BAYES. (f) The reconstructed signal for BAYES + BAYES.

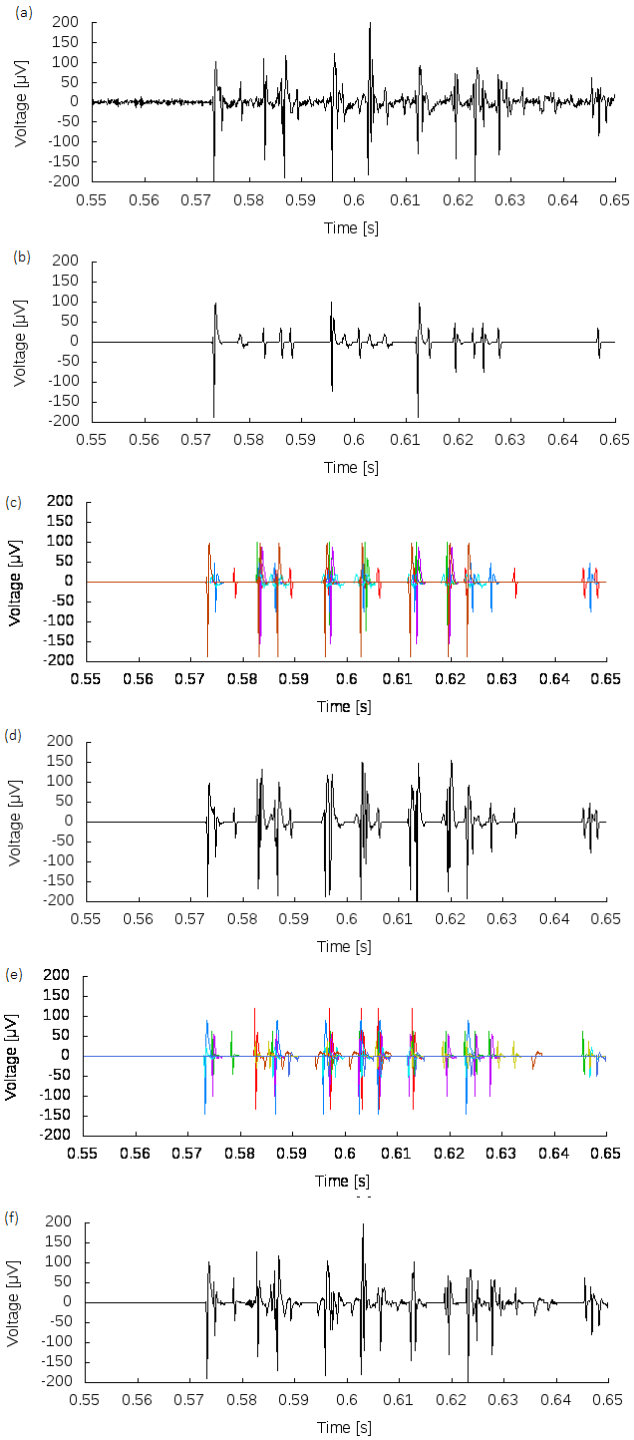

Figure 4.10. The estimated results for the part of the signal in segment B2. Note that different colors in spike trains mean different neurons. (a) The original signal. (b) The reconstructed signal for DB + TLMS. (c) The spike trains estimated with DB + BAYES. (d) The reconstructed signal for DB + BAYES. (e) The spike trains estimated with BAYES + BAYES. (f) The reconstructed signal for BAYES + BAYES.

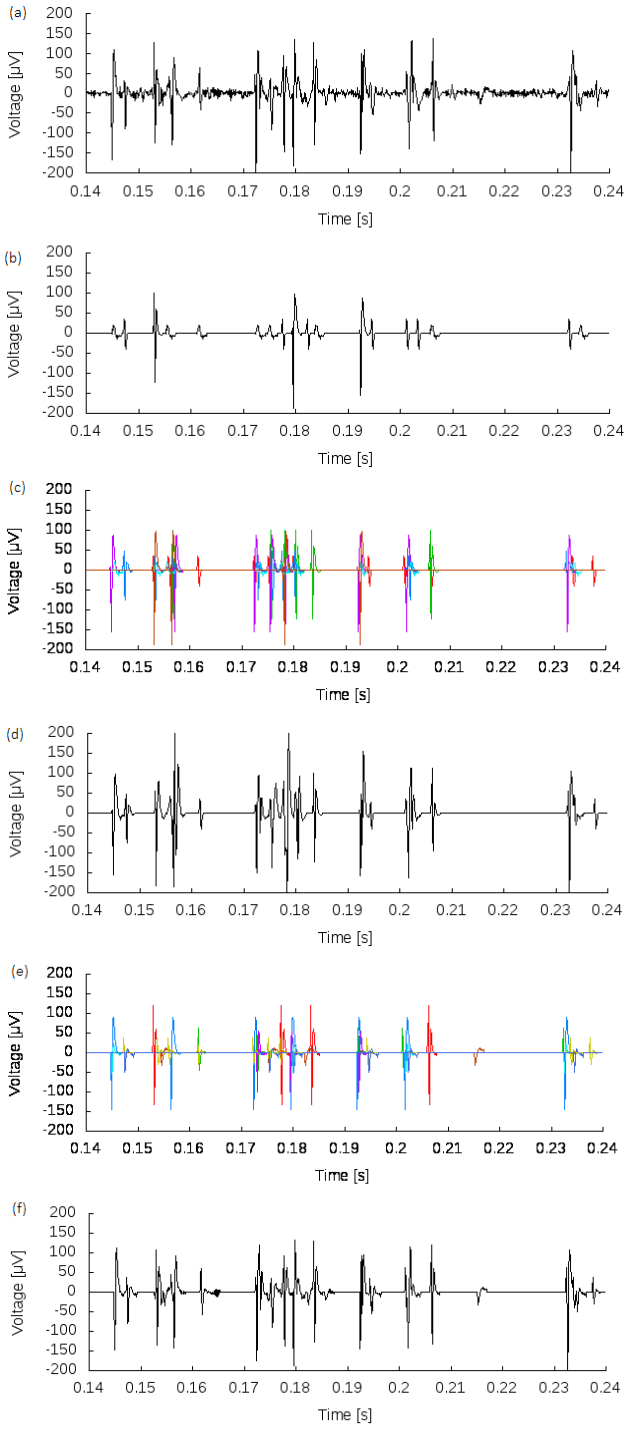

Figure 4. 11. The estimated results for the part of the signal in segment B3. Note that different colors in spike trains mean different neurons. (a) The original signal. (b) The reconstructed signal for DB + TLMS. (c) The spike trains estimated with DB + BAYES. (d) The reconstructed signal for DB + BAYES. (e) The spike trains estimated with BAYES + BAYES. (f) The reconstructed signal for BAYES + BAYES.

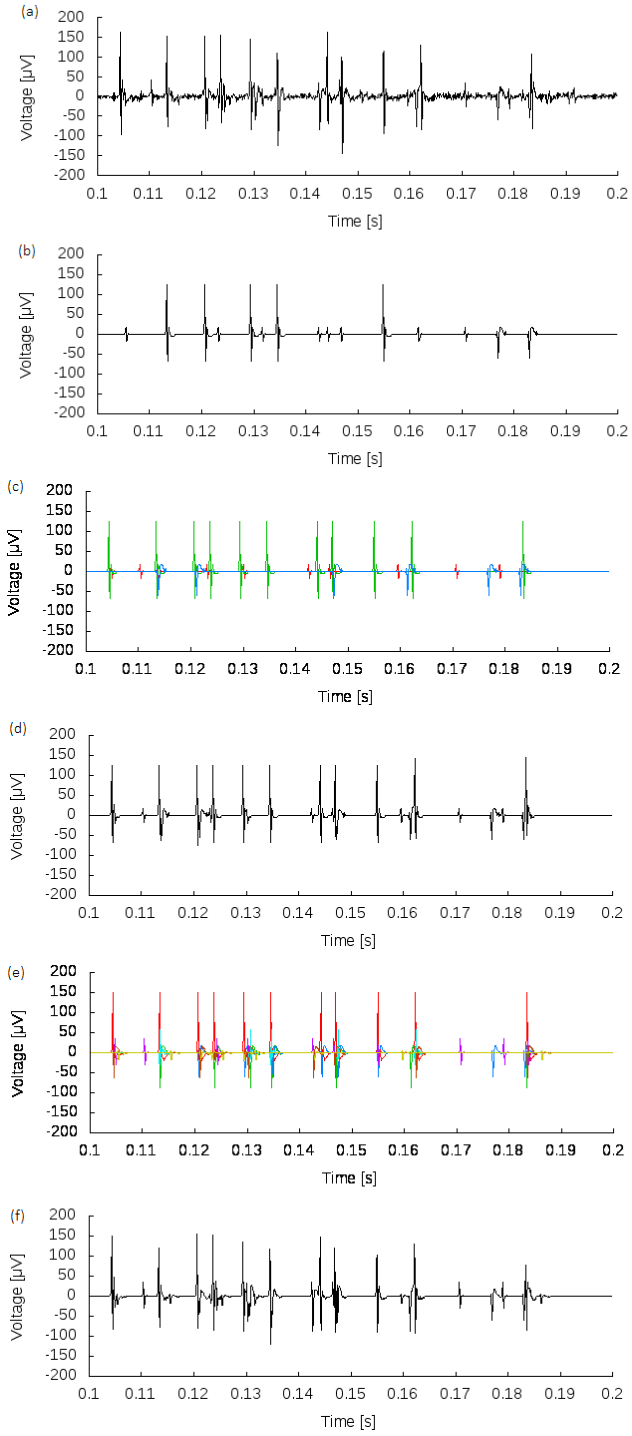

Figure 4.12. The estimated results for the part of the signal in segment C1. Note that different colors in spike trains mean different neurons. (a) The original signal. (b) The reconstructed signal for DB + TLMS. (c) The spike trains estimated with DB + BAYES. (d) The reconstructed signal for DB + BAYES. (e) The spike trains estimated with BAYES + BAYES. (f) The reconstructed signal for BAYES + BAYES.

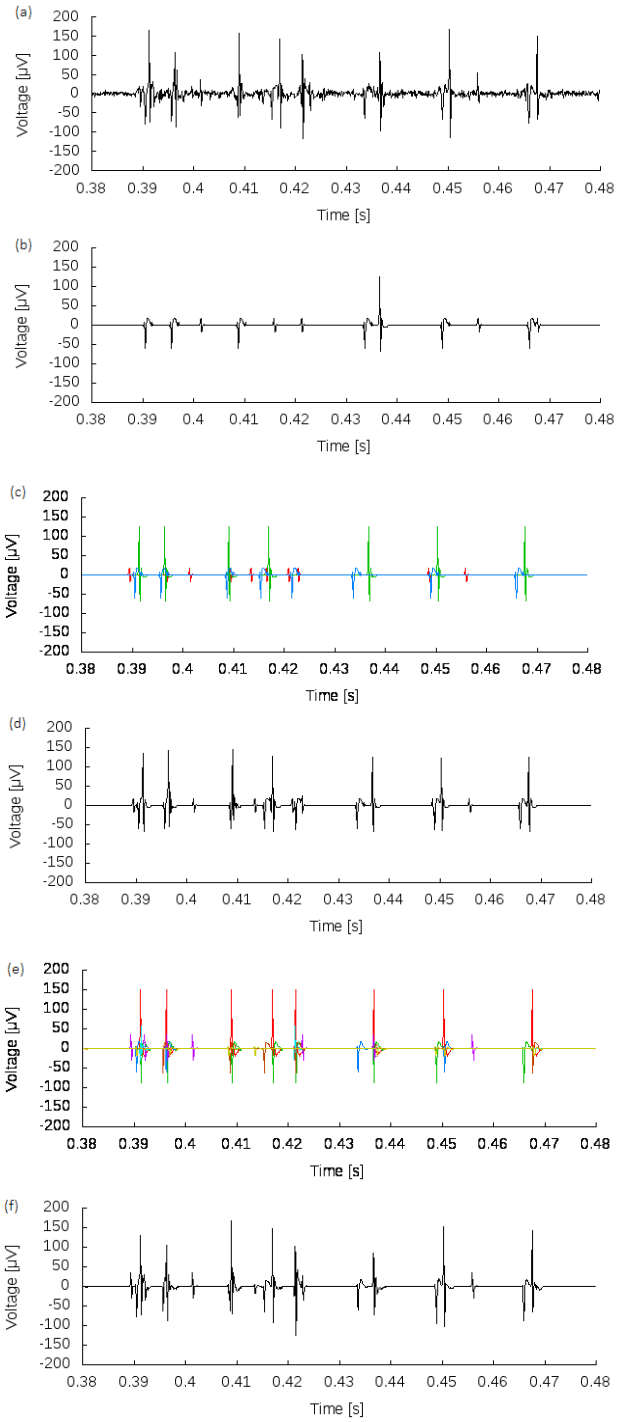

Figure 4.13. The estimated results for the part of the signal in segment C2. Note that different colors in spike trains mean different neurons. (a) The original signal. (b) The reconstructed signal for DB + TLMS. (c) The spike trains estimated with DB + BAYES. (d) The reconstructed signal for DB + BAYES. (e) The spike trains estimated with BAYES + BAYES. (f) The reconstructed signal for BAYES + BAYES.

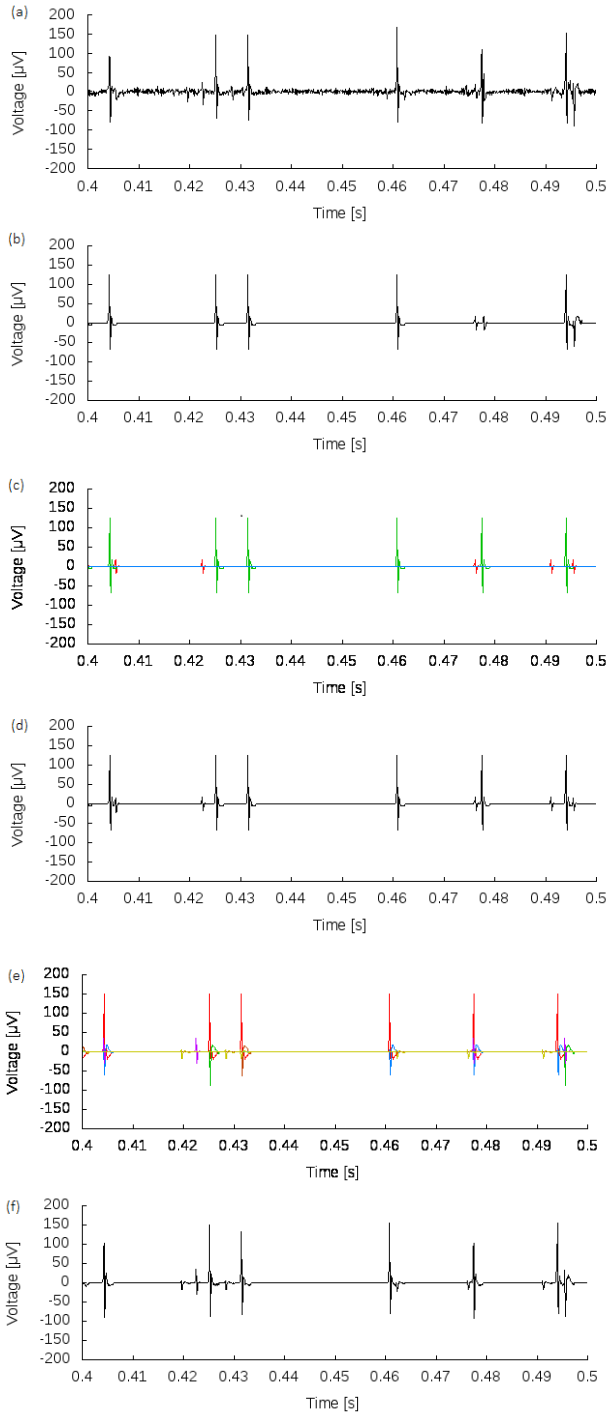

Figure 4.14. The estimated results for the part of the signal in segment C3. Note that different colors in spike trains mean different neurons. (a) The original signal. (b) The reconstructed signal for DB + TLMS. (c) The spike trains estimated with DB + BAYES. (d) The reconstructed signal for DB + BAYES. (e) The spike trains estimated with BAYES + BAYES. (f) The reconstructed signal for BAYES + BAYES.

BAYES + BAYES were generally more similar to the original signal than those of DB + TLMS, which suggested better estimation with our real-time method. However, the estimation of DB + BAYES showed a few obviously invalid results like those in Figures 4.6-4.8 (c) (d), and BAYES + BAYES performed better than DB + BAYES for the rest area.

4.4 Discussion

We obtained a larger number of spike templates with our off-line method than with the traditional approach with thresholding and DBSCAN clustering. Furthermore, spike detection with the spike templates created by our off-line method performed better than that with the spike templates created by the traditional approach. These results implied that the traditional approach missed necessary spike templates that can be detected with our off-line method, even though the traditional approach used the whole signal and our off-line method used only 5-s segments. This is one of the merits of our off-line methods to extract spike templates from the signals of short lengths containing bursts in contrast to clustering algorithms that usually require large data sets. This is realized by the decomposition of overlaps and the processing without thresholds in voltage. As we explained in Chapter 2, detection by thresholds often causes invalid results. It also affects the estimation by DB + TLMS in which many spikes are ignored or classified into invalid templates.

However, the number and shapes of the spike templates estimated by our off-line methods differed between segments from the same signal. One of the reasons for this was that some spike templates were not contained in the short segments clipped from the signal. If a neuron is not activated for several seconds, it is possible that the spike template for the neuron is not contained in a clipped signal. Nevertheless, applying our off-line method to the entire signal is difficult because of the high computational cost. One reasonable strategy to avoid the problem is the parallel computing of several short signals clipped with different timings and to compare the estimated results to determine the spike templates. This will reduce the misses of spike templates and the invalid estimations caused by overdecomposition and artifact noises.

The detection and sorting of the long signal should be processed by our real-time method presented in Chapter 2. However, as can be seen in the experimental results of DB + BAYES, invalid spike templates can cause obviously invalid estimations. This is one of the reasons to apply two methods in combination.

In the experiment, we observed that the spike templates of signal A had a longer duration than those of signal B and signal C. One possible reason for this is different electrophysiological properties of the recorded neurons. As we showed in Section 1.2, regular firing neurons usually have longer durations than fast spiking neurons. However, it is unlikely that all of the neurons recorded in an

electrode have the same properties. Another possibility is the inhomogeneity of the extracellular medium. The more days *in vitro*, the more developed are the cultured neuronal networks and glial cells. They produce an inhomogeneity of conductivity and permittivity in the extracellular environment, which provides low-pass filtering properties to the extracellular medium (Bedard et al., 2004). How the durations of spikes are changed should be investigated additionally because it is important to determine the appropriate duration of spikes with the setting parameters.

4.5 Summary of the chapter

In this chapter, we applied two methods in combination to various data and compared it with the traditional approach and the application without the combination. In the experimental results, we obtained a larger number of spike templates with our off-line methods than with the clustering approach, and using the spike templates extracted by our off-line methods improved the performance of the estimation with our real-time method. Additionally, our real-time method enabled applications to lengthy data, and this could not be realized with our off-line method. This implied that the two methods have a complementary relationship and that applying the two methods in combination is a reasonable approach.

Chapter 5
Conclusion

5.1 Summary of the thesis

The present thesis dealt with the detection and sorting of complexly overlapped neural spikes recorded with extracellular voltage recording. For this purpose, this thesis proposed two methods.

In Chapter 2, we proposed a fast sequential method that can robustly detect and sort arbitrarily overlapped spikes recorded with arbitrary types of electrodes. In our method, the probabilities of possible spike trains, including ones with overlapping spikes, are evaluated by a sequential Bayesian inference based on probabilistic models of spike-train generation and extracellular voltage recording. In order to reduce the high computational cost inherent in an exhaustive evaluation, candidates with low probabilities are considered to be impossible candidates and are censored at every sampling time in order to limit the number of candidates in the next evaluation. In addition, the data for a few sampling times ahead is considered and used to calculate the look-ahead probability, which results in more efficient calculation due to the faster elimination of candidates. These efforts reduce the computational time enough to enable real-time computation without impairing performance. We assessed the performance of our method with simulated neural signals and a real neural signal recorded from primary cortical neurons cultured on a multi-electrode array. Our results showed that our method could be applied in real-time and that the delay was less than 10 ms. The estimation accuracy was higher than that of a conventional spike sorting method, especially for signals with many overlapped spikes.

In Chapter 3, a method for the simultaneous estimation of spike templates and the timings of highly overlapped spikes was proposed. In our method, the inference based on HMM with the probabilistic penalty is efficiently calculated with the approximation. The performance of the method was assessed with simulated and real neural signals. The results showed that our method could appropriately decompose the simulated and real signals containing complexly overlapped spikes.

In Chapter 4, we discussed that The strong and weak points of these two methods were complementary and compared the performance of the two methods in combination with the

traditional approach and the application without the combination. In the experimental results, we obtained a larger number of spike templates with our off-line methods than with the clustering approach, and using the spike templates extracted by our off-line methods improved the performance of the estimation with our real-time method. Additionally, our real-time method enabled applications to lengthy data, and this could not be realized with our off-line method. This implied that the two methods have a complementary relationship and that applying the two methods in combination is a reasonable approach.

These methods showed good performance in spike detection and sorting under many complex overlaps. Our methods will help to obtain more accurate analyses of highly synchronized neural activity.

5.2 Future research directions

5.2.1 Real-time creation of spike templates and acceleration of computation

In Chapter 2, we discussed the real-time creation of spike templates in parallel with spike detection as one of a number of possible extensions. This can be realized by the reorganization of the learning procedure of the spike templates in Chapter 3 in a forward sequential manner and by adding it to the algorithm in Chapter 2. This cannot improve the computational time for the complete estimation of all of the spike templates and timings, but it can provide an incomplete and modest estimation in real-time before the complete estimation, which takes a long time.

5.2.2 Handling long-term changes of spike templates caused by drifts of electrodes

In both methods, long-term changes of spike templates caused by the drift of electrodes (Lewicki, 1998) still remain an unsolved issue. Modeling the changes with the Gauss-Markov process and estimating spike shapes as the hidden variable at every sampling time (Calabrese and Paninski, 2011) can solve the problem. However, implementing it would increase the computational cost.

5.2.3 Handling short-term changes of spike templates caused by bursting

The short-term changes in spike shapes caused by bursting (Lewicki, 1998) are also a remaining problem. This can be solved by adding a mathematical model about those changes to the proposed method. However, to the best of our knowledge, no simple model has been proposed for the changes in short-term spike shapes. Therefore, the properties of the change in spike shapes by bursting must be studied quantitatively in order to realize the improvement.

5.2.4 Handling artifact noises

Artifact noises that have spike-like transient shapes also have been a major problem in spike detection and sorting, especially in recordings from free-moving animals. Our methods have the potential to avoid detecting these noises. In our methods, the likelihood, which is the probability of the data given the model, is calculated every time. This factor shows how well the model explains the data, and therefore, data that exhibit a low likelihood are estimated to be outliers. This approach can be applied to not only the removal of artifact noises but also the detection of new spike templates.

5.2.5 Application to connectivity analysis

If we add the regression of other neurons' spike trains to the parameters of a neuron's inhomogenous Poisson process, we can take into account the correlations between the activities of neurons (Dayan et al., 2005). Of course, we can apply analysis methods after spike detection and sorting, but such a model could improve the estimation accuracy of spike detection and sorting if there are strong correlations between the spike trains of different neurons.

Acknowledgement

I gratefully appreciate the supervisors, Professor Kunihiko Mabuchi, Assistant Professor Takayuki Hoshino, Research Associate Osamu Fukayama. They provided me the fertile research environment and many advices about writing techniques.

I would also like to thank supervisors Professor Yasuhiko Jimbo at the Department of Human and Engineered Environmental Studies, Assistant Professor Hirokazu Takahashi at the Department of Information Physics and Computing, and Dr. Takafumi Suzuki at National Institute of Information and Communications Technology.

I express my gratitude for Dr. Yuzo Takayama at National Institute of Advanced Industrial Science and Technology, who gave me many technical advices about cell cultures and multi-electrode arrays. I could not record high-quality neural signals without his advices.

I would like to thank Ms. Mari Yasuhara, Ms. Yuko Kuboyama for helping me with the administrative chores.

References

Alabi AA, Tsien RW. Synaptic vesicle pools and dynamics. Cold Spring Harbor Perspectives in Biology 2012;4(8);1--18.

Bakkum DJ, Chao ZC, Potter SM. Spatio-temporal electrical stimuli shape behavior of an embodied cortical network in a goal-directed learning task. J Neural Eng 2008;5(3);310—23.

Baltz T, Herzog A, Voigt T. "Slow oscillating population activity in developing cortical networks: models and experimental results". J Neurophysiol 2011;106;1500—1514.

Bar-Gad I, Ritov Y, Vaadia E, Bergman H. Failure in identification of overlapping spikes from multiple neuron activity causes artificial correlations. J Neurosci Methods 2001;107(1-2);1—13.

B´edard C, Kröger H, Destexhe A. Modeling extracellular field potentials and the frequency-filtering properties of extracellular space. Biophys J 2004;86(3);1829–1842.

Bishop CM. Pattern Recognition and Machine Learning. Springer 2006.

Brewer GJ, Boehler MD, Pearson RA, DeMaris AA, Ide AN, Wheeler BC. Neuron network activity scales exponentially with synapse density. J Neural Eng 2009;6(1): 014001.

Brown EN, Kass RE, Mitra PP. Multiple neural spike train data analysis: state-of-the-art and future challenges. Nature Neurosci 2004;7(5); 456—61.

Buzsáki G, Anastassiou CA, Koch C. The origin of extracellular fields and currents — EEG, ECoG, LFP and spikes. Nat Rev Neurosci 2012;13(6);407--420.

Calabrese A, Paninski L. Kalman filter mixture model for spike sorting of non-stationary data. J Neurosci Methods 2011;196(1);159—69.

Campbell PK, Jones KE, Huber RJ, Horch KW, Normann RA. A silicon-based, three-dimensional neural interface: manufacturing processes for an intracortical electrode array. IEEE Trans Biomed Eng 1991;38(8);758—768.

Chiappalone M, Massobrio P, Martinoia S. Network plasticity in cortical assemblies. Euro J Neurosci 2008;28(1); 221–237.

Dayan P, Abbott LF. Theoretical Neuroscience: Computational and Mathematical Modeling of Neural Systems. The MIT Press 2005.

Donoghue JP. Connecting cortex to machines: recent advances in brain interfaces. Nature Neurosci 2002;5;1085—8.

Ester M, Kriegel HP, Sander J, Xu X. A density-based algorithm for discovering clusters in large spatial databases with noise. Proceedings of the 2nd International Conference on Knowledge Discovery and Data mining 1996;226—31.

Ferezou I, Bolea S, Petersen CCH. Visualizing the Cortical Representation of Whisker Touch: Voltage-Sensitive Dye Imaging in Freely Moving Mice. Neuron 2006;50(4);617–629.

Franke F, Natora M, Boucsein C, Munk MHJ, Obermayer K. An online spike detection and spike classification algorithm capable of instantaneous resolution of overlapping spikes. J Comput Neurosci 2010; 29(1);127—48.

Ge D, Carpentier EL, Farina D. Unsupervised Bayesian decomposition of multiunit EMG recordings using tabu search. IEEE Trans Biomed Eng 2010;57(3);561—71.

Gasthaus J, Wood F, Gorur D, Teh YW. Dependent Dirichlet process spike sorting, Adv Neur In 2008;497--504.

Gold C, Henze DA, Koch C, Buzsaki G. On the origin of the extracellular action potential waveform: a modeling study. J Neurophysiol 2006;95(5);3113-3128.

Heldman DA, Wang W, Chan SS, Moran DW. Local field potential spectral tuning in motor cortex during reaching, IEEE T Neur Sys Reh 2006;14(2);180--183.

Henze DA, Borhegyi Z, Csicsvari J, Mamiya A, Harris KD, Buzsaki G. Intracellular features predicted by extracellular recordings in the hippocampus in vivo. J Neurophysiol 2000; 84(1);390—400.

Herbst JA, Gammester S, Ferrero D, Hahnloser HR. Spike sorting with hidden Markov models. J Neurosci Methods 2008; 174(1);126—134.

Hines ML, Carnevale NT. The NEURON Simulation Environment. Neural Comput 1998;9(6);1179—1209.

Holt GR, Koch C. Electrical Interactions via the Extracellular Potential Near Cell Bodies. J Comput Neurosci 1999;6(2);169—184.

Hulata E, Segev R, Ben-Jacob E. A method for spike sorting and detection based on wavelet packets and Shannon's mutual information. J Neurosci methods 2002;117(1); 1—12.

Ito D, Tamate H, Nagayama M, Uchida T, Kudoh SN, Gohara K. Minimum neuron density for synchronized bursts in a rat cortical culture on multi-electrode arrays. Neuroscience 2010;171(1);50–61,.

Jenkner M, Tartagni M, Hierlemann A, Thewes R. Cell-Based CMOS Sensor and Actuator Arrays. IEEE J Solid-St Circ 2004;39(12);2431-2437.

Kandel E, Schwartz J, Jessell T. Principles of Neural Science, 4th edition. McGraw-Hill Medical 2000.

Kim S, McNames J. Automatic spike detection based on adaptive template matching for extracellular neural recordings. J Neurosci Methods 2007;165(2);165-74.

Lampl I, Reichova I, Ferster D. Synchronous membrane potential fluctuations in neurons of the cat visual cortex. Neuron 1999; 22(2); 361–374.

Lebedev MA, Carmena MJ, O'Doherty JE, Zacksenhouse M, Henriquez CS, Principe JC, Nicolelis MAL. Cortical ensemble adaptation to represent velocity of an artificial actuator controlled by a brain–machine interface. J Neurosci 2005;25(19);4681—93.

Lebedev MA, Nicolelis MAL. Brain-machine interfaces: past, present and future. Trends Neurosci 2006;29(9);536—46.

Lewicki, MS. Bayesian modeling and classification of neural signals. Neural Comput, 1994; 6(5);1005—30.

Lewicki MS. A review of methods for spike sorting: the detection and classification of neural action

potentials. Network-Comp Neural 1998;9(4);53—78.

Maccione A, Gandolfo M, Massobrio P, Novellino A, Martinoia S, Chiappalone M. A novel algorithm for precise identification of spikes in extracellularly recorded neuronal signals. J Neurosci Methods 2009;177(1); 241–249.

McGill CK. Optimal Resolution of Superimposed Action Potentials. IEEE Trans Biomed Eng 2002; 49(7);640—50.

Pelt JV, Wolters PS, Corner MA, Rutten WLC, Ramakers GJA. Long-Term Characterization of Firing Dynamics of Spontaneous Bursts in Cultured Neural Networks. IEEE T Bio-med Eng 2004;51(11).

Quian Quiroga R, Nadasdy Z, Ben-Shaul Y. Unsupervised spike detection and sorting with wavelets and superparamagnetic clustering. Neural Comput 2004;16;1661—87.

Rasmussen CE, The infinite Gaussian mixture model, Adv Neural Inf Processing Syst 2000;554—560.

Ruaro ME, Bonifazi P, Torre V. Toward the neurocomputer: Image processingand pattern recognition with neuronal cultures. IEEE T Bio-med Eng 2005; 52(3);371–383.

Sato T, Suzuki T, Mabuchi K. Fast automatic template matching for spike sorting based on Davies-Bouldin validation indices. Proceedings of the 29th International IEEE EMBS Conference; 2007;3200—3.

Schikorski T, Stevens CF. Quantitative Ultrastructural Analysis of Hippocampal Excitatory Synapses. J Neurosci 1997;17(15):5858-5867.

Shoham S, Fellows MR, Normann RA. Robust, automatic spike sorting using mixtures of multi-variate t-distribution. J Neurosci Methods 2003;127(2);111—122.

Shu Y, Hasenstaub A, Badoual M, Bal T, McCormick DA. Barrages of Synaptic Activity Control the Gain and Sensitivity of Cortical Neurons. J Neurosci 2003;23(32);10388—10401.

Slutzky MW, Jordan LR, Lindberg EW, Lindsay KE, Miller LE. Decoding the rat forelimb movement direction from epidural and intracortical field potentials. J Neural Eng 2011;8(3): 036013.

Squire LR, Bloom FE, Spitzer NC, Darwin B, Lac S, Ghosh A. Fundamental Neuroscience, Third

Edtion. Academic Press 2008.

Stashuk D. EMG signal decomposition: how can it be accomplished and used? J Electromyography Kinesiol 2001;11(3);151—73.

Stegenga J, Feber JL, Marani E, Rutten WLC. Analysis of Cultured Neuronal Networks Using Intraburst Firing Characteristics. IEEE T Bio-med Eng 2008;55(4).

Stuart G, Spruston N, Sakmann B, Häusser M. Action potential initiation and backpropagation in neurons of the mammalian CNS. Trends Neurosci 1997;20(3);125--131.

Suzuki I, Yasuda K. Detection of tetanus-induced effects in linearly lined-up micropatterned neuronal networks: Application of a multi-electrode array chip combined with agarose microstructures. Biochem Biophy Res Co 2007;356;470–475.

Takahashi N, Sasaki T, Usami A, Matsuki N, Ikegaya Y. Watching neuronal circuit dynamics through functional multineuron calcium imaging (fMCI), Neurosci Res 2007;58(3); 219--225.

Takahashi S, Sakurai Y. Real-time and automatic sorting of multi-neuronal activity for sub-millisecond interactions in vivo. Neuroscience 2003;134(1); 301—15.

Takahashi S, Anzai Y, Sakurai Y. Automatic sorting for multi-neuronal activity recorded with tetrodes in the presence of overlapping spikes. J Neurophysiol 2003a;89(4);2245—58.

Takahashi S, Anzai Y, Sakurai Y. A new approach to spike sorting for multi-neuronal activities recorded with a tetrode--how ICA can be practical、Neurosci Res 2003b;46(3);265—72.

Takekawa T, Isomura Y, Fukai T. Accurate spike sorting for multi-unit recordings, Euro J Neurosci 2010;31(2);263—272.

Thakur PH, Lu H, Hsioa SS, Johnson KO. Automated optimal detection and classification of neural action potentials in extra-cellular recordings. J Neurosci Methods 2007;162(1);64—376.

Vogelstein JT, Watson BO, Packer AM, Yuste R, Jedynak B, Paninski L. Spike inference from calcium imaging using sequential monte carlo methods. Biophys J 2009;97(2);636–655.

Wagenaar D, Pine J, Potter S. An extremely rich repertoire of bursting patterns during the development of cortical cultures. BMC Neurosci 2006;7(11); 1—18.

Wood F, Black MJ. A nonparametric Bayesian alternative to spike sorting, J Neurosci Methods 2008;173(1);1--12.

Yang X, Shamma S. A totally automated system for the detection and classification of neural spikes. IEEE Trans Biomed Eng 1988;35(10);806—10.

Zhang S, Jiang B, Zhu J, Zhang Q, Chen W, Zheng X, Zhao T. A study on combining local field potential and single unit activity for better neural decoding. Int J Imag Syst Tech 2011;21(2);165--172.

Publications

Journal Paper (English)

Tatsuya Haga, Osamu Fukayama, Yuzo Takayama, Takayuki Hoshino, Kunihiko Mabuchi, ``Efficient Sequential Bayesian Inference Method for Real-time Detection and Sorting of Overlapped Neural Spikes," Journal of Neuroscience Methods, Vol. 219, Issue 1, pp. 92-103, 2013.

Leo Miyashita, Yuzo Takayama, Tatsuya Haga, Takafumi Suzuki, Kunihiko Mabuchi, ``Effects of Electric Field Stimulation Timing on Calcium Dynamics of Cultured Cardiomyocytes," IEEJ Transactions on Electrical and Electronic Engineering, Vol. 8, No. S1, 2013

Yuzo Takayama, Naoki Kotake, Tatsuya Haga, Takafumi Suzuki, Kunihiko Mabuchi, ``Formation of one-way-structured cultured neuronal networks inmicrofluidic devices combining with micropatterning techniques," Journal of Bioscience and Bioengineering, Vol. 114, Issue 1, pp. 92–95, 2012

原著論文（日本語）

矢田祐一郎, 芳賀達也, 宮廻裕樹, 高山祐三, 深山理, 星野隆行, 満渕邦彦, ``シミュレーションを用いた神経回路網可塑的変化のテタヌス刺激位置依存性の検討," 電気学会論文誌 C（電子・情報・システム部門誌）, Vol. 133, No. 8, pp. 1485-1492, 2013.

International Conference

Tatsuya Haga, Yuzo Takayama, Kunihiko Mabuchi, “Estimation of Templates and Timings of Spikes in Extracellular Voltage Signals Containing Overlaps of the Arbitrary Number of Spikes”, 35th Annual International Conference of the IEEE Engineering in Medicine and Biology Society, Osaka, Japan, Jul. 2013 [Poster, Proceedings]

Yuichiro Yada, Tatsuya Haga, Osamu Fukayama, Takayuki Hoshino, Kunihiko Mabuchi, "Multiplicative-STDP Learning Rule shows Pathway Specificity", 35th Annual International Conference of the IEEE Engineering in Medicine and Biology Society, Osaka, Japan, Jul. 2013 [Poster]

Tatsuya Haga, Osamu Fukayama, Kunihiko Mabuchi, ``Template Estimation of Overlapped Neural Spikes Using Hidden Markov Model", The 44th ISCIE International Symposium on Stochastic Systems Theory and Its Applications Tokyo, Japan, November 1-2 ,2012 [Oral, Proceedings]

Tatsuya Haga, Osamu Fukayama, Takafumi Suzuki, Kunihiko Mabuchi, ``Estimation method of time-varying connection properties of neuronal network: assessments and application to in vitro data," 8th FENS Forum of Neuroscience, Barcelona, Spain, Jul. 2012 [Poster]

Tatsuya Haga, Yuzo Takayama, Osamu Fukayama, Takafumi Suzuki, Kunihiko Mabuchi,``Analysis of time-varying connection properties of cultured neuronal network under diverse conditions of electrical stimuli," MEA-meeting 2012, Reutlingen, Germany, Jul. 2012 [Poster, Proceedings]

Yuzo Takayama, Naoki Kotake, Tatsuya Haga, Takafumi Suzuki, Kunihiko Mabuchi,``Formation of One-way-propagated Cultured Neuronal Networks using Micro-fabrication and -fluidics Techniques," 8th FENS Forum of Neuroscience, Barcelona, Spain, Jul. 2012 [Poster]

Yuzo Takayama, Naoki Kotake, Tatsuya Haga, Takafumi Suzuki, Kunihiko Mabuchi,``Formation of One-way-propagated Cultured Neuronal Networks using Micro-fabrication and -fluidics Techniques," MEA-meeting 2012, Reutlingen, Germany, Jul. 2012 [Poster, Proceedings]

Yuzo Takayama, Naoki Kotake, Tatsuya Haga, Takafumi Suzuki, Kunihiko Mabuchi, “Microfabrication- and microfluidics-based patterning of cultured neuronal network”, 33rd Annual International Conference of the IEEE Engineering in Medicine and Biology Society, Boston, the United States, Sep. 2011 [Poster, Proceedings]

国内学会

芳賀　達也, 深山　理, 満渕 邦彦, "逐次ベイズ推定に基づくオーバーラップに頑健なリア

ルタイムスパイク検出法の多点電極アレイへの拡張", Neuro2013, Jun. 2013 [Poster]

高山 祐三, 小竹 直樹, 芳賀 達也, 鈴木 隆文, 満渕 邦彦, ``神経系形態形成における力学作用評価のためのマイクロ培養デバイス試作," 「細胞を創る」研究会 5.0, Nov. 2012 [Poster]

森田 明宏, 芳賀 達也, 深山 理, 鈴木 隆文, 満渕 邦彦, ``関節スティフネス表現を組み入れた物理モデルによる筋電義手関節角度推定," 平成２４年電気学会電子・情報・システム部門大会, Sep. 2012 [Oral, Proceedings]

芳賀 達也, 深山 理, 満渕 邦彦, ``再帰的ベイズ推定を用いた細胞外実計測信号からのオーバーラップした神経スパイクの実時間検出および分類," 第 27 回生体・生理工学シンポジウム, Sep. 2012 [Oral]

Tatsuya Haga, Osamu Fukayama, Takafumi Suzuki, Kunihiko Mabuchi, "Real-time template matching algorithm for overlapping spikes", The 21st Annual Conference of the Japanese Neural Network Society, pp. 140-141, Dec. 2011 [Poster]

Tatsuya Haga, Osamu Fukayama, Takafumi Suzuki, Kunihiko Mabuchi, ``The variance of connection property fluctuations in cultured neural networks according to conditions of electrical stimuli," Proceedings of The 26th Symposium on Biological and Physiological Engineering, Sep. 2011 [Oral]

芳賀 達也, 深山 理, 鈴木 隆文, 満渕 邦彦, ``事前知識を必要としないオンラインスパイクソーティング手法の開発," 生体医工学会第 50 回大会, Apr. 2011 [Poster]

芳賀 達也, 深山 理, 鈴木 隆文, 満渕 邦彦, ``Multi-Electrode-Array Dish 上の培養神経細胞ネットワークのリアルタイム結合推定・可視化システムの構築," 第 25 回生体・生理工学シンポジウム, Oct. 2010 [Oral]

藤原 正浩, 芳賀 達也, 鈴木 隆文, 満渕 邦彦, ``培養神経細胞を用いた刺激パターンの学習に関する研究ー高頻度電気刺激によるスパイク発火頻度の時間的分布変化を持ちいた学習ー," 第 25 回生体・生理工学シンポジウム, Oct. 2010 [Oral]

芳賀 達也, 深山 理, 鈴木 隆文, 満渕 邦彦, ``培養神経細胞ネットワークの電気刺激下におけるシナプス結合強度変化の動的推定," 生体医工学会第 49 回大会, Jun. 2010 [Poster]

芳賀 達也, 深山 理, 鈴木 隆文, 満渕 邦彦, ``発火確率モデルを用いた無入力条件下での培養神経細胞ネットワークの結合強度解析," 電気学会医用・生体工学研究会, No. 25, Mar. 2010 [Oral]

芳賀 達也, 深山 理, 鈴木 隆文, 満渕 邦彦, ``発火確率モデルを用いた神経細胞ネットワーク構造の動的推定法 -培養神経細胞に対する試験的解析," 神経回路学会「脳と心のメカニズム」 第 10 回冬のワークショップ, Jan. 2010 [Poster]

Appendix A
Cell Culture and recording methods

Cortical tissues were isolated from Wister rat embryos (on embryonic day 18) and dissociated by digestion with 0.1% trypsin-EDTA (Gibco Inc.) in calcium- and magnesium-free Hanks' balanced salt solution (Sigma Diagnosis Inc.). The dissociated cells were plated on MEA substrates coated with polyethylenimine at a density of 1.7×10^3 cells/mm^2. The MEA substrate used in the experiment was MED545A (Alpha MED Scientific Inc.). It had 8×8 indium–tin–oxide (ITO) electrodes coated with platinum black and 4 electrodes for reference. Each electrode was 50μm square and the distance between electrodes was 450μm. The culture medium consisted of Dulbecco's modified eagle's medium (Gibco Inc.), 5% fetal bovine serum, 5% horse serum, 2.5μm/mL insulin and 5-40 U/mL penicillin streptomycin. The cultures were maintained in an incubator with 5% CO_2 at 37 ºC and in a water-saturated atmosphere. Half of the medium was exchanged twice a week.

Difference of potential between each recording electrode and reference electrodes were measured and 64-channel signals were obtained. The signals were amplified 1000 times and filtered to cut frequencies under 100 Hz with the MED 64 Amplifier (Alpha MED Scientific Inc.). Amplified signals were recorded on PC after conversion to digital data (2 byte integer) within the range of ± 0.5V by using two 32-channel A/D boards (PCI6071E, National Instruments Inc.) and comedi (A/D driver for Linux). We recorded signals for 10 minutes from 2 samples after 100 days *in vitro* and 45 days *in vitro* respectively. We used one or two channels chosen from 64 channels. The sampling rate was 10 kHz. The block diagram of the recording system is shown in Fig. A. 1 and setup is shown in Fig. A. 2.

The experiment was done in accordance with the University of Tokyo's guidelines regarding animal research.

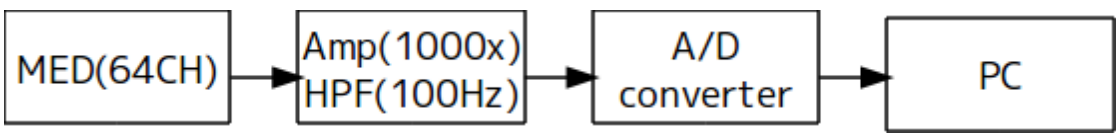

Figure A. 1. Block diagram of the recording system.

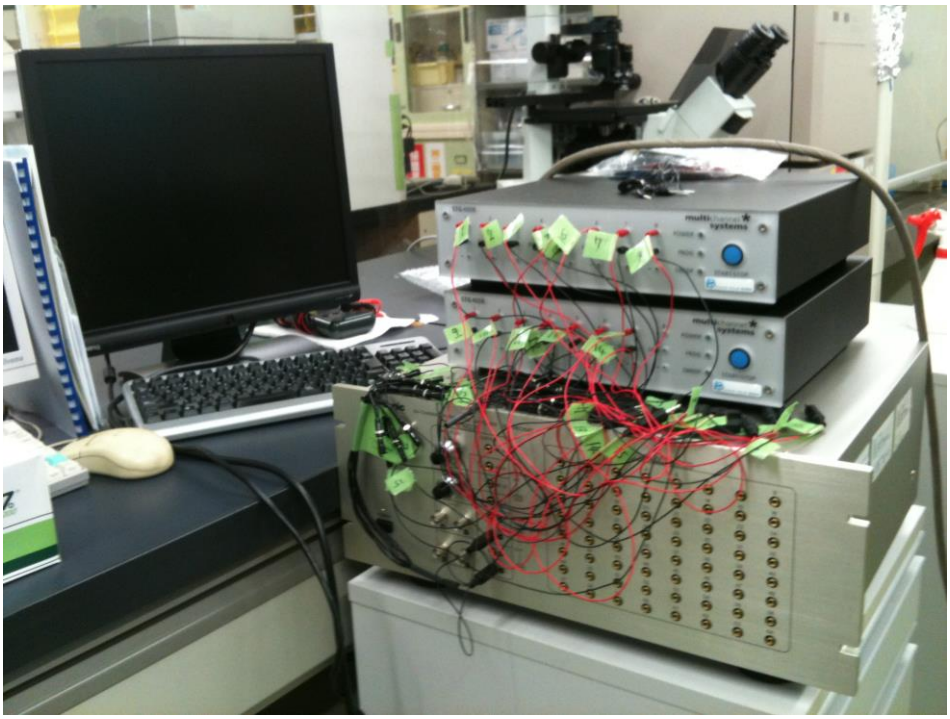

Figure A. 2. Setup of the recording system.

Appendix B
Derivation of equations to update parameters in M-step

In this appendix, model parameters that maximizes Q function under given probabilistic distributions of hidden variables $\gamma(z_t)$, $\xi(z_{t-1}, z_t)$ in Chapter 3 is derived. Q function is

$$\begin{aligned} Q(\theta) &= \sum_{z_{1:T}} p(z_{1:T}|y_{1:T},\theta^{old}) \log p(y_{1:T},z_{1:T}|\theta^{new}) \\ &= \log p(z_1) + \sum_{t=2}^{T} \sum_{z_t,z_{t-1}} \xi(z_t,z_{t-1}) \log p(z_t|z_{t-1},\theta) \\ &+ \sum_{t=1}^{T} \sum_{z_t} \gamma(z_t) \log p(y_t|z_t,\theta) \end{aligned} \tag{B.1}$$

We define Q_π and $Q_{\mu,\sigma}$ as

$$\begin{aligned} Q_\pi &= \sum_{t=2}^{T} \sum_{z_t} \xi(z_t,z_{t-1}) \log p(z_t|z_{t-1},\theta) \\ &= \sum_{t=1}^{T} \left\{ \sum_{z_{t-1}} \sum_{z_t\, s.t. z_t \in C_z \wedge z_t[1]=0} \xi(z_t,z_{t-1}) \log \left\{ 1 - \phi^{F(z_t)} (1 - \pi_0 - \sum_{k \in C_r} \pi_k) \right\} \right. \\ &\left. + \sum_{z_{t-1}} \sum_{z_t\, s.t.\, z_t \in C_z \wedge z_t[1] \in C_f} \xi(z_t,z_{t-1}) \left(\log \pi_{z_t[1]} + F(z_t) \log \phi \right) \right\} \end{aligned} \tag{B.2}$$

$$Q_{\mu,\sigma} = \sum_{t=1}^{T}\sum_{z_t}\gamma(z_t)\log p(y_t|z_t,\theta)$$

$$= \sum_{t=1}^{T}\sum_{z_t}\gamma(z_t)\left\{-\frac{1}{2}\log(2\pi) - \frac{1}{2}\log(\sigma) - \frac{\left(y_t - \sum_{\tau=1}^{M+1}\mu_{z_t[\tau],\tau}\right)^2}{2\sigma}\right\} \tag{B.3}$$

and derive π that maximizes Q_π and μ, σ that maximizes $Q_{\mu,\sigma}$ respectively. Q_π is maximized by Lagrange's method of undetermined multipliers.

$$L_\pi = Q_\pi - \lambda\left(\sum_{k=0}^{N}\pi_k - 1\right) \tag{B.4}$$

$$\frac{\partial L_\pi}{\partial \lambda} = \sum_{k=0}^{N}\pi_k - 1 = 0 \tag{B.5}$$

$$\frac{\partial L_\pi}{\partial \pi_0} = \sum_{t=1}^{T}\sum_{z_{t-1}}\sum_{z_t\ s.t.z_t\in C_z\wedge z_t[1]=0}\xi(z_t,z_{t-1})\frac{\phi^{F(z_t)}}{1-\phi^{F(z_t)}\left(1-\pi_0-\sum_{k\in C_r}\pi_k\right)} - \lambda = 0 \tag{B.6}$$

$$\Leftrightarrow \frac{1}{T}\sum_{t=1}^{T}\sum_{z_{t-1}}\sum_{z_t\ s.t.z_t\in C_z\wedge z_t[1]=0\wedge F(z_t)=0}\xi(z_t,z_{t-1})\ \frac{1}{\pi_0+\sum_{k\in C_r}\pi_k} +$$

$$\frac{1}{T}\sum_{t=1}^{T}\sum_{z_{t-1}}\sum_{z_t\ s.t.z_t\in C_z\wedge z_t[1]=0\wedge F(z_t)=1}\xi(z_t,z_{t-1})\ \frac{\phi}{1-\phi\left(1-\pi_0-\sum_{k\in C_r}\pi_k\right)} - \frac{1}{T}\lambda = 0 \tag{B.7}$$

$$\Leftrightarrow \frac{q_0}{\pi_0} + \frac{q_1\phi}{1-\phi\left(1-\pi_0-\sum_{k\in C_r}\pi_k\right)} - \frac{1}{T}\lambda = 0 \tag{B.8}$$

$$\frac{\partial L_\pi}{\partial \pi_k} = \frac{1}{\pi_k}\sum_{t=1}^{T}\sum_{z_{t-1}}\sum_{z_t\ s.t\ .z_t\in C_z\wedge z_t[1]=k\in C_f}\xi(z_t,z_{t-1}) - \lambda = 0\ ,\ k\neq 0 \tag{B.9}$$

$$\Leftrightarrow \frac{1}{T}\lambda\,\pi_k = r_k \tag{B.10}$$

Here we defined q_0, q_1, r_k as shown below.

$$q_0 = \frac{1}{T}\sum_{t=1}^{T}\sum_{z_{t-1}}\sum_{z_t\ s.t.\ z_t \in C_z \wedge z_t[1]=0 \wedge F(z_t)=0} \xi(z_t, z_{t-1}) \ , \tag{B.11}$$

$$q_1 = \frac{1}{T}\sum_{t=1}^{T}\sum_{z_{t-1}}\sum_{z_t\ s.t.\ z_t \in C_z \wedge z_t[1]=0 \wedge F(z_t)=1} \xi(z_t, z_{t-1}) \ , \tag{B.12}$$

$$r_k = \sum_{t=1}^{T}\sum_{z_{t-1}}\sum_{z_t\ s.t.\ z_t \in C_z \wedge z_t[1]=k \in C_f} \xi(z_t, z_{t-1}) \tag{B.13}$$

By summing π_k for $1 \leq k \leq N$ and using $\sum_{k=1}^{N} \pi_k = 1 - \pi_0$ we can derive

$$\lambda = \frac{T}{1-\pi_0}\sum_{k=1}^{N} r_k \tag{B.14}$$

and

$$\pi_k = \frac{T r_k}{\lambda} = \frac{r_k}{\sum_{k=1}^{N} r_k}(1-\pi_0) \tag{B.15}$$

.

By substituting this formula to $\frac{q_0}{\pi_0} + \frac{q_1 \phi}{1-\phi(1-\pi_0-\sum_{k\in C_r}\pi_k)} - \frac{1}{T}\lambda = 0$ and by using

$$q_0 + q_1 + \sum_{k=1}^{N} r_k = \frac{1}{T}\sum_{t=1}^{T}\sum_{z_{t-1},z_t} \xi(z_t, z_{t-1}) = 1 \tag{B.16}$$

$$\frac{q_0}{\pi_0} + \frac{q_1 \phi}{1-\phi\left(1-\frac{\sum_{k\in C_r} r_k}{\sum_{k=1}^{N} r_k}\right)(1-\pi_0)} - \frac{1}{1-\pi_0}\sum_{k=1}^{N} r_k = 0 \tag{B.17}$$

$$\Leftrightarrow \phi\pi_0^2 - (\phi(q_0+1) + q_1 - 1)\pi_0 - q_0(1-\phi) = 0 \tag{B.18}$$

, the solution of this quadratic equation is derived as

$$\pi_0 = \frac{\phi(q_0+1) + q_1 - 1 \pm \sqrt{(\phi(q_0+1) + q_1 - 1)^2 + 4q_0\phi(1-\phi)}}{2\phi} \tag{B.19}$$

.

Under constraints $0 < \beta < 1$ and $0 \leq q_0 \leq 1$,

$$4q_0\phi(1-\phi) > 0 \tag{B.20}$$

$$\frac{\phi(q_0+1) + q_1 - 1 - \sqrt{(\phi(q_0+1) + q_1 - 1)^2 + 4q_0\phi(1-\phi)}}{2\phi} < 0 \tag{B.21}$$

Therefore π_0 which maximizes Q_π in $0 \leq \pi_0 \leq 1$ is specified.

$$\pi_0 = \frac{\phi(q_0+1) + q_1 - 1 + \sqrt{(\phi(q_0+1) + q_1 - 1)^2 + 4q_0\phi(1-\phi)}}{2\phi} \tag{B.22}$$

π_k can be calculated from π_0 using the equation (B.15).

Next, we derive $\mu_{n,\tau}$ that maximizes $Q_{\mu,\sigma}$.

$$\frac{\partial Q_{\mu,\sigma}}{\partial \mu_{n,\tau}} = \sum_{t=1}^{T} \sum_{z_t \, s.t. z_t[\tau]=n} \gamma(z_t) \frac{\left(y_t - \sum_{\tau=1}^{M+1} \mu_{z_t[\tau],\tau}\right)}{\sigma} = 0 \;, 1 \le n \le N, 1 \le \tau \le M \tag{B.23}$$

$$\Leftrightarrow \sum_{t=1}^{T} \sum_{z_t \, s.t. z_t[\tau]=n} \gamma(z_t) \sum_{\tau=1}^{M+1} \mu_{z_t[\tau],\tau} = \sum_{t=1}^{T} y_t \sum_{z_t \, s.t. z_t[\tau]=n} \gamma(z_t) \tag{B.24}$$

$$\Leftrightarrow \mu_{n,\tau} \sum_{t=1}^{T} \sum_{z_t \, s.t. z_t[\tau]=n} \gamma(z_t) + \sum_{\tau \neq \tau'} \sum_{n'=1}^{N} \mu_{n',\tau} \sum_{t=1}^{T} \sum_{z_t \, s.t. z_t[\tau]=n, z_t[\tau']=n'} \gamma(z_t) = \sum_{t=1}^{T} y_t \sum_{z_t \, s.t. z_t[\tau]=n} \gamma(z_t) \tag{B.25}$$

Matrix representation of this equation is

$$\mathbf{A}\boldsymbol{\mu} = \mathbf{b} \tag{B.26}$$

$$\boldsymbol{\mu} = \{\mu_{1,1}, \mu_{1,2}, \dots, \mu_{1,M+1}, \mu_{2,1}, \mu_{2,2}, \dots, \mu_{N,M+1}\} \tag{B.27}$$

$$\mathrm{A}[\tau + (n-1)(M+1), \tau' + (n'-1)(M+1)] = \begin{cases} \sum_{t=1}^{T} \sum_{z_t \, s.t. z_t[\tau]=n} \gamma(z_t) \;, \tau = \tau', n = n' \\ 0, \tau = \tau', n \neq n' \\ \sum_{t=1}^{T} \sum_{z_t \, s.t. z_t[\tau]=n, z_t[\tau']=n'} \gamma(z_t) \;, \tau \neq \tau' \end{cases} \tag{B.28}$$

$$\mathrm{b}^{(\tau+(n-1)(M+1))} = \sum_{t=1}^{T} y_t \sum_{z_t \, s.t. z_t[\tau]=n} \gamma(z_t) \tag{B.29}$$

$\boldsymbol{\mu}$ can be obtained by solving equation (B.26).

σ that maximizes $Q_{\mu,\sigma}$ under given $\mu_{n,\tau}$ is

$$\frac{\partial Q_{\mu,\sigma}}{\partial \sigma} = \sum_{t=1}^{T} \sum_{z_t} \gamma(z_t) \left\{ -\frac{1}{2\sigma} + \frac{\left(y_t - \sum_{\tau=1}^{M+1} \mu_{z_t[\tau],\tau}\right)^2}{2\sigma^2} \right\} = 0 \tag{B.30}$$

$$\Leftrightarrow \sigma = \frac{1}{T} \sum_{t=1}^{T} \sum_{z_t} \gamma(z_t) \left(y_t - \sum_{\tau=1}^{M+1} \mu_{z_t[\tau],\tau} \right)^2 \tag{B.31}$$

As described above, we could obtain equation (B.15) and equation (B. 22) to update π_k, equation (B.26) to update $\mu_{n,\tau}$, and equation (B.31) to update σ.